

Optical properties of thermally annealed CdZnSe/ZnSe quantum dots

Dissertation zur Erlangung des
naturwissenschaftlichen Doktorgrades
der Bayerischen Julius-Maximilians-Universität
Würzburg



vorgelegt von

Emanuela Margapoti

geboren in Lecce (Italy)

Würzburg 2010

Eingereicht am: 25 August 2009
bei der Fakultät für Physik und Astronomie

1. Gutachter der Dissertation: Prof. Dr. L. Worschech
2. Gutachter der Dissertation: Prof. Dr. K. Brunner

1. Prüfer der mündlichen Prüfung: Prof. Dr. L. Worschech
2. Prüfer der mündlichen Prüfung: Prof. Dr. Kinzel

Tag der mündlichen Prüfung: 20 Mai 2010

Doktorurkunde ausgehändigt am:

Parts of this work have been published:

- E. Margapoti, L. Worschech, Fabrizi M. Alves, S. Mahapatra, V. Lopez-Richard, K. Brunner, C. Destefani, C. Bougerol, Menéndez-Proupin, Fanyao Qu, G. E. Marques, A. Forchel
'Characterization of spin-state tuning in thermally annealed semiconductor quantum dots',
Phys. Rev.B **82**, 205318 (2010)
- E. Margapoti, L. Worschech, S. Mahapatra, K. Brunner, Fabrizio M. Alves, V. Lopez-Richard, G. E. Marques, C. Bougerol, and A. Forchel
'Negative magneto-polarization in thermally annealed self assembled quantum dots',
Phys. Rev.B **77**, 73308 (2008)
- E. Margapoti, L. Worschech, A. Tribu, T. Aichele, R. André, K. Kheng and A. Forchel
'Annealing induced inversion of quantum dot fine-structure splitting',
Appl. Phys. Lett. **90**, 181927 (2007)
- E. Margapoti, L. Worschech, S. Mahapatra, T. Slobodskyy, A. Tribu, T. Aichele, K. Brunner, G. Schmidt, L. W. Molenkamp, R. André, K. Kheng, C. Bougerol and A. Forchel
'Optical characterization of thermally annealed self-assembled ZnCdSe quantum dots',
Phys. Stat. Sol. (c) **4**, 3280-3288 (2007)
- S. Mahapatra, T. Kiessling, E. Margapoti, G. V. Astakhov, J. Renner, U. Bass, C. Bougerol, T. Schmidt, A. Bendounan, F. Schmitt, C. Schumacher, L. Worschech, W. Ossau, J. Geurts, L. W. Molenkamp, F. Reinert, A. Forchel, and K. Brunner
'CdSe/ZnSe heteroepitaxy: Aspects of growth and self organization of nanostructures',
Phys. Stat. Sol. (c) **4**, 3129-3149 (2007)
- S. Mahapatra, T. Kiessling, E. Margapoti, G. V. Astakhov, W. Ossau, L. Worschech, A. Forchel, K. Brunner
'Layer-by-layer growth and island formation in CdSe/ZnSe heteroepitaxy',
J. Crystal Growth **301-302**, 310 (2007)
- S. Mahapatra, E. Margapoti, L. Worschech, A. Forchel, K. Brunner
'Amorphous-Te mediated self organization of CdSe/ZnSe nanostructures',
J. Crystal Growth **301-302**, 293 (2007)

- S. Mahapatra, K. Brunner, C. Schumacher, T. Kiessling, G. V. Astakhov, U. Bass, E. Margapoti, W. Ossau, J. Geurts, L. Worschech, A. Forchel, and L. W. Molenkamp,
'Comparative study of self-assembled CdSe/ZnSe quantum dots grown by variants of conventional MBE
Phys. Stat. Sol. (c) **3**, 928 (2006)
- E. Margapoti, L. Worschech, T. Slobodskyy, L. W. Molenkamp, and A. Forchel
'Enhanced Zn-Cd interdiffusion and biexciton formation in self-assembled CdZnSe quantum dots in thermally annealed small mesas',
J. Appl. Phys. **100**, 113111 (2006)
- S. Mahapatra, T. Kiessling, E. Margapoti, G. V. Astakhov, W. Ossau, L. Worschech, A. Forchel, and K. Brunner
'Formation mechanism and properties of CdSe quantum dots on ZnSe by low temperature epitaxy and in situ annealing'
Appl. Phys. Lett. **89**, 043102 (2006)
- E. Margapoti, L. Worschech, S. Mahapatra, K. Brunner, C. Bougerol, and A. Forchel
'Tuning the magnetic properties of ZnCdSe/ZnSe quantum dots by thermal annealing',
Phys. Stat. Sol. (c) **3**, 3904 (2006)
- E. Margapoti, L. Worschech, T. Slobodskyy, L. W. Molenkamp, and A. Forchel
'Thermal annealing of self-assembled CdZnSe quantum dots studied by photoluminescence spectroscopy',
Phys. Stat. Sol. (c) **3**, 920 (2006)

Contents

Summary	1
1 Introduction	8
2 Basic optical properties of CdZnSe quantum dots (QDs)	11
2.1 Self-assembled quantum dots	12
2.1.1 Energy levels of a QD	12
2.1.2 Optical excitation	13
2.1.3 Exciton in QDs	15
2.1.4 Trions and biexcitons in QDs	15
2.1.5 Exciton in anisotropic quantum dots: Fine structure splitting	17
2.1.6 Quantum dot exciton in magnetic fields: Fock-Darwin formalism	20
2.2 The KP theory: valence band calculation	23
2.3 Diffusion properties	24
2.3.1 Fick's laws	24
3 Experimental basics	27
3.1 Experimental methods	27
3.1.1 Micro-PL for the detection of SQD	27
3.1.2 Detection of linear polarized components	28
3.1.3 Photoluminescence of QDs in an external magnetic field	29
3.1.4 Detection of circular polarized components	30
3.2 Time resolved measurements	30
3.3 Sample fabrication	32
3.3.1 Single quantum dot detection	32
3.3.2 Mesas fabrication	33
3.4 Rapid thermal annealing	34
4 Method to calculate the activation energy	36
4.1 Eigen energy of annealed quantum dot	36
4.1.1 Evaluation of the characteristic curves	38

5	Optical characterization of CdZnSe QDs	40
5.1	Structuring of the sample	40
5.1.1	QDs-formation	40
5.1.2	Single QD photoluminescence	41
5.2	Annealing of CdZnSe QDs	42
5.3	Enhanced diffusion of single CdZnSe QDs	46
5.3.1	Model	48
6	Study of the anisotropy of a quantum dot	51
6.1	Control of QD-isotropy by thermal annealing	51
6.1.1	Tuning of the QDs symmetry	51
6.1.2	Strain assisted diffusion	54
7	Magneto-polarization in thermally annealed self assembled QDs	55
7.1	Introduction	55
7.2	Inversion of polarization	55
8	Paramagnetic response of TA nonmagnetic SQD	63
8.1	Paramagnetic response of TA nonmagnetic SQD	63
8.2	Sample preparation and experimental set-up	63
8.3	Experimental observation	64
8.4	Theoretical calculation	66
	Appendix A: KP theory	73
	Appendix B: Sample S1	79
	Sample S2	82
	Appendix C: Sample S2	82
	Appendix D: Sample S3	84
	Bibliography	87

Summary

Nowadays, low dimensional semiconductor heterostructures, like quantum wells (QWs), quantum wires, and quantum dots (QDs), form the basis of a number of unique applications in both micro- and opto-electronic industries. Most devices based on low-dimensional heterostructures make use of the fact that several properties of charge carriers in such systems are modified mainly due to quantum confinement. This has not only improved the performance of some of the existing devices, such as QD- based lasers and detectors, but has also paved the way for conceptually new "quantum devices".

Realization of low-dimensional quantum devices has been made possible by modern techniques of heteroepitaxial growth, such as molecular beam epitaxy (MBE). In heteroepitaxy, single-crystalline epi-layers of one semiconductor are grown atop substrates of another semiconductor crystal. Due to difference in the lattice parameters of the substrate and the grown epi-layer, heterostructures are almost always elastically strained. Though detrimental for QW-based devices, accumulation and release of elastic strain is the driving force behind the self-assembly of QDs in semiconductor heteroepitaxy. Furthermore, engineering of strain enables manipulation and control of fundamental electronic and optical properties of semiconductor heterostructures, such as their band gap, density of states, band splitting, and masses of charge carriers. A simple and elegant method to manipulate strain in heterostructures is by post-growth (epitaxy) thermal annealing. For self-assembled QDs in particular, thermal annealing induces an inter-diffusion between the QDs and the surrounding barrier layer, in which they are embedded. This leads to a change in size, shape, and composition of the QDs, concomitantly affecting the elastic strain. This thesis systematically investigates the effect of post-growth thermal annealing on the diffusion characteristics and magnetic/optical properties of epitaxially self-assembled CdSe/ZnSe QDs. CdSe/ZnSe represents the prototypical II-VI heterosystem, studied widely in the past for possible applications in blue-green lasers and light emitting diodes and very recently, to realize visible single photon sources.

To analyse the diffusion characteristics, photoluminescence (PL) spectroscopy has been carried out in extensive detail on single, as well as, ensembles of thermally annealed (TA) CdSe/ZnSe QDs. Since TA-induced interdiffusion modifies the effective size and composition of the QDs, the band gap and the confining potential profile of

the QDs are altered. Zn intermixing of CdSe QDs causes the effective band gap of the QDs to widen, which is... results in a blue-shift of the PL spectrum. For a series of QD-ensembles, each annealed for $t_A = 30$ s at temperatures from $T_A = 300$ - 550 °C, the change in the QD-composition has been calculated from the blue-shift of the exciton ground-state PL-emission, using a concentration function based on Fick's laws of diffusion. The diffusion length (L_D) and the activation energy (E_A) have been determined thereof. For the studied QDs, E_A has been evaluated to be 2.2 eV.

Additionally, TA results also in an enhancement of the PL-intensity and reduction of the full-width-at-half maximum (FWHM) of the spectra. This point towards an increased homogeneity of the QD-size and composition, and decrease in the concentration of defects around the QDs.

For single CdSe/ZnSe QDs, TA has been varied from 100-240 °C, in steps of 20 °C, with t_A kept fixed at 30 s. To access the ground state exciton emission of single QDs, mesas have been fabricated by electron beam lithography and dry-chemical etching and the luminescence has been recorded in a micro-PL set up. For single QDs, E_A depends strongly on the size of the mesas. While, for large mesas, the calculated values of E_A are comparable to that of the QD-ensembles, for small mesas, the activation energy is significantly smaller. For two mesas, 180 nm and 90 nm in diameter, E_A has been calculated to be 1.8 and 0.9 eV, respectively. This scaling of E_A with the mesa-size is due to an enhancement of Cd/Zn interdiffusion, mediated by the defects located on the sidewalls of the mesas.

On small mesas, the evolution of the PL spectra of individual QDs with TA further reveals that not only the size and composition of the QDs, their symmetry might also be tuned by TA. Typically, as-grown QDs are asymmetric in their in-plane dimensions, resulting in a breaking of their cylindrical symmetry. This causes the two-fold degeneracy of the excitonic ground state to be lifted and the PL-emission to be linearly polarized in two perpendicular directions. For generation of entangled single-photons using self-assembled QDs, as envisaged in quantum cryptographic applications, this energy-splitting of the excitonic ground state is highly unwelcome. Tremendous research efforts have therefore been directed to achieve symmetrical QDs, which would enable generation of indistinguishable photons on demand. It has been observed in this work that post-growth TA of QDs on small mesas allows the shape-asymmetry, and therefore the energy-splitting of the excitonic ground state, to be tuned to zero or even negative values.

On 80 nm mesas, thermal annealing at $T_A = 60$ °C and above has been observed to progressively reduce the energy splitting of the two linearly polarized non-degenerate ground exciton state emissions. At ~ 120 °C the fine splitting reduces to zero, signifying a complete suppression of the shape asymmetry. Beyond 120 °C, the fine-structure-splitting changes sign. For $T_A = 180$ °C the inverted fine-splitting has been observed to be twice as large as that of the as-grown QDs. Thus, it is demonstrated that simple post-growth thermal annealing can serve to eliminate the fine structure splitting of the

excitonic ground state in epitaxial QDs, essentially of any heterosystem.

Finally, the evolution of the magneto-optic response with post-growth thermal annealing has been studied for both individual QDs and QD-ensembles. An external magnetic field, applied perpendicular to the plane of the QDs (Faraday configuration), results in Zeeman spin splitting of the ground exciton state. The emissions from the Zeeman-split states are left and right circularly polarized and from the degree of circular polarization (DCP), as well as, the spectral separation of the PL-peaks, the g-factor can be estimated. For CdSe/ZnSe QD-ensembles, the g-factor has been observed to change sign with TA. This is explained by the TA-induced change in the occupation of the light- and heavy-hole states, via a change in the size and Zn/Cd concentration of the quantum dots. For single QDs, the g-factor has been calculated to be $g_X = 1.1$ and $g_X = 3$, prior to and after TA, respectively. These results highlight the fact that post growth thermal annealing strongly influences the magneto-optic response of the investigated QDs.

It is well known that apart from the Zeeman-splitting, both spin-states show a diamagnetic blue-shift, with quadratic dependence on the applied magnetic field. In this work, similar to previous reports, diamagnetic shift has been recorded for as-grown (single) CdSe/ZnSe QDs. However, thermal annealing has been observed to cause a pronounced red-shift of the spectra, strongly suggesting a paramagnetic behavior. Paramagnetism requires the presence of unpaired spins, as in transition metal elements. Thus, diluted magnetic semiconductor (DMS) QDs, such as CdMnSe/ZnSe, are known to show a paramagnetic red-shift of the PL-spectra. The intrinsic paramagnetic dispersion, demonstrated in this work for thermally annealed single CdSe/ZnSe QDs is attributed to quantum-confinement-induced inversion of heavy- and light-hole states. This phenomenon, non-existent in bulk systems, might be observed in quantum dots based on any material system. Therefore annealed semiconductor QDs have the potential to serve as a new class of magnetic material due to an intrinsic magnetization. In conclusion, this thesis presents a comprehensive study of the evolution of a number of important attributes of CdSe/ZnSe QDs with post-growth thermal annealing, several findings of which are applicable, in general, to epitaxial QDs of most semiconductor heterosystems.

Zusammenfassung

Heutzutage bilden niederdimensionale Halbleiterheterostrukturen die Grundlage für zahlreiche spezielle Anwendungen sowohl in der mikro- wie auch der optoelektronischen Industrie. Viele dieser Bauteile beruhen dabei auf der Tatsache, dass die grundlegenden Eigenschaften von Ladungsträgern in diesen Systemen durch quantenmechanischen Einschluss modifiziert werden. Dies führte nicht nur zu einer deutlichen Leistungssteigerung der aktuellen Bauteile, sondern ebnete den Weg für konzeptionell neuartige "Quantenbauelemente".

Die Realisierung niederdimensionaler "Quantenbauelemente" ermöglichen moderne Techniken des heteroepitaktischen Wachstums wie beispielsweise die Molekularstrahl-epitaxie (MBE). In der Heteroepitaxie werden monokristalline Schichten eines Halbleiters auf die Oberfläche eines anderen Halbleiterkristalls aufgebracht. Die unterschiedlichen Gitterkonstanten des Substrates und der gewachsenen Halbleiterschicht führen sehr häufig zu elastischen Verspannungen dieser Heterostrukturen. Auf- und Abbau von Gitterverspannungen, die sich nachteilig auf Quantenfilm basierende Bauteile auswirken, können zur Formation selbstorganisierter Quantenpunkte in Halbleiterheterostrukturen genutzt werden. Weiter können diese Gitterverspannungen dazu genutzt werden, die fundamentalen elektronischen und optischen Eigenschaften von Halbleiterheterostrukturen gezielt einzustellen. Zu nennen sind hier neben der Bandlücke, die Zustandsdichte, die Feinstrukturaufspaltung der Energiebänder sowie die effektive Masse der Ladungsträger. Eine einfache Möglichkeit die Gitterverspannungen in Heterostrukturen zu manipulieren, ist das thermische Ausheilen, oft auch "thermal annealing" genannt. Besonders im Fall selbstorganisierter Quantenpunkte führt thermisches Ausheilen zu einer Interdiffusion zwischen dem Material der Quantenpunkte und der sie umgebenden Barriere. Dies führt zu Veränderungen in Größe, Form und Materialzusammensetzung der Quantenpunkte, die maßgeblich vom Grad der Gitterverspannungen beeinflusst werden. Die vorliegende Arbeit untersucht systematisch den Einfluss des "post-growth thermal annealing" auf die Diffusionscharakteristik sowie die magnetischen und optischen Eigenschaften von epitaktisch hergestellten selbstorganisierten CdSe/ZnSe Quantenpunkten. CdSe/ZnSe Quantenpunkte repräsentieren ein in der Vergangenheit intensiv untersuchtes prototypisches II-VI Heterosystem zum Einsatz in blau-grünen Lasern, Licht emittierenden Dioden und seit kurzem zur Realisierung von Einzelphotonenquellen im sichtbaren Spektralbereich. Die Dif-

fusionscharakteristik wurde mittels detaillierter Photolumineszenz-(PL)-Spektroskopie an einzelnen sowie an Ensembles von thermisch ausgeheilten (TA) CdSe/ZnSe Quantenpunkten untersucht. Da TA induzierte Interdiffusion die effektive Größe und Zusammensetzung der Quantenpunkte beeinflusst, ändern sich auch die Bandlücke und das Einschusspotential dieser Strukturen. Die Durchmischung der CdSe Quantenpunkte mit Zn führt zu einer Erhöhung der Bandlücke und resultiert folglich in einer Blauverschiebung des PL- Spektrums. Für eine Serie von Quantenpunktensembles, die jeweils für $t_A = 30$ s bei Temperaturen von $T_A = 300-500$ °C ausgeheilt wurden, kann die Veränderung in der Quantenpunktzusammensetzung mittels der Blauverschiebung des Exziton-Grundzustandes berechnet werden. Dazu wird eine Konzentrationsfunktion basierend auf dem Fick'schen Gesetz angenommen und die Diffusionslänge (L_D) sowie die Aktivierungsenergie (E_A) können bestimmt werden. Für die untersuchten Quantenpunkte kann E_A zu 2.2 eV bestimmt werden.

Zusätzlich führt TA zu einer Zunahme der PL Intensität und zu einer Reduktion der Halbwertsbreite (FWHM) des Spektrums. Dies deutet auf eine zunehmende Homogenität der Quantenpunkte und einer Abnahme der Kristalldefekte im Umfeld hin.

Für CdSe/ZnSe Quantenpunkte wurde das TA für Temperaturen zwischen 100-240 °C in Schritten von 20 °C bei konstanter Zeit $t_A = 30$ s durchgeführt. Für den Zugang zum Grundzustand einzelner Quantenpunkte wurden Mesen mit Hilfe von Elektronenstrahlolithographie und Trockenätzverfahren hergestellt und das Lumineszenzsignal dieser Proben mit Mikro-PL untersucht. Für einzelne Quantenpunkte ist E_A stark von der Größe der Mesa abhängig. Während für große Mesen die berechneten Werte von E_A mit denen des Quantenpunktensembles vergleichbar sind, fällt die Aktivierungsenergie für kleine Mesen deutlich geringer aus. Für Mesen mit 180 nm und 90 nm konnte E_A zu 1.8 eV beziehungsweise 0.9 eV berechnet werden. Die Größenabhängigkeit von E_A wird dabei auf eine Zunahme der Cd/Zn Interdiffusion durch Gitterdefekte an den Seitenflächen der Mesen zurück geführt. Die Veränderungen des PL-Spektrums einzelner Quantenpunkte zeigt zudem, dass nicht nur die Materialzusammensetzung, sondern auch die Symmetrie der Quantenpunkte durch TA beeinflusst wird. Typischerweise besitzen epitaktisch gewachsenen Quantenpunkte senkrecht zur Wachstumsrichtung eine starke Asymmetrie. Dies führt zur Aufhebung der zweifach entarteteten, optisch aktiven Exziton-Grundzustände und die PL-Emission weist zwei senkrecht zueinander orientierte lineare Polarisationszustände auf. Für die Realisierung von verschränkten Einzelphotonenzuständen selbstorganisierter Quantenpunkten, wie sie für Anwendungen der Quantenkryptographie angestrebt werden, ist die Energieaufspaltung der Exzitonenzustände äußerst unwillkommen. Aus diesem Grund wurden vielseitige Anstrengungen unternommen, symmetrische Quantenpunkte zu realisieren, die es ermöglichen ununterscheidbare Photonenzustände zu generieren. Im Rahmen dieser Arbeit wurde beobachtet, dass TA einzelner Quantenpunkte es ermöglicht, die Form-asymmetrie und damit die Energieaufspaltung des Exziton-Grundzustandes auf Null oder negative Werte zu verändern. An 80 nm großen Messen konnte eine zunehmende Reduk-

tion der Energieaufspaltung der beiden linear polarisierten, nicht entarteten Exziton-Grundzustände für TA Temperaturen von $T_A = 60$ °C und darüber beobachtet werden. Für $T_A = 120$ °C verschwindet die Feinstrukturaufspaltung und damit die Formasymmetrie der Quantenpunkte. Oberhalb von 120 °C tritt ein Vorzeichenwechsel der Energieaufspaltung auf. Eine invertierte Energieaufspaltung, deren Betrag in etwa doppelt so groß ausfällt wie für epitaktisch gewachsenen Quantenpunkte, wurde für Temperaturen von ca. 180 °C beobachtet. Damit konnte gezeigt werden, dass mittels TA die Feinstrukturaufspaltung selbstorganisierter Quantenpunkte gezielt eliminiert werden kann. Abschließend wurde das magneto-optische Verhalten für thermisch ausgeheilte einzelne Quantenpunkte und Quantenpunktensembles untersucht. Ein externes Magnetfeld senkrecht zur Quantenpunkzebene (Faraday-Konfiguration) führt zu einer Zeeman-Aufspaltung des Exziton-Grundzustandes. Die Emission dieser aufgespaltenen Zustände sind links- und rechts-zirkular polarisiert. Über den Polarisationsgrad des PL-Signals kann der g-Faktor bestimmt werden. Für CdSe/ZnSe Quantenpunktensembles wurde ein Vorzeichenwechsel des g-Faktor durch TA beobachtet. Dieser kann mittels einer Änderung der Besetzung von Leicht- und Schwerlochzuständen durch Veränderungen in Größe und der Zn/Cd Konzentration der Quantenpunkte erklärt werden. Für einzelne Quantenpunkte wurde der g-Faktor vor und nach TA zu $g_x = 1.1$ und $g_x = 3$ bestimmt. Dies unterstreicht, dass thermisches Ausheilen maßgeblich die magneto-optischen Eigenschaften der untersuchten Quantenpunkte beeinflusst. Es ist bekannt, dass neben der Zeeman-Aufspaltung beide Spinzustände eine diamagnetische Blauverschiebung mit einer quadratischen Abhängigkeit vom externen Magnetfeld aufweisen. In dieser Arbeit wurde vergleichbar mit früheren Arbeiten die diamagnetische Verschiebung für epitaktisch hergestellte Quantenpunkte beobachtet. Dagegen zeigte sich, dass durch TA die Spektren der Quantenpunkte eine deutliche Rotverschiebung aufweisen, die auf ein paramagnetisches Verhalten schließen lassen. Para-magnetismus jedoch setzt die Anwesenheit von ungepaarten Spins voraus, wie sie beispielsweise in Übergangsmetallen auftreten. Aus diesem Grund zeigen semimagnetische (DMS) Quantenpunkte, wie beispielsweise CdMnSe/ZnSe eine paramagnetische Rotverschiebung des PL-Spektrums. Die in dieser Arbeit demonstrierte paramagnetische Verteilung für thermisch ausgeheilte Quantenpunkte wird auf eine durch quantenmechanischen Einschluss bedingte Inversion der Schwer- und Leichtlochzustände zurückgeführt. Dieses Phänomen, das nicht im Volumenhalbleiter existiert, kann prinzipiell in jedem Materialsystem beobachtet werden. Daher bergen thermisch behandelte Quantenpunkte das Potential einer neuen Klasse magnetischer Materialien. Zusammenfassend präsentiert die vorliegende Arbeit eine ausführliche Untersuchung des Verhaltens einiger wichtiger Eigenschaften von CdSe/ZnSe Quantenpunkten durch TA, die allgemein auf epitaktische Quantenpunkte vieler weiterer Halbleiterheterosysteme übertragen werden können.

Chapter 1

Introduction

A semiconductor nanostructure quantum dot (QD) confines the motion of an electron and a hole, or similarly of an exciton. Since the 3D charge confinement within QDs is comparable to that in real atoms, QDs are often referred to as artificial atoms. Additionally, like real atoms, filling of the energy states in QDs follows the Hund's rule [JAC98]. However, there are also several distinct differences between the two systems. The shape of the confinement potential of QDs, unlike real atoms, offers itself to be manipulated and controlled, which make them attractive candidates to probe quantum phenomena.

There are several ways to apply 3D confining potentials. One of them is by application of electrostatic potentials [LIS03] to a 2DEG, using external electrodes. Other ways include the use of semiconductor surfaces (nanocrystals) [TAL02] or interfaces between two semiconductors with different band-gap energies. An interface of this kind is easily achieved by modern crystal growth techniques, like molecular beam epitaxy (MBE) (self-assembly)[MER98]. QDs might also be formed by combination of lithography and chemical etching [ZAI01]. The QDs studied in this thesis were prepared by MBE.

In the context of epitaxially self-assembled QD formation, several heterosystems have been investigated in the past years. In the early 1990s, QDs were made using typically III-V (i.e. InAs/GaAs) and group IV (i.e. Ge/Si) semiconducting materials [MAR94, GRU95]. III-V QDs exhibited fluorescence in the infrared (IR) region. The wavelength of QD-emission can be easily tuned by simply tuning the size of QDs. Thus QDs are attractive candidates for applications in the field of telecommunication requiring emission at $\sim 1.3\text{-}1.5 \mu\text{m}$ [TAK05]. Recently, QDs of wide-bandgap II-VI semiconductors have attracted considerable research interest because of their emission in the visible range of the electromagnetic spectrum. The two most widely studied II-VI heterosystems are CdSe/ZnSe and CdTe/ZnTe. The lattice mismatch between CdSe and ZnSe is 7 %, i.e. a value very similar to that of the prototypical system InAs/GaAs.

Apart from their emission in the blue-green region of the electromagnetic spec-

trum, epitaxially self-assembled CdSe/ZnSe QDs have been found to possess several other features, interesting for studies of fundamental physical phenomena as well as realization of novel device concepts. The II-VI QDs are characterized by strong electron exchange (EHX) interaction [SAN03, TAK93] and also strong oscillator strengths for optical transitions. Further, it has been found that both parameters can be tuned to certain extent by changing the size, shape, and material composition of the QDs. The EHX causes the otherwise-degenerate ground state of the QD to split into two non-degenerated components. While the emission from the pure degenerate states are σ^+ and σ^- polarized, that of the mixed non-degenerate states are π^+ and π^- polarized. The EHX splitting of the ground QD-state results due to asymmetric shape of CdZnSe QDs. This topic has attracted considerable research interest. A non-degenerate QD-ground state precludes the use of QDs in applications like generation of entangled photons.

Another interesting aspect of II-VI QDs is in the fact that they, e.g. can be rendered magnetic by the intentional incorporation of paramagnetic ions, Mn^{2+} [AWS00, BAC02, AND50]. Ions of Mn^{2+} embedded in CdZnSe QDs lead to a strong Zeeman splitting of the confined states in magnetic fields. Recently an unique paramagnetic behaviour of the ground state of such QDs, in absence of Mn^{2+} incorporation has also been demonstrated by us [MARG1, MARG2].

As mentioned before, several attributes of CdZnSe QDs are strongly dependent on their shape, size, and composition. As-grown self-assembled QDs are characterized by a spread in their dimensions and composition. A simple and elegant way of tuning these properties of self-assembled QDs is by performing post-growth thermal annealing, which essentially induces interdiffusion between the QDs and the surrounding matrix. This thesis deals with post-growth thermal annealing (TA) of epitaxially self-assembled CdZnSe QDs (prepared by MBE) and how TA influences the composition and morphology of QDs, and in turn, the EHX and magnetic response of QD-optical transitions.

The work of this thesis is presented in eight chapters as follows:

- Chapter 2 is a general introduction to the physics of QDs. First, it discusses the types of excitons encountered in a QD. Then, QD symmetry and its influence on the exciton recombination (or optical transition) is presented. A general understanding of the magnetic properties of such QDs is discussed next, which covers dia-, para-, and ferro-magnetism in QDs, as well as, Zeeman splitting. To describe the electronic levels of the QDs, the $\vec{K} \cdot \vec{P}$ theory and the Luttinger model is introduced in this chapter, with particular emphasis to confined systems. To deal with the interdiffusion process, which is central to a thermal annealing experiment, Fick's laws of diffusion and Arrhenius' law are also explained. Calculations of the electron and hole states, corresponding to different annealing steps are shown in this chapter.

- In chapter 3, the method of sample fabrication and processing, in order to measure the single QD optics, is briefly discussed. Later, the set-ups used are depicted and discussed in all their elements. Finally, the method of performing thermal annealing is also described.
- Chapter 4 deals with the method used to calculate the electron and hole states for thermally annealed QDs. By using the Fick's second law the activation energy of diffusion was then calculated.
- Chapter 5 deals with the optical characterization of thermally annealed CdZnSe QDs. TA-induced Cd-Zn interdiffusion in single as well as large ensembles of CdZnSe QDs is demonstrated. For both cases the activation energies corresponding to the thermally activated interdiffusion process are determined.
- In Chapter 6, the influence of TA on the symmetry of single CdZnSe QD has been studied. The typical asymmetry of the as-grown QDs is strongly affected by the TA process, leading to the achievement of almost symmetric QDs and even reversal of QD asymmetry.
- Chapter 7 deals with the magnetic-optical properties of self-assembled semiconductor QDs. The magnetic-optical response of several thermally annealed QDs samples was investigated by polarization resolved measurements. Information on the spin splitting of the ground state of the electron and heavy-holes is shown to be strongly dependent on QD-parameters.
- Chapter 8 studies the influence of thermal annealing on the magneto-optic response of CdZnSe QDs. Here, it is shown that the QD ground state, corresponding to certain combinations of size and composition shows a paramagnetic behavior. A detailed theoretical model based on the Luttinger Hamiltonian attributes this behavior to a reversal of the ground state character from a heavy-hole-like to a predominantly light-hole like, achieved by TA.

Chapter 2

Basic optical properties of CdZnSe quantum dots

In this chapter the physics of quantum dots, pertinent to the understanding of the optical experiments performed on epitaxially self-assembled CdSe/ZnSe QDs, subject to sequential post-growth rapid thermal annealing, is discussed. Due to TA, the optical and magnetic properties of a QD are modified. Here, special attention is paid to the analysis of fine structure splitting (FSS) and the magneto-optical response of excitons, confined within self-assembled QDs.

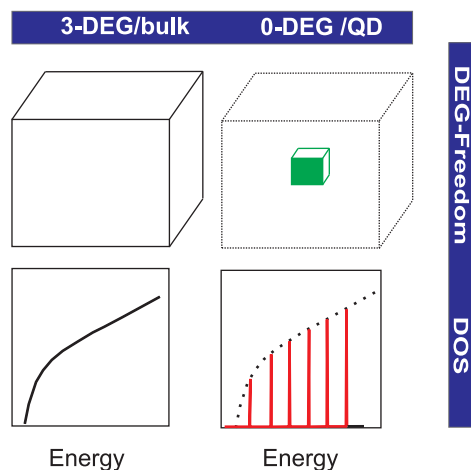


Fig. 2.1: Sketches of electronic densities of the states (DOS) of a bulk semiconductor crystal with a three-dimension (3D) electrons gas (3-DEG) (left) and for a QD with a 0D-DEG (0-DEG) (right).

2.1 Self-assembled quantum dots

A quantum dot is a small region of a semiconductor in which electrons, holes or both are trapped due to a spatial confinement in all three directions. This is in contrast to the continuous density of states (DOS) known for bulk semiconductor crystals.

Due to the quantum dot size, in the nanometer length-scale, the electronic states within a QD are quantized, owing to two main mechanisms. The first the "quantum confinement", where the bound level of the confined particles are determined by the standing-wave function of the Schrödinger equation (as shown in the next section). Since the energy of these states vary about as the inverse of the de Broglie wavelength, the distance between the quantized levels is proportional to $1/R^2$, where R is the radius of the quantum dot. Another important mechanism appearing in quantum dots is the electrostatic Coulomb interaction between the particles. The strength of this interaction vary as $1/R$. For large QD, where the confinement is poor, the main contribution to the quantization of the energy level is added by the electrostatic interaction between the particles

A typical picture which depict the situation of bulk semiconductor with a three dimensional-(3D)EG and quantum dot with zero dimensional-(0D)EG, is schematically shown Fig. 2.1. The charge carriers of a bulk semiconductor, which are free to move in all three directions, become trapped, which is thus lead to a discrete DOS of QDs.

Crystal growth technologies allowed the fabrication of heterostructure with confinement in one dimension (quantum well), in two dimension (quantum wires) and in three dimension (quantum dot). In this thesis QDs with a type-I confinement were studied. They are able to confine both electrons and holes.

2.1.1 Energy levels of a QD

There exist many different methods to describe numerically the energy levels of quantum dots [PRY98, STI99, WAN99], which show the impact of size, shape and composition on the electronic structures of QDs. In order to gain an understanding of the energy levels effective mass approximations [CHU95] can be applied.

Assume an electron in the conduction band of a semiconductor with a periodic lattice structure and ignore spin. For a plane wave with momentum \vec{k} , the wavefunction can be written as:

$$\psi_e(\vec{r}) = e^{i\vec{k}\cdot\vec{r}} u_{e,\vec{k}}(\vec{r}), \quad (2.1)$$

where $u_{e,\vec{k}}$ is periodic with the lattice. In the effective mass approximation the wavefunction of an electron that experiences a slowly varying potential can be written

as

$$\psi_e(\vec{r}) = f(\vec{r})u_{e,\vec{k}}(\vec{r}), \quad (2.2)$$

where $f(\vec{r})$ is an envelope function, which satisfy the Schrödinger equation:

$$\left[-\frac{\hbar^2}{2m^*} \nabla^2 + V(\vec{r}) \right] f(\vec{r}) = E f(\vec{r}). \quad (2.3)$$

Here m^* is the effective mass related to the curvature of the conduction band at $\vec{k} = 0$, $V(\vec{r})$ is the effective potential and E is the energy of the state. Due to the typical flat shape of self-assembled QDs along the growth axis (z direction), it is common use to describe the QDs by a harmonic potential in the x - and y -direction (in-plane) and an infinite square potential well in the z -direction. The following energy levels are:

$$E_n = (n_x + n_y + 1)\hbar\omega_0 + \left(\frac{\pi^2 \hbar^2}{2m^* L^2} \right) n_z^2, \quad (2.4)$$

where $\hbar\omega_0$ is the energy-level spacing, n_x and n_y are integers ≥ 0 , and n_z is an integer ≥ 1 . Usually the height of a quantum dot, L , is assumed to be small so that only $n_z = 1$ states are considered.

For the electrons in the conduction band, the atomic orbital functions contained in $u_{e,0}$ have s -like symmetry. Therefore there is only one conduction band which has spin degeneracy. For holes in the valence bands, the situation is more complicated since the atomic orbital functions have p -like symmetry. Neglecting the spin-orbit interaction, there are two bands, heavy-hole and light-hole, which can mix. It is usually assumed that the highest valence-band state has a heavy hole nature, when the quantization occurs in the z direction, i.e. the axis of symmetry.

It is usually assumed that the energy difference between the first heavy hole (hh) state and the first light hole (lh) state is large, so that the light holes states can be neglected. The magnetic component of the heavy-hole states can be written as $|m_j^{hh} = 3/2\rangle = |m_l = 1, \uparrow\rangle$ and $|m_j^{hh} = -3/2\rangle = |m_l = -1, \downarrow\rangle$, where m_l and m_j^{hh} are the z projections of the orbital angular momentum and the total angular momentum for the heavy-hole states, respectively. Nevertheless, such an approximation cannot always be used. It depends on the QDs shape, size and composition which can also result in a narrowing of the gap between the two heavy- and light- band states, which in turn mixes the states. In such a case the model mentioned above cannot be used and a band mixing theory has to be considered (see chap. 8).

2.1.2 Optical excitation

It is possible to optically excite efficiently CdSe quantum dots, with energies above the CdSe bandgap, and on resonance with transitions within the quantum dot (CdSe). In

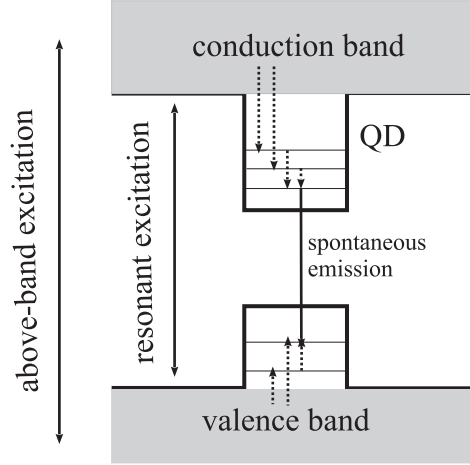


Fig. 2.2: Schematic illustration of the energy levels for above-band and resonant excitation.

above-band excitation (see Fig. 2.2), the laser wavelength is tuned above the CdSe bandgap, which is for bulk about 680 nm (1.82 eV) at low temperature (2-4 K). It is convenient to use either UV laser excitation or blue laser with wavelengths around 405 nm (3.06 eV). Electrons and holes are thus generated in the ZnSe barrier of the CdSe QDs. Then carriers relax via cascades and due to interactions, e.g. with phonons, into the electron and hole ground states. The Coulomb interaction between electron and holes results in an additional lowering of the system's energy by forming excitons. The recombination of excitons leads to characteristic QD exciton lines. For weak excitation, the dominant intraband relaxation mechanism inside the quantum dot is thought to be phonon assisted [HEI96, ADL96], although the relaxation rates typically seen are faster than expected theoretically [TOD99, BOG01, ZHA01]. When the carrier density is higher, Auger processes can also contribute.

In resonant excitation (see Fig. 2.2), the laser wavelength is tuned to a higher transition within the quantum dot. A much larger laser power is required than for above-band excitation, since the absorption cross-section of a single quantum dot is very small. This method is usually used when one wants to create a single electron-hole pair directly inside the QD for single-photon sources measurements. There are several advantages of such an excitation scheme.

In this thesis, the above-band excitation was used. Since a large volume of ZnSe acts as absorber, more carriers are excited and funnel into the quantum dots. For continuous-wave (cw) excitation, appropriate pump powers range between a few μW up to tens of μW . This also allows the observation of biexcitons. Another good reason to use the above-band excitation is that the laser wavelength (around 405 nm) is far detuned from the quantum-dot emission wavelength (around 486 nm), so the scattered laser light can be easily cut off using appropriate filters.

2.1.3 Exciton in QDs

As described in the previous section an electron can be excited by a laser from the valence band to the conduction band, leaving a hole (see Fig. 2.3). When such electrons and holes are trapped within QDs, they bind together due to the attractive Coulomb interaction, forming *excitons* (X). To describe the exciton energy levels within a QD, the Hamiltonian can be written as:

$$H_{exciton} = H_e + H_{hh} + H_{Coulomb} \quad (2.5)$$

where H_e and H_{hh} represent the Hamiltonians for the QD confined electron and the heavy hole, respectively. The term $H_{Coulomb}$ takes into account the electron-hole Coulomb interaction. This term is discussed in detail in section 2.1.4. The ground electron state within a QD, which has an s-like character, is doubly degenerate, and is represented by $|m_j^e = 1/2\rangle = |m_l^e = 0, m_s^e = 1/2\rangle$ and $|m_j^e = -1/2\rangle = |m_l^e = 0, m_s^e = -1/2\rangle$, where m_j^e , m_l^e and m_s^e are the z-projection of the total, orbital and spin angular momenta, respectively. On the other hand, the hole ground state is assumed to be heavy-hole-like. It is also doubly degenerate, denoted by $|m_j^h = 3/2\rangle = |m_l^h = 1, m_s^h = 1/2\rangle$ and $|m_j^h = -3/2\rangle = |m_l^h = -1, m_s^h = -1/2\rangle$, respectively. The light-hole states, also doubly degenerate, are higher-lying in energy and represented as $|m_j^h = 1/2\rangle = |m_l^h = 0, m_s^h = 1/2\rangle$ and $|m_j^h = -1/2\rangle = |m_l^h = 0, m_s^h = -1/2\rangle$, respectively. The z-projection of the total angular momentum of a photo-generated exciton is given by $|m_j^X\rangle = |m_j^e + m_j^h\rangle$, leading to the following exciton states $|1\rangle$, $|-1\rangle$, $|2\rangle$ and $|-2\rangle$. The exciton states $|\pm 1\rangle$ couple to an incident light field and are known as the bright states, while the exciton states $|\pm 2\rangle$ cannot couple with light referred to as the dark states. The dark states are optically inactive because the spins of the electron and the hole, constituting the exciton, do not match [NIR95]. Fig. 2.3 shows a sketch for an off-resonant excitation of a QD, where an electron and a hole are previously formed in the continuum of states of the barrier layer (path 1). Subsequently, both the electron and the hole thermalize and scatter in the lower energy state (path 2) in the QD. Finally, the electron and the hole recombine giving rise to photoluminescence (PL) emission (path 3). All the measurements presented in this work were performed in such off-resonant excitation.

2.1.4 Trions and biexcitons in QDs

In the discussion so far, only neutral excitons, consisting of a Coulomb-bound electron-hole pair, have been considered. However, in optical spectroscopy of QDs, other charged and multiexcitonic species are often detected. The energy required to add extra charges of the same sign to a QD increases due to the Coulomb repulsion [MED97, BAN99]. It must be noted, that it is possible to add a positive as well as a negative charge to a QD. In this way, a positive (X^+) or a negative (X^-) trion are formed. By increasing the power of photoexcitation, a pair of excitons can be formed. A Coulomb-bound pair

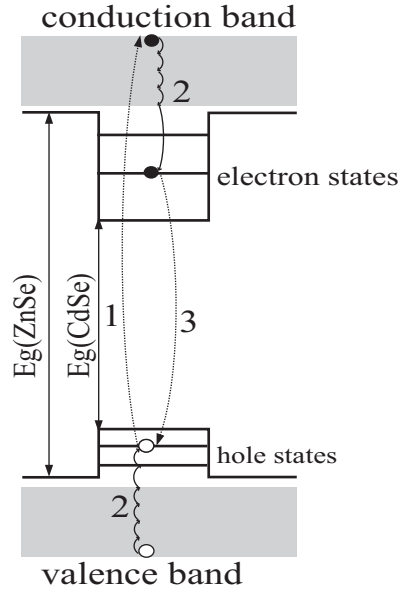


Fig. 2.3: Schematic representation of the photogeneration of electrons and holes into the continuum of states and their subsequent relaxation to the electron and hole ground states within the QD, under non-resonant excitation.

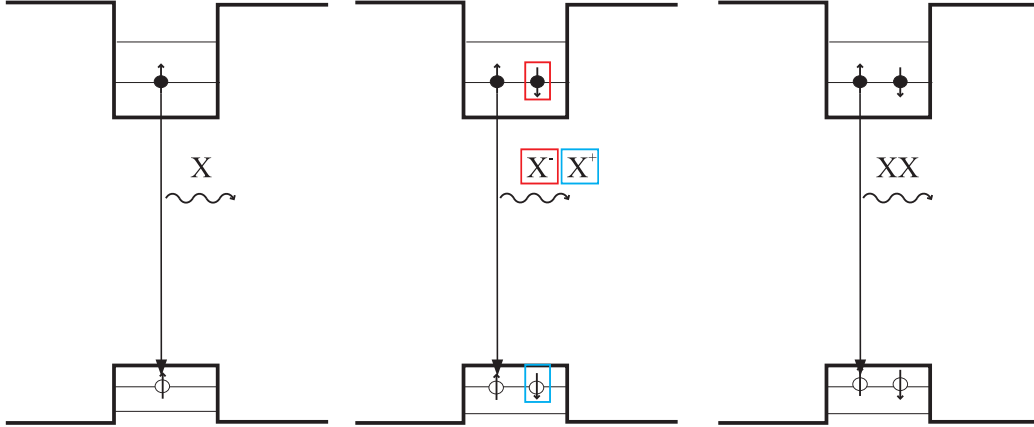


Fig. 2.4: Exciton, negative (red) and positive (blue) trion, and biexciton recombination.

of excitons is known as biexciton (XX). Normally, the biexciton appears several meV below the energy of the X ground state. A single particle sketch is shown in Fig. 2.4, where only information about the involved levels are given. The energy required to build a biexciton state is known as biexciton binding energy (BBE) and is expressed as

$$BBE = E(X \rightarrow 0) - E(XX \rightarrow X) \quad (2.6)$$

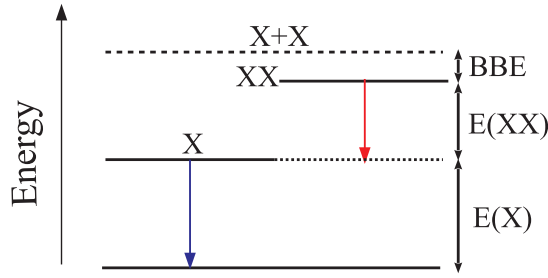


Fig. 2.5: Sketch of energy diagram of the biexciton binding energy defined as the energy difference between exciton $E(X \rightarrow 0)$ and of the biexciton $E(XX \rightarrow X)$ ground states

where $E(X \rightarrow 0)$ is the energy corresponding to ground state exciton transition and $E(XX \rightarrow X)$ is the transition from the biexciton to the exciton state [BAY98], as schematically shown in Fig. 2.5.

2.1.5 Exciton in anisotropic quantum dots: Fine structure splitting

In section 2.1.2, it was shown that the z-projection of the total angular momentum of an exciton, m_j^X , is the sum of the corresponding momenta of the constituent electron and hole, which is a good quantum number for QDs possessing rotational symmetry along the z-axis. Only in that case the bright exciton state is two-fold degenerate. However, epitaxially self-assembled QDs more often possess an asymmetric shape, due to which the degeneracy of the bright exciton state is lifted. This is caused by the exchange integral originating from the Coulomb interaction. The energy splitting between the mixed sub-states formed due to the exchange interaction, can be directly observed in PL spectroscopy of single QDs. Additionally, the transitions from the two sub-states are linearly polarized.

According to Kramer's theorem [MES99, TAK00], a system containing an odd number of spins (e.g. trions) has at least a two-fold degeneracy. In contrary, if the system contains an even number of spins (e.g. a biexciton) it can lose its degeneracy. The main contribution to the exciton-ground-state-splitting comes from the last term of eq. 2.5, $H_{Coulomb}$. $H_{Coulomb}$ can be distinguished in two parts, the "direct" and the "exchange" parts. The direct part of the Coulomb interaction is

$$H_{Coulomb}^{Direct} = \delta_{m_j^e, m_j^{e'}} \delta_{m_j^h, m_j^{h'}} \int d^3 r_e \int d^3 r_h |\psi_e(\vec{r}_e)|^2 \frac{-e^2}{\epsilon |\vec{r}_e - \vec{r}_h|} |\psi_h(\vec{r}_h)|^2 \quad (2.7)$$

where ϵ is the dielectric constant, r_h and r_e are the hole and electron radius, respectively, whereas ψ_h and ψ_e are the respective wavefunctions. This term mainly contributes to

the exciton binding energy. The term that is responsible of the splitting observed in asymmetric QDs is given by the exchange part, expressed by

$$H_{Coulomb}^{Exchange} = \delta_{m_j^e, m_j^h} \delta_{m_j^{e'}, m_j^h} \int d^3 r_e \int d^3 r_h \psi_e^*(\vec{r}_e) \psi_h(\vec{r}_e) \frac{-e^2}{\epsilon |\vec{r}_e - \vec{r}_h|} \psi_h^*(\vec{r}_h) \psi_e(\vec{r}_h) \quad (2.8)$$

This term arises from the antisymmetry of the fermionic wave function under exchange of particles [SAN03]. This equation can be further decomposed in two parts, the short-range and the long-range exchange interaction. They correspond to the case of $\vec{r}_e = \vec{r}_h$ and $\vec{r}_e \neq \vec{r}_h$, respectively. The energy splitting between the bright and the dark states is caused by the short-range part [MAS02] and their separation is indicated by δ_0 . The long-range part is responsible for the splitting of the bright exciton states, indicated by δ_1 . The long-range interaction is proportional to the spatial overlap between the electron and hole wave function, which is sensitive to the shape of the QDs [TAK93]. The energy levels depend on the nature of the potential confining the electron-hole pair. For the quantum dots discussed here the confinement is stronger along the z-direction (grow-direction) and lower along the in-plane directions, i.e. the relation $L_x, L_y > L_z$ is satisfied (see Fig. 2.6 (a)).

The splitting of the bright exciton states under the influence of the exchange interaction has been investigated experimentally [BLA94, CHA96, KUL99] and theoretically [BLA94, TAK93] and has been defined as fine structure splitting (FSS) of excitons. A sketch of the states with and without the influence of the exchange interaction is depicted in Fig. 2.6. The left side of Fig. 2.6 (b) shows the biexciton and exciton recombination when the exchange interaction is absent. The middle and right side show the X and XX emissions when the short- and the long-range exchange are present.

In the first case, when the exchange interaction and confinement is neglected, the ground state of the heavy hole is fourfold degenerate and the recombination of the exciton and biexciton are expressed by a single emission line with a BBE given by the direct component of the Coulomb interaction. However, by considering a QD with a cylindrical symmetry, which means belonging to the symmetric group D_{2d} , the short-range exchange interaction has to be considered. In this way, the previously fourfold degenerate ground-state is split into two dark and two bright states. The dark levels are further split into two components by $\delta_2 \ll \delta_0$.

Finally, when the long-range exchange interaction is considered in addition to the short range one, i.e. when the QD symmetry is $< D_{2d}$, the degeneracy of the bright states is also lifted. This is one of the topics studied extensively in this thesis. The energy splitting is denoted by δ_1 in Fig. 2.5 (b). Optical transitions from these states are linearly polarized along (π^+) and perpendicular (π^-) to the QD long-axis, which lie along the $\langle 110 \rangle$ directions in case of most self-assembled QDs, including CdSe/ZnSe.

It should be noted, that the XX ground state is a spin-singlet state ($S=0$). Therefore, the recombination of the biexciton state into the exciton state leads to a PL

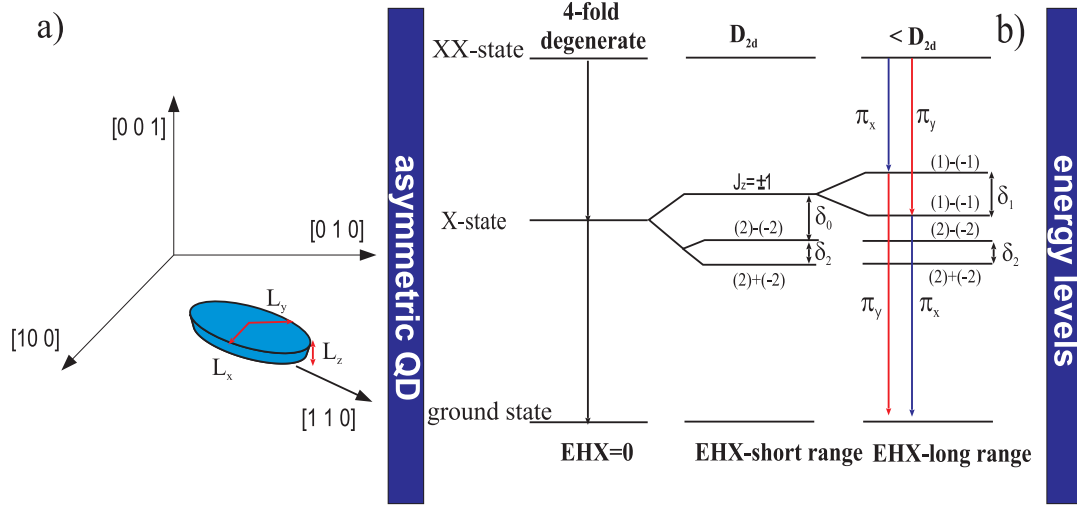


Fig. 2.6: (a) Sketch of an anisotropic QD (b) Schematic representation of the exciton and biexciton ground state in absence of electron-hole exchange interaction (left), in presence of the short (middle) and long range (right) exchange interaction.

emission, which mirrors the exciton recombination [KUL99] (See Fig. 2.5 (b)). This implies, that when the longitudinal and transverse polarization energy of an exciton is such that $\pi_x < \pi_y$, the biexciton shows an opposite behavior, i.e. $\pi_x > \pi_y$. In case of isotropic QDs, δ_1 vanishes and the bright exciton states $|+1\rangle$ and $|-1\rangle$ are degenerate. In case of a QD with an in-plane anisotropy, δ_1 is not zero and the Hamiltonian gives rise to more complex eigen functions, as follow: $|X\rangle = \frac{1}{\sqrt{2}}(|+1\rangle + |-1\rangle)$ and $|Y\rangle = \frac{1}{\sqrt{2}}(|+1\rangle - |-1\rangle)$, for the bright states. In table 2.1 the eigen functions and eigen values, for both anisotropic and isotropic QDs, and for both dark and bright states, are listed.

Tab. 2.1: Eigenfunctions and eigenenergies of both bright and dark exciton states for a symmetric (D_{2d}) and an asymmetric ($< D_{2d}$) QD.

D_{2d}	D_{2d}	$< D_{2d}$	$< D_{2d}$
eigen energy	eigenfunction	eigen energy	eigenfunction
$+\frac{1}{2}\delta_0$	$ -1\rangle$	$\frac{1}{2}\delta_0 + \frac{1}{2}\delta_1$	$\frac{1}{\sqrt{(2)}}(+1\rangle + -1\rangle)$
$+\frac{1}{2}\delta_0$	$ +1\rangle$	$\frac{1}{2}\delta_0 - \frac{1}{2}\delta_1$	$\frac{1}{\sqrt{(2)}}(+1\rangle - -1\rangle)$
$-\frac{1}{2}\delta_0 + \frac{1}{2}\delta_2$	$\frac{1}{\sqrt{2}}(+2\rangle + -2\rangle)$	$-\frac{1}{2}\delta_0 + \frac{1}{2}\delta_2$	$\frac{1}{\sqrt{(2)}}(+2\rangle + -2\rangle)$
$-\frac{1}{2}\delta_0 - \frac{1}{2}\delta_2$	$\frac{1}{\sqrt{2}}(+2\rangle - -2\rangle)$	$-\frac{1}{2}\delta_0 - \frac{1}{2}\delta_2$	$\frac{1}{\sqrt{(2)}}(+2\rangle - -2\rangle)$

2.1.6 Quantum dot exciton in magnetic fields: Fock-Darwin formalism

The spin properties of confined excitons in magnetic fields have been studied extensively over the last few years, both experimentally [TRA95, KOT01, BRA97] and theoretically [KOT01]. This has been triggered by the possibility of using confined spin systems in several device applications, including solid state qubits. Major interest has been in studying the Zeeman spin-splitting of the bright excitonic state and associated studies, i.e. tuning of the g-factor (magnitude and sign) by varying the size and composition of QDs (and also quantum wells). In addition the diamagnetic shift of the excitonic transition in magnetic fields has also gained considerable attention [TRA95]. In the following discussion, diamagnetic and paramagnetic properties of QDs are discussed because of their relevance to this thesis work.

Diamagnetism is a type of magnetism expressed as a weak repulsion from a magnetic field and exhibited only in presence of the field. Pure diamagnetic materials have all electrons paired, which implies the absence of a net magnetic moment.

When an external magnetic field B_{ex} is applied, the electron changes its velocity, generating an induced magnetic moment that opposes the magnetic field generating it. The change in velocity of the electron is followed by a change of the electron magnetic moment. The change in the orbital motion caused by B_{ex} is the effect that characterizes the diamagnetic materials. The material studied in this work are CdSe and ZnSe semiconductors, which have no unpaired electrons and are therefore with no net magnetic moment at zero field.

Let us consider the electron to be confined in a parabolic potential. The motion of an exciton confined in a parabolic potential, in a perpendicular magnetic field, can be expressed by the Hamiltonian:

$$H = \frac{1}{2m_e} \left(\vec{p} - \frac{e}{c} \vec{A} \right)^2 + \frac{1}{2} m_e \omega_0^2 r^2 \quad (2.9)$$

where m_e is the electron effective mass, \vec{A} the vector potential of a magnetic field \vec{B} and \vec{p} is the momentum. The first term describes the kinetic energy of a free electron and in an external magnetic field B. The two-dimensional parabolic well is described by the second term of eq. 2.9. This Hamiltonian, solved in the Fock-Darwin formalism [JAC98], gives the eigenvalues:

$$E_{(n,m)}(B) = \hbar\Omega(n+1) - \frac{1}{2}\hbar\omega_c m, \quad (2.10)$$

with $\Omega^2 = \omega_0^2 + \frac{1}{4}\omega_c^2$. While $n = 0, 1, 2, \dots$ and $m = -n, -n+2, \dots, n-2, n$ are the principal and the azimuthal quantum numbers, respectively. ω_0 and ω_c describe the frequency of the electron in absence and presence of a magnetic field B, respectively. The frequency ω_c is the cyclotron frequency described as $\omega_c = eB/m_e c$.

It is possible to distinguish between two cases, the motion of the electron in a strong magnetic field ($\omega_c \gg \omega_0$) or the case of the motion in a weak magnetic field ($\omega_c \ll \omega_0$). In the weak field regime, the electron is influenced by the QD confinement potential, while in strong magnetic fields the confined potential can be neglected. Therefore, it is possible to write the expression of the eigenvalue for the two regimes, separately as:

$$\omega_c \ll \omega_0 : E_{0,0}(B) = \hbar\omega_0 + \frac{1}{8} \frac{\omega_c^2}{\omega_0} = \hbar\omega_0 + \frac{1}{8} \frac{e^2}{m_e c \omega_0} B^2 \quad (2.11)$$

$$\omega_c \gg \omega_0 : E_{0,0}(B) = \hbar\omega_c + \frac{e}{2m_e c} B. \quad (2.12)$$

The quadratic term in B (in Eq.2.11) describe the diamagnetic shift, observed in weak-field regime. Eq. 2.12 gives the ground state energy in strong-field regime. In the present work all discussions are limited to the weak-field regime. In the above discussion the motion of an electron in a parabolic potential in presence of an external magnetic field is considered. However, for self-assembled QDs, the Hamiltonian has to be extended to an excitonic problem. Consequently, eq. 2.10 is rewritten taking into account also the holes:

$$\begin{aligned} H &= \frac{1}{2m_e} \left(\vec{p}_e - \frac{e}{c} \vec{A}_e \right)^2 + \frac{1}{2} m_e \omega_{0,e}^2 r_e^2 + \\ &+ \frac{1}{2m_h} \left(\vec{p}_h - \frac{e}{c} \vec{A}_h \right)^2 + \frac{1}{2} m_h \omega_{0,h}^2 r_h^2 - \frac{e^2}{\varepsilon |r_e - r_h|} \\ &= T_e + V_e + T_h + V_h + V_{eh}, \end{aligned} \quad (2.13)$$

where T_e and T_h are the electron and hole kinetic energies, V_e and V_h are the electron and hole potentials, while the last term V_{eh} describes the electron-hole Coulomb attraction. Therefore, the eigenvalue in case of an exciton can be written as:

$$E_{m_j}(B) = E_0 + \gamma B^2 - \frac{1}{2} m_j^X g_X \mu_B B \quad (2.14)$$

where the first term $E_0 = \hbar\omega_0$ is the eigen energy in absence of a magnetic field B, the second term is calculated within the first order perturbation theory and describes the *diamagnetic shift*. While, the last term is the Zeeman energy splitting, with g_X the exciton g-factor obtained from the electron and hole g-factors. m_j^X is the \hat{z} component of the total angular momentum of the exciton, defined as: $m_j^X = m_j^e \pm m_j^h = \pm 1$. The coefficient γ is called diamagnetic coefficient and can be expressed as:

$$\gamma = \frac{e^2}{8m^*} \langle r_x^2 \rangle, \quad (2.15)$$

where m^* is the exciton effective mass and $\langle r_x^2 \rangle$ the squared in-plane radius. Here one should note that γ is always positive and that it changes its amplitude with the effective mass and size of the dot.

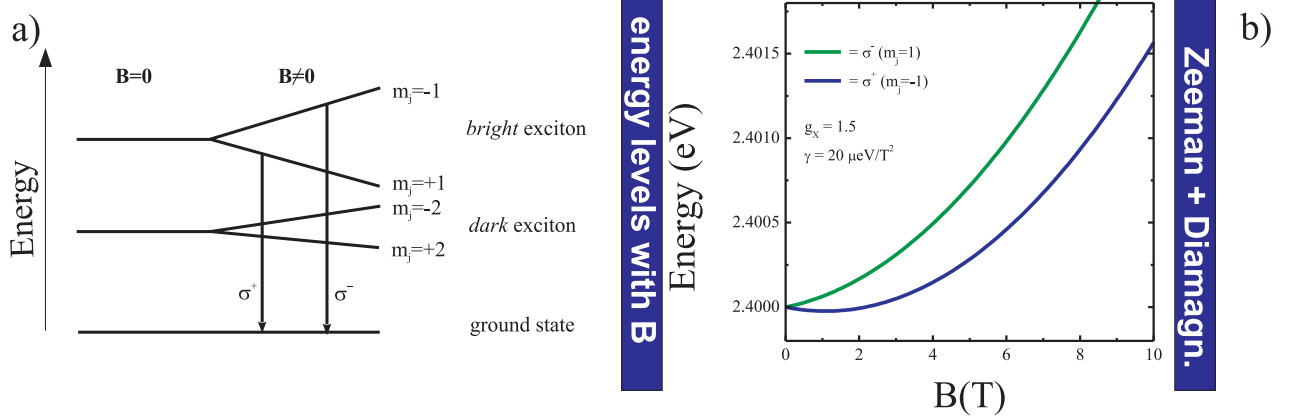


Fig. 2.7: (a) Zeeman splitting of the dark and bright exciton states. The circularly polarized emission from the two energy-split bright states are also shown. (b) Magnetic dispersion of the left and right circularly polarized emission from Zeeman spin-split bright exciton states, based on Eqn. 2.14

Eq.2.14 gives the energy splitting of the two circularly polarized components of the QDs-luminescence versus the magnetic field strength and, at the same time, the absolute energy shift of the two components. Since γ depends on the QD in-plane radius r_x and on the exciton effective mass m^* , it is found that, when e.g. the QD is small m^* is larger, leading to a decrease of the diamagnetic factor γ . In Fig. 2.7 (a) an example of the energy shift, calculated from eq. 2.14 is shown, depicting clearly a diamagnetic shift of components $m_j = \pm 1$. In this plot the g-factor has been assumed to be 1.5 and the diamagnetic coefficient to be $20 \mu\text{eV}/\text{T}^2$ [GOD06]. In Fig.2.7 (b) a sketch of the exciton ground state in absence and in presence of a magnetic field B is shown, neglecting the EHX interaction and the diamagnetic shift. The emissions are oppositely circularly polarized (σ^\pm).

Atoms constituting a **paramagnetic** material have permanent magnetic moments(dipoles), which in absence of a magnetic field are randomly oriented. Thus in absence of a magnetic field paramagnetic materials exhibit no magnetism. When a magnetic field is applied the dipoles are oriented all in the direction of the applied field, resulting in a net magnetic moment. If sufficient energy is exchanged between neighboring dipoles they interact and spontaneously align or anti-align to form magnetic domains, resulting in **ferromagnetism** (permanent magnets) or **antiferromagnetism**, respectively.

When paramagnetic ions like Mn^{2+} are incorporated into the lattice of a non-

magnetic semiconductor, for example ZnSe, the latter is rendered magnetic. Emission from CdSe QDs embedded in such a magnetic host (ZnMnSe), shows a strong magnetic dispersion [OH03, BAC01].

2.2 The KP theory: valence band calculation

In calculating the electronic energy levels of QDs, often the effective mass approximation is used and the bands are assumed to be parabolic around $\vec{k} = 0$. Albeit, this approximation is valid for the conduction band, for the valence band it turns out to be insufficient. The valence bands are more complicated than the conduction band for several reasons. One reason is that the symmetry of the orbitals are p-like and not s-like as for the conduction band and second difficulty arises from the spin-orbit coupling. Indeed, when the spin-orbit coupling is significant a splitting in the valence band with an energy Δ proportional to Z^4 arises, where Z is the atomic number. For some materials this value is very small and can be neglected.

The most well known method to describe the band structure is the $\vec{k} \cdot \vec{p}$ (KP) method. The idea is to rewrite the Schrödinger equation for the periodic part $u_{n\vec{k}}(\vec{R})$ of the Bloch functions alone, factoring out the plane wave. The new Hamiltonian in the frame of KP theory is rewritten as:

$$\hat{H}_{\vec{k}\cdot\vec{p}}(\vec{k}) = \left(\frac{\vec{p}^2}{2m_0} + V(\vec{R}) \right) + \left(\frac{\hbar}{m_0} \vec{k} \cdot \vec{p} + \frac{\hbar^2 k^2}{2m_0} \right). \quad (2.16)$$

The Hamiltonian $H_{\vec{k}\cdot\vec{p}}$ can be resolved using different approaches. One approach is to use perturbation methods (appendix A), which gives good results in proximity of $\vec{k} = 0$, but is insufficient for high \vec{k} -values. Another approach is to resolve $H_{\vec{k}\cdot\vec{p}}$ by the use of the *Kane Model* (Appendix A). The Kane model is a standard approximation that uses various level of complexity. In appendix A some information about the Kane model in case of a quantum well is given. However, this model does not describe well the light and heavy hole states for large values of \vec{k} , so then in order to simplify the model, a better approach is the *Luttinger model* (appendix A). This model not only gives a good understanding of the light and heavy hole states for $k \neq 0$, but also helps in the understanding of the light-heavy hole mixing effect. It has been already demonstrated that the biaxial tensile strain, which has an opposite effect on the confinement, was shown by [PER00] that the light and heavy hole gap decreases and rises the heavy hole subband above the light hole, while the opposite is normally observed when the confinement is present. When such a situation occurs, a valence band mixing (VBM) study needs to be considered.

2.3 Diffusion properties

In this section an overview of the basic diffusion laws is provided, as they are important for the interpretation of thermally annealed QDs. The diffusion process is caused by the thermal motion of individual atoms, molecules or nano-sized material particles. In order to get information about the activation energy (E_A) and diffusion length (L_D) of the thermal process, executed on single QDs, an introduction to the first and second Fick's law is given.

2.3.1 Fick's laws

The diffusion's law is a relationship between the diffusion-rate and the concentration gradient responsible of the net mass transfer:

$$\vec{J} = -D\vec{\nabla}C, \quad (2.17)$$

where $\vec{J}(x,y,z)$ is the flux flowing normally to the plane of diffusion, D is the diffusion coefficient and C the concentration. This expression is known as *Fick's first law* [GLI00]. In order to derive *Fick's second law* the conservation of the mass needs to be applied.

Mass conservation: If we consider a general point $P(x,y,z)$ in a cube of volume $\Delta x\Delta y\Delta z$, the flux $J(P)$ about the point P is the sum of the flux entering or leaving the opposite faces of the cube. Thus the mass balance is expressed as:

$$\text{inflow-outflow} = \text{accumulation rate}$$

applying this definition, the mass balance becomes:

$$-\left(\frac{\partial J_x}{\partial x} + \frac{\partial J_y}{\partial y} + \frac{\partial J_z}{\partial z}\right) \Delta x\Delta y\Delta z = \frac{\partial C}{\partial t} \Delta x\Delta y\Delta z, \quad (2.18)$$

By the definition of the divergence it is possible to rewrite eq. 2.18 as:

$$-\vec{\nabla} \cdot \vec{J} = \frac{\partial C}{\partial t} \quad (2.19)$$

Two cases can be distinguished: (i) If there is a converging flow at a point P ($\vec{\nabla} \cdot \vec{J} < 0$) the concentration rises with time, (ii) whereas if there is a diverging flow ($\vec{\nabla} \cdot \vec{J} > 0$) the concentration falls. This equation is known as continuity equation.

By the use of the above continuity equation (eq. 2.19) Fick's second law can be written, inserting eq. 2.17 into eq. 2.19:

$$\nabla^2 C = \frac{1}{D} \frac{\partial C}{\partial t}, \quad (2.20)$$

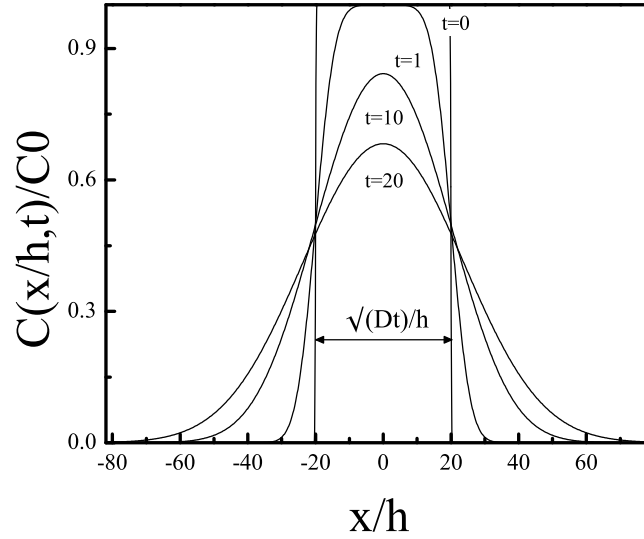


Fig. 2.8: Normalized concentration versus the normalized distance, for a slab-width of $2h$.

which is true only for constant values of D . Eq. 2.20 is known as *Fick's second law* or *linear diffusion equation*. Fick's second law is important because it allows to determine the concentration C , which in one dimension can be written as:

$$C(x, t_A) = C_0 \operatorname{erfc} \left(\frac{x}{2\sqrt{Dt_A}} \right), \quad (2.21)$$

where C_0 is the concentration at the time $t = 0$ for a slab of unidimensional material. The problem can be generalized to the case of two slabs, one with concentration $C_0 = 0$ (i.e. without material) and one with concentration $C_0 > 0$. It results in diffusion of the material from one slab with $C_0 > 0$ to the other slab with $C_0 = 0$. Generally, Fick's second law for can be written as:

$$C(x, t_A) = \frac{C_0}{2} \left[\operatorname{erf} \left(\frac{x/h + 1}{2h\sqrt{Dt_A}} \right) - \operatorname{erf} \left(\frac{x/h - 1}{2h\sqrt{Dt_A}} \right) \right], \quad (2.22)$$

where $2h$ is the thickness of the slab, D the diffusion coefficient and t the diffusion time. This expression, known as Grube-Jedele (G-J) diffusion [GLI00] is used in the calculation of the diffusion properties of QDs in Chapter 4 and Chapter 5. Indeed, eq. 2.22 is normally used to evaluate the diffusion length and the activation energy (E_A) in thermally activated processes for QDs or QW systems [CHE01, RAO94, BOL03]. The activation energy E_A , used firstly in 1889 by Svante Arrhenius, is the energy necessary

to activate a diffusion process and is defined via the diffusion coefficient:

$$D = D_0 e^{-E_A/kT_A} \quad (2.23)$$

where D_0 is the pre-factor and k the Boltzman constant. By the use of eq. 2.22, the concentration function $C(x,t)$ is found, as shown in Fig. 2.8 for a layer of size $h = 2$ and an initial concentration $C(x,0) = C_0$. Varying the annealing time ($t_A = 0, 1$ s 10 s, 20 s) the concentration profile smears out, thus leading to have different potential profiles, which characterize the system. By applying this model to thermally annealed QDs, varying either the annealing temperature (T_A) or the annealing time (t_A), the activation energy E_A of the system will be evaluated.

Chapter 3

Experimental Basics

This chapter is mostly concentrated on the description of the spectroscopic set-up used to perform photoluminescence (PL) measurements, along with a short introduction of the devices implemented. Experimental setup used to perform polarization measurements and time resolved measurements, in presence or absence of external magnetic fields, are also presented. Furthermore, a short overview of the sample preparation method used to characterize single quantum dot (SQD) lines are discussed.

3.1 Experimental methods

The PL measurements were performed in the following way. After the laser has been focused on the sample, photoluminescence was generated and focused onto the entrance slit of a spectrometer. The spectrometer is composed of a monochromator and a liquid-Nitrogen (LN₂) cooled CCD camera. The PL goes through the spectrometer's slit (normally ~ 50 -100 μm opened) and is reflected by a curved mirror. The collimated beam is then diffracted by a grating, which separates the incoming light into different wavelengths. Then, the dispersed beam is re-focused by a second mirror. As a result, different wavelengths are then focused to different positions on the out-going slit. The wavelengths that go through the slit are then collected onto a liquid N₂ cooled CCD camera. The spectrum is then analysed. **CCD** stands for *charge-coupled device*, which is a piece of a silicon wafer micro-manufactured and segmented into an array of individual light-sensitive cells called "photo sites." Each photo site is one element of the whole picture that is formed, this is called a picture element or "pixel." The CCD camera used in this work has a resolution of 1100 pixels on the x-axis.

3.1.1 Micro-PL for the detection of SQD

The set-up used to resolve SQD lines is depicted in Fig. 3.1. The sample was excited by a GaN solid state continuous-wave laser emitting at 405 nm. The laser beam (LB) first passes through attenuator filters F1, then is reflected by a mirror (M) before passing

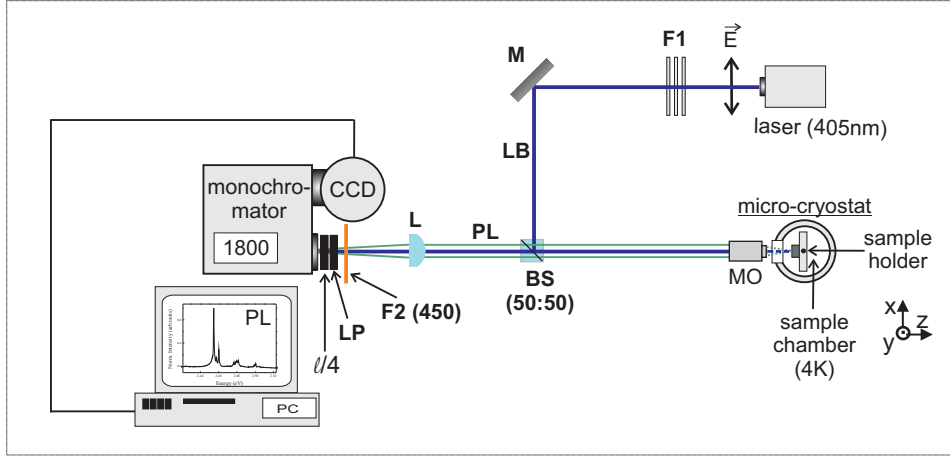


Fig. 3.1: Set-up used for micro-PL in order to resolve SQD. Following acronyms were used: L, lens; M mirror; BS, beam splitter; LB, laser beam; MO, microscope objective; LP, linear polarizer.

through a 50:50 beam splitter (BS). Afterward, the LB was reflected onto a microscope objective (MO) which then focuses the beam onto the sample. A MO with a numerical aperture ($NA=0.4$) was used to obtain a beam size of $\sim 3 \mu\text{m}$. The measurements were carried out in continuous flow LHe cryostat which is able to reach a temperature of $\sim 4\text{K}$. The photoluminescence generated from the QDs-sample is then emitted backward and, by using the confocal geometry, passes through the MO again and then toward the spectrometer. Afterward, the PL-signal was collected by a monochromator with a spherical lens with a focal length of $\sim 30 \text{ cm}$. An appropriated color filter (OG450) was used to diminish the laser wavelength.

3.1.2 Detection of linear polarized components

In order to be able to measure the linearly polarized components, π_x and π_y , from an asymmetric QD, a linear polarizer in combination with a $\lambda/4$ -plate was placed in front of the monochromator as shown in Fig. 3.1. To avoid the passage of the laser inside the monochromator a barrier filter F2(OG450) has been used, which works as a wavelengths selector cutting out the wavelengths smaller than 450 nm.

The monochromator (Jobin Yvon) has two gratings allowing to work with either 600 or 1800 lines and has a focal length of 1 m. It will resolve a single line with a 0.05 meV resolution. Then a CCD camera was used to convert the optic signal to an electric signal, which is then sent to a calculator. The measurements carried out with this setup are described in chapter 5.

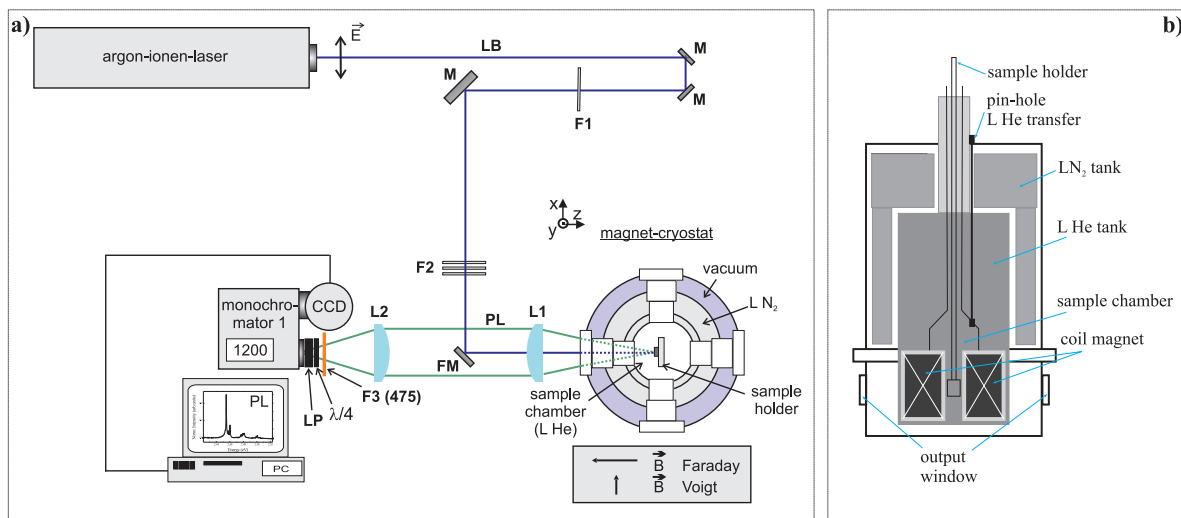


Fig. 3.2: a) Schematic top view of a set-up where an external magnetic field is applied up to 8T. The magnetic field works both in Faraday and Voigt geometry. b) A schematic cross section shows several chambers of the cryostat. Following abbreviations are used: L, lens; M mirror; FM, finger mirror; LB, laser beam; LP, linear polarizer.

3.1.3 Photoluminescence of QDs in an external magnetic field

Magnetic properties of QDs have been also studied by using another set-up, where an external magnetic field was applied. The set-up is shown in Fig. 3.2 (a). In this set of measurements an argon ion (Ar^+) laser, emitting in the visible range, was used as excitation source. In most of the measurements the 458 nm line was selected. However, a GaN solid state continuous-wave laser emitting at 405 nm was also used in some measurements. The laser beam was reflected by several mirrors, then guided onto a finger-mirror and finally focused onto the sample. The distance between sample and outer window of the cryostat was ~ 17 cm, which requires the use of a spherical lens instead of the microscope objective. In this way the lens (L1) has been used to focus the laser on the sample. The diameter of the laser beam obtained on the sample was estimated to be $70 \mu\text{m}$. The PL emitted from the QDs then passes through the L1 and, then is focused onto the monochromator by L2. Finally, a LN_2 cooled CCD camera was used to collect the spectrum.

The measurements were collected when the sample was cooled to $\sim 2\text{K}$. This temperature was obtained by flowing liquid He into the sample chamber through a pin-hole. The helium chamber is normally filled with $\sim 30 - 40$ l of He. In order to keep the system in thermal equilibrium there are two more outer chambers, one filled with LN_2 and another one under vacuum up to 10^{-6} mbar. Furthermore, the cryostat has four windows, which allows for measurements both in Faraday ($B \parallel z$) and in Voigt geometry ($B \perp z$), where z is the direction perpendicular to the surface of the sample.

However, in this work only measurements in Faraday geometry were executed. In the lower part of the cryostat magnet coils are present, which allow to generate magnetic fields up to 8T.

3.1.4 Detection of circular polarized components

When a magnetic field is applied, circular polarized components of the PL can be detected. In particular, the condition $\Delta m_l = +1$ refers to σ^+ , whereas the condition $\Delta m_l = -1$ refers to σ^- , with m_l the angular magnetic quantum number. In order to resolve experimentally the circular polarized components (σ^+ and σ^-), the light emitted from the QDs was collected through a linear polarizer and a $\lambda/4$ -plate, that were placed in front of the cryostat. The $\lambda/4$ -plate was kept constant at 45° and the linear polarizer were rotated between 45° and 135° , which allowed thus a selection of σ^+ and σ^- polarized lighth, respectively. Afterward, a spectrometer, shown in Fig. 3.2 (a) was used to analyze the two circular polarized components. These measurements were applied for the investigations of Zeeman splitting and diamagnetic shifts of QDs, which will be discussed in chapter 8.

In order to study more systematically the degree of circular polarization (DCP) of the QDs a 50 kHz photoelastic modulator operating as a $\lambda/4$ -plate in combination with a linear polarizer was placed in front of the monochromator.

3.2 Time resolved measurements

In order to obtain a complete overview of the QDs properties, the time evolution of the electron - hole annihilation (exciton lifetime) was collected by the pico-second setup described in Fig. 3.3. An Ar^+ ion laser has been used to pump a Ti-Saphire laser emitting infrared light, LB2, between 840 - 1000 nm and with a repetition rate of 82 MHz, which corresponds to a pulse to pulse duration of ~ 12 ns. The Ti-Saph laser was able to generate laser pulses in two operating modes, picosecond and femtosecond, that are 1 - 2 ps and 80 - 200 fs, respectively. If a second harmonic generator BBO crystal was used, it was possible to generate light in the visible range. Indeed, the BBO crystal or beta BaB_2O_4 is a non linear optical crystal, that is used in order to excite photons in the visible to UV range.

After the laser energy was doubled in the BBO crystal the laser beam passed through a BG 39 bandpass filter, which block all the residual infrared light still existing after the BBO crystal (see Fig. 3.3). Next, the produced visible laser beam, LB3, passed through a gradual attenuator filter (GF), which was used to continuously attenuate the power of the laser. Later on, LB3 is reflected by several mirrors and finally, by a finger mirror (FM) reflected toward the cryostat. By the use of a lens, the LB3 is focused onto the sample, which is placed inside the cryostat and cooled to $\sim 2\text{K}$. The PL generated from the sample is then redirected backward toward the

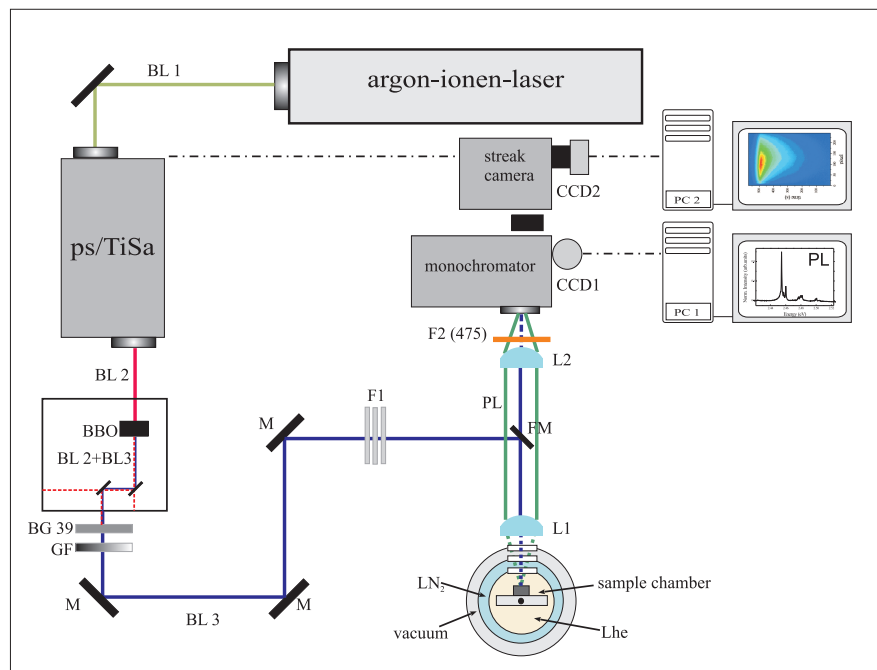


Fig. 3.3: Pico-second setup used to detect the exciton lifetime of MQDs. An Ar^+ ion laser beam (LB1) has been used to pump the Ti-Sapphire laser operating in the picosecond mode. The infrared light (LB2), emitted from the Ti-Sa laser, is doubled by a non-linear BBO crystal. Thus a visible laser light LB3 is generated. Finally, by the use of a streak camera the lifetime of QDs, excited by BL3, were analysed. Following abbreviations are used: L, lens; M mirror; FM, finger mirror; LB, laser beam; GF, linear filter.

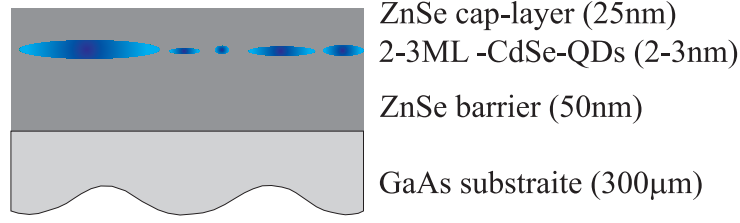


Fig. 3.4: Typical sample structure of CdSe/ZnSe heterostructure. The 2-3ML CdSe QDs embedded between the ZnSe matrix have a random size and material distribution.

spectrometer. The lens L2, having a focal length of ~ 20 cm, allows to focus the PL in the monochromator.

By this configuration, it is possible to analyse the PL energy of MQDs or SQDs, as described for the previous set-up. However, this set up provides the redirection of the PL toward the streak camera. In this manner, the lifetime of the PL can be also collected. The streak camera has a resolution time of 20 ps.

3.3 Sample fabrication

The QDs investigated in this work are composed of CdSe layers embedded in a ZnSe matrix, as shown in Fig. 3.4, which are formed by molecular-beam-epitaxy (MBE). It includes 2-3 ML of CdSe, which is grown on top of a 50 nm thick ZnSe barrier and a 300 μm thick GaAs substrate. The QDs are protected by the deposition of a ZnSe cap layer 50 nm thick. The QDs formed have a height of 1.5-2 nm and 8-20 nm in-plane extension. The QDs density is about $\rho = 10^{11} \text{ cm}^{-2}$. For more details about the growth conditions of the samples studied, see appendices C, D and E. The respective results, obtained with the above samples, are described in the later chapters.

3.3.1 Single quantum dot detection

The large QDs densities and the size distribution lead to a broad photoluminescence. Then, in order to be able to resolve a SQD, the number of excited dots were reduced by fabrication of mesas structures. In Fig. 3.5 a comparison between the characterization of multi QDs (MQDs) and SQD lines are shown. Fig. 3.5 (a) shows the broad PL spectrum recorded from MQDs, with a sketch of the typical sample during the excitation (see Fig. 3.5 (b)). On the other hand, Fig. 3.5 (c) shows the μ -PL spectrum of SQD when only few QDs have been excited. In this last case the excited area contains only few QDs delimited by the mesa, as shown in Fig. 3.5 (d).

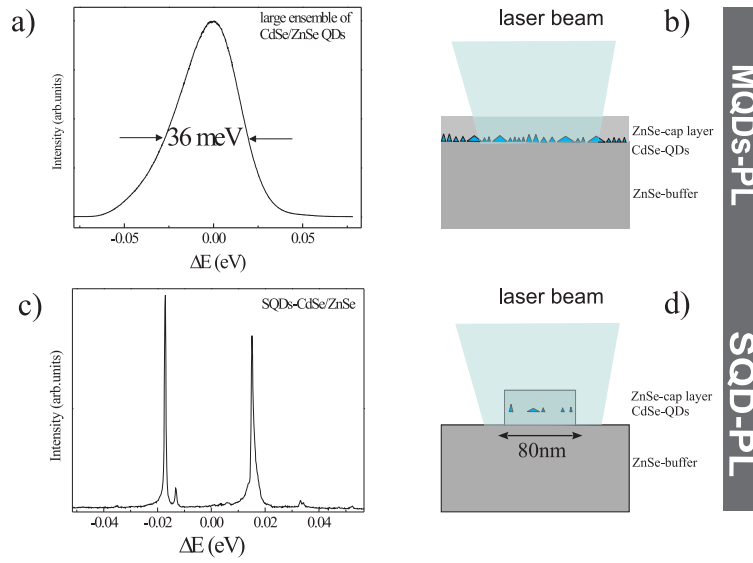


Fig. 3.5: (a) A broad PL is photo-generated by (b) excitation of an ensemble of multi QDs (MQDs). (c) SQD lines are selected by the (d) fabrication of a small mesa (~ 80 nm large).

3.3.2 Mesas fabrication

Usually, the fabricated mesas have sizes ranging from $100 \mu\text{m}$ to 60 nm , with respective distances between different mesas chosen accordingly of the needs. When the setup in use has a microscope objective that can lead to a laser beam with a size of $\sim 5 \mu\text{m}$, the distance between the mesas can be of $\sim 10\text{-}20 \mu\text{m}$. On the other hand when the size of the laser beam is about $50\text{-}70 \mu\text{m}$ the distance between the mesas must be much larger if one wants to avoid multi-mesa excitation.

A typical method used to fabricate mesas is schematically shown in Fig. 3.6. The mesa fabrication requires spin coating a thin film of polymeric material, such as a positive resist (PMMA) (Fig. 3.6 (b)). The part of the resist exposed to the electron beam (Fig. 3.6 (c)) modifies the chemical properties of the resist, which then can be selectively removed from the sample by using an appropriate solution. Thus a resist mask is obtained (Fig. 3.6 (d)). However, the PMMA mask is not sufficient to protect the sample from the chemical etchant, and a layer of titanium (Ti) is deposited for further protection. In this way, the Ti-layer is not only deposited on the resist, but also in the inner part of the mask previously formed (see Fig. 3.6 (e)). By selective removal of the resist, the Ti on the top of the resist is removed and then only a Ti-mask remains on the sample. This process is known as the *lift-off*. In Fig. 3.6 (f), the last step of the fabrication process is shown, where a mesa is formed after the wet chemical etching is performed. Accordingly with the size of the mesa fabricated the

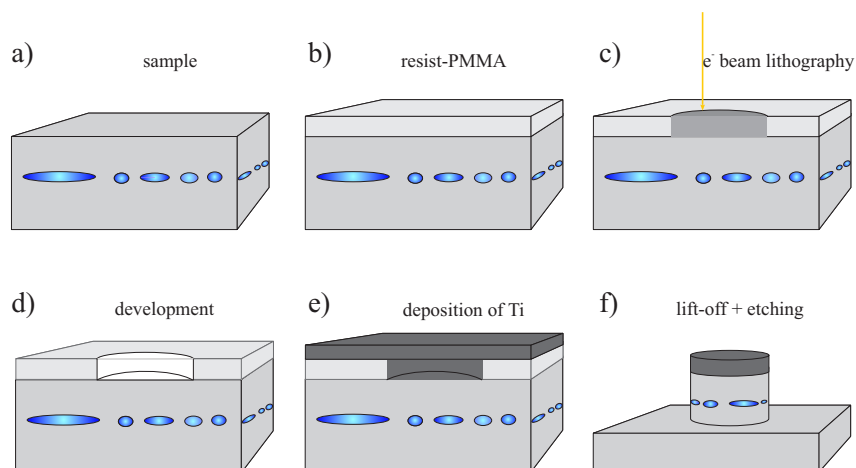


Fig. 3.6: a) Sketch of processes to build mesa structure, starting from an as-grown sample. b) Deposition of the positive resist (PMMA). c) Lithography by exposing the sample with an electron beam. d) A resist-mask is obtained. e) Further deposition of Ti-layer. d) The selective removal of the PMMA leads to obtain a Ti-mask, known as lift-off. The mesa so obtained has a low number of QDs.

number of active QDs carried by the mesa will change. After the mesa fabrication the sample is characterized by the use of a liquid helium (LHe) bath or cold-finger cryostat for PL detection.

3.4 Rapid thermal annealing

The main work of this thesis deals with thermal annealing (TA) of QDs samples. The thermal annealing of the QDs-sample was done in two ways, one known as rapid thermal annealing (RTA) process, where the RTA process consisted of a fast temperature ramp, followed by a temperature plateau of t_A (annealing time) at T_A (annealing temperature). During the annealing, the sample was placed inside a graphite box in order to ensure a fast heating as well as a fast cooling down of the sample. The above instrument allowed minimum annealing temperatures of 230 °C. For this reason a second way to perform rapid thermal annealing was used. It consist in using a hot-plate during the heating process and a cold-plate to cool down quasi instantaneously the sample. During the heating and the cooling process N_2 gas was blown on the surface of the sample for 30s. In this way a rapid quench of the annealing process was ensured. Also water condensation on the sample was therefore avoided.

This alternative method allowed to investigate the single quantum dot (SQD) behavior when several annealing steps were performed. Indeed, it was observed that very low temperature (around 100°C) was enough to change the energy position of single QDs lines. Most of the thermal annealing were executed by this method. The anneal-

ing was performed in the range of temperatures between 100 °C and 220 °C in steps of 20 °C for an annealing time of 30 s.

Chapter 4

Method to calculate the activation energy

4.1 Eigen energy of annealed quantum dot

Hereby the method used to calculate the energy of electron and hole states for thermally annealed quantum dots by using the second Fick's law is presented. In order to simplify the problem, QDs with cylindrical shape (symmetric group D_{2d}) are considered. The Hamiltonian can be expressed as in eq. 2.5 neglecting the Coulomb interaction. Therefore, the Hamiltonian is written as:

$$H = -\frac{\hbar^2}{2m_e}\Delta_e^2 - \frac{\hbar^2}{2m_h}\Delta_h^2 + V_e(r) + V_h(r) \quad (4.1)$$

where the first two terms describe the kinetic energies of the electron and hole and the third and fourth terms are the electron and hole potentials, respectively.

In order to calculate the exciton eigen energies of a QD subject to a thermal treatment, the Cd and Zn contents after any annealing step have to be evaluated. The early step-potential changes size and shape when the interdiffusion between the barrier and the QD take place. In order to evaluate numerically the exciton eigen energies at any TA step, the G-J solution is used to describe the potential profile, which was previously calculated for a slab of material (eq. 2.22). By taking the complementary of eq. 2.22 and subtracting it from the unity, one obtains an equation describing 100% of Zn-content in the barrier and 100% of Cd-content inside the QD. When TA is performed, part of the Zn diffuses from the barrier inside the QD and part of Cd diffuses from the QD into the barrier. In this way the potential in the growth direction becomes:

$$C(z, t) \equiv V(z) = 1 - \frac{C_0}{2} \left[\operatorname{erfc} \left(\frac{z - L_z/2}{2L_D} \right) + \operatorname{erfc} \left(\frac{z + L_z/2}{2L_D} \right) \right], \quad (4.2)$$

where L_z is the size of the QD, $L_D = \sqrt{Dt_A}$ the diffusion length and C_0 the Cd-content before TA. In the L_D expression, D is the diffusion coefficient and t_A is the annealing

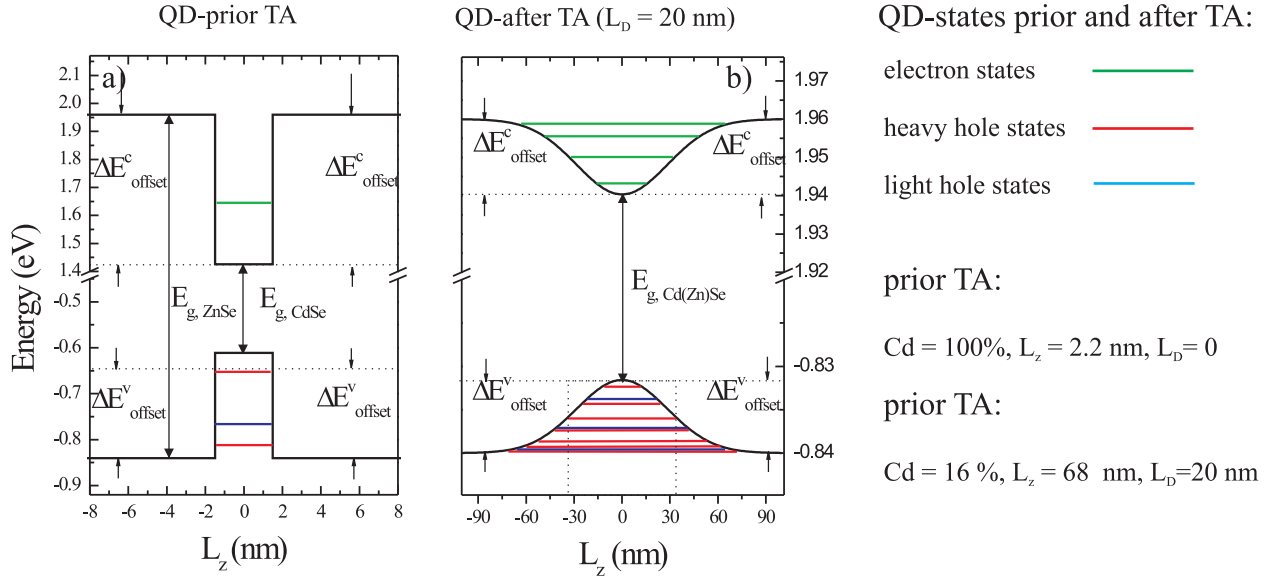


Fig. 4.1: (a) Electron and holes states prior to TA. (b) Potential profile of a QD thermally annealed. The diffusion length is $L_D = 2$ nm. The number of electron and hole states are strongly increased with narrowed energy spacing compared to the case prior to TA.

time. By varying either t_A or T_A , $C(z,t)$ changes accordingly to the Cd/Zn content in the QD. Indeed, when the annealing time, t_A , or annealing temperature, T_A , increase, L_D increases as well and, consequently, the potential changes its shape, accordant to eq. 4.2.

The PL energies obtained experimentally were used in order to evaluate the activation energy. By the use of eq. 4.2 it is possible to have different potentials profiles by varying L_D . Since different potential profiles refer to different QDs, also different electron and hole energies can be calculated. As a result, varying the potential profile means to vary the exciton energy. By doing so a correlation between the PL-energies and the L_D 's can be found. In Fig. 4.1 (a) and (b) an example of the QD-potential as a variation of the Cd/Zn content versus the growth direction is shown. Figure 4.1 (a) refers to a QD box-potential typically applied for a QD prior to TA ($L_D \rightarrow 0$), whereas the shallow potential in Fig. 4.1 (b) refers to the QDs-potential after TA ($L_D \neq 0$). As can be noted from the above calculation, when L_D increases, the energy gap increases as well. In this figures only $L_D = 0$ and $L_D = 20$ nm are considered for an initial QD-size, $L_z = 2.2$ nm, and an initial Cd content, $C_0 = 100\%$.

In addition, prior to TA a typical step like profile is shown with only one ground electron state (green lines) in the conduction band, and heavy hole (red lines) and light

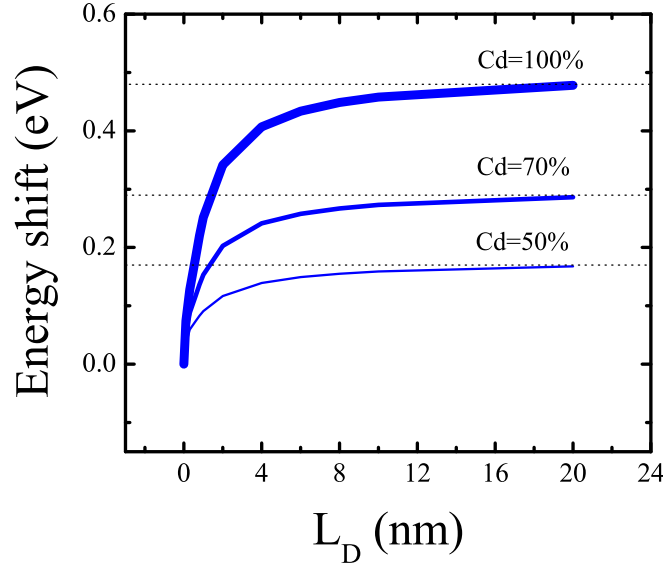


Fig. 4.2: Comparison between three characteristic curves, with different initial Cd-contents (100 %, 70 % and 50 %). The QDs-layer size has been fixed at $L_z = 2.2nm$ and L_D has been varied in small step.

hole (blue lines) states in the valence band. It should be mentioned that stress was not considered in this calculation. However, a very good agreement with data from the literature [TON94] was found. These calculations were used to fit the experimental data shown in chapter 5. Both the activation energy and diffusion lengths of CdSe/ZnSe QDs were determined.

4.1.1 Evaluation of the characteristic curves

As already mentioned in sec. 2.2 the valence states in bulk material are degenerate at $k=0$. However, when QDs are grown, the degeneracy at $k = 0$ is lost due to the strong confinement. It should be mentioned that such loss of degeneracy might change with the size of the QDs. In the present work, an energy difference between the lowest light hole and the highest heavy hole is ~ 100 meV for as grown CdSe QDs. In such configuration, the light and the heavy hole do not interact with each other and consequently, the exciton is formed with the electron and the heavy hole.

As mentioned above, when the dot undergoes a thermal treatment the potential is smeared out and the reduced confinement induces energetically narrowed states. The decrease of the interlevel states can lead to emission from excited states. Also the interaction between light and heavy holes is enhanced [HEI88, TWA85, TWA87,

MAH70]. In chapter 7 of this thesis it will be shown, that by varying both the size and the material concentration, the light and the heavy hole can mix in such way that the hybrid hole state might have a strong light hole character.

By the use of the above calculation, a correlation between the PL energies and the L_D 's was obtained and shown in Fig. 4.2 further referred to as characteristic curve. The characteristic curve changes with the initial QD-size and material content. The curves are calculated for three different initial Cd-contents, 100 %, 70 % and 50 %. The choice of the parameter used to calculate the characteristic curve is related to the best measured energies of thermally annealed QDs.

Chapter 5

Optical characterization of CdZnSe QDs

5.1 Structuring of the sample

The results on thermal annealed QDs are hereby presented. The samples defined as S1 and S2 are described in Appendix B and C. As discussed in the first chapter, II-VI semiconductor QDs allow the observation of fine structure splitting (FSS), biexciton binding energy (BBE) and charged exciton emissions. In this respect, a study of CdSe/ZnSe QDs is presented, whose morphological nature has been altered by ex-situ thermal annealing.

5.1.1 QDs-formation

In lattice-mismatched semiconductor heteroepitaxy [LIT01, PER00], the formation of self-assembled quantum dots is driven by elastic strain relaxation. Elastic strain results due to the different lattice constants of the substrate and the QD-forming materials. For example, the lattice mismatch between InAs and GaAs is 7%. Elastic relaxation of strain leads to a morphological re-organization of the growing surface, resulting in the formation of well-defined 3D nanostructures [AKI07, CHA98]. This mechanism of epitaxial growth is known as the Stranski-Krastanow (SK) transition and has been successfully employed to realize QDs of several heterosystems. Though the lattice-mismatch between ZnSe and CdSe is also 7%, the SK mechanism has not been observed for this heterosystem. The resultant structures are appropriately described as inhomogeneous quantum wells of ternary CdZnSe. The formation of 3D islands is hindered by other routes of strain relaxation in this case, i.e. through interdiffusion [KIM00] or by dislocation [LIT01] formation. Nonetheless, the local compositional inhomogeneities of the ternary QWs (Cd-rich inclusions) confine electrons and holes (or excitons) three-dimensionally, as in ideal QDs. Such QDs, formed in case of the CdSe/ZnSe heterosystem are also known as natural QDs [ZRE94]. Description on the

morphology of such QDs and further information about them can be found in Appendix B.

5.1.2 Single QD photoluminescence

A major part of the work done in this thesis involves the study of single QDs. Access to single QDs by optical spectroscopy requires fabrication of small mesas containing only a few QDs. For construction of mesas a combination of electron beam lithography (EBL) and wet-chemical etching has been used, as described in chapter 3. The smallest mesa fabricated in this work measured 80 nm in diameter.

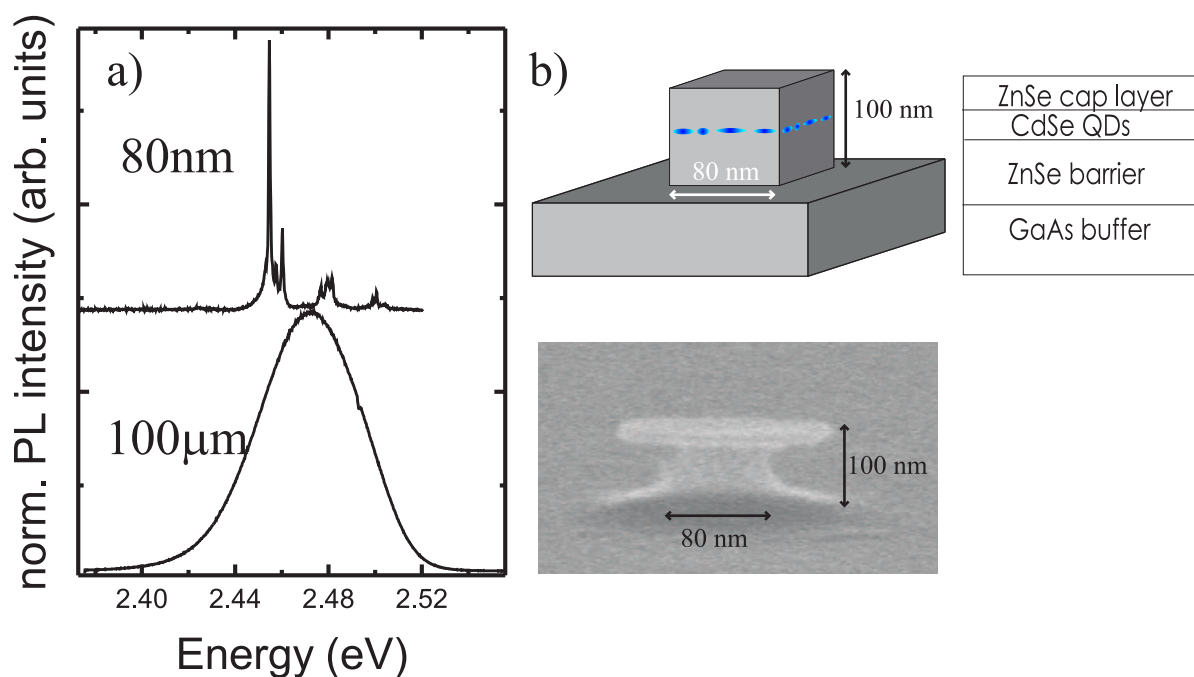


Fig. 5.1: (a) PL spectra recorded from a 100 μm and a 80 nm mesa. (b) A sketch of a 80-nm-mesa (upper panel). The blue region represents the CdSe QD-layer. SEM image of the mesa, prior to Ti mask removal, is shown in the right bottom panel.

In Fig. 5.1 (a) PL spectra from two different mesas, of size 100 μm (bottom spectrum) and 80 nm (top spectrum) are compared. For a 100 μm mesa the excitation beam probes a large number of QDs, which vary in size, morphology and composition. Due to this spread in the physical properties of the QDs, their ground-state energies also exhibit a dispersion, which is reflected in the inhomogeneously-broadened (Gaussian

profile) PL spectrum. On the other hand for the 80-nm mesa only a few QDs are probed and the PL spectrum deconvolutes to sharp emission lines, due to individual QDs. A sketch of the 80-nm mesa is shown in Fig. 5.1 (b), upper panel and a SEM image of the real mesa (prior to removal of the metal mask) is shown in the lower panel. The blue region of the sketch corresponds to the CdSe QD-layer.

5.2 Annealing of CdZnSe QDs

As mentioned in chapter 1, this thesis deals primarily with the evolution of CdSe/ZnSe QD-properties due to post-growth thermal annealing (TA). For the first investigations, large ensembles (without fabrication of any mesa) were annealed at different annealing temperatures, T_A , ranging between 300-550 °C, for a constant duration, t_A , of 10 s. PL was recorded using the set up described in section 3.2. Figure 5.2 shows the PL spectra of the entire series of samples. For ease of analysis, the spectra are displaced on the vertical axis and normalized, to the maximum intensity.

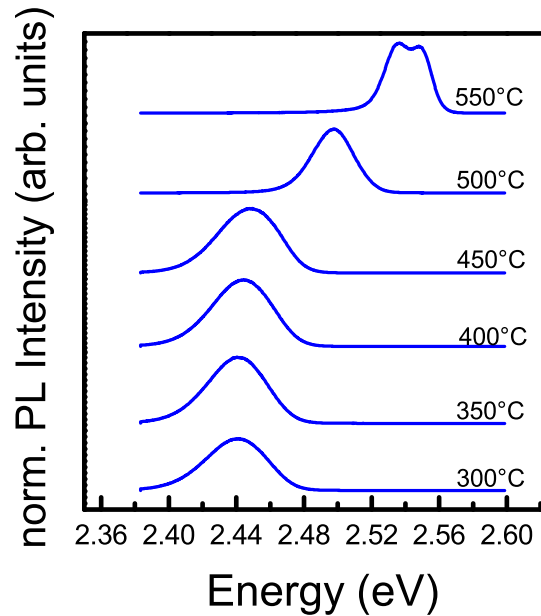


Fig. 5.2: Photoluminescence spectra of QDs annealed for the same duration $t_A = 10$ s at different annealing temperatures, varied in steps of 50 °C, starting from $T_A = 300$ °C to 550 °C. At $T_A = 300$ °C, the QD emission is centered at 2.44 eV. Up to 400 °C, the spectra remain almost unchanged. For $T_A > 450$ °C, a pronounced blue shift of the photoluminescence peak is observed.

Thermal annealing up to $T_A = 400$ °C leads to no significant change in the PL of the ensemble of QDs. However, a drastic blue shift of up to 100 meV is observed for T_A ranging between 450-550 °C. Prior to TA, the PL peak is inhomogeneously broadened with a maximum registered at 2.44 eV and a FWHM = 36 meV. Such broad emission is typical of CdSe based QDs, where the formation of QDs results essentially from composition fluctuations within a ternary QW [OUA90]. The blue shift for higher T_A are explained by annealing-induced Cd-Zn interdiffusion between the QDs and the surrounding matrix. Interdiffusion changes an abrupt interface, prior TA, to a graded interface, after TA. A numerical solution of a Schrödinger equation was used to extract diffusivity values from the experimental data, as explained in section 2.8 and more extensively in chapter 4. The concentration function uses standard error function:

$$C(z, t) = 1 - \frac{C_0}{2} \left[\operatorname{erfc} \left(\frac{z - L_z/2}{2L_D} \right) + \operatorname{erfc} \left(\frac{z + L_z/2}{2L_D} \right) \right] \quad (5.1)$$

where L_D is the diffusion length and L_z the size of the QDs in the growth direction, while C_0 is the Cd-content prior to TA. This equation provides potential profiles at different TA. In this way a correlation between the ground exciton energy and the diffusion parameters was made. By use of the Arrhenius law it is possible to determine the activation energy, E_A , from the slope of the plotted diffusion coefficient, D , as a function of the $1/kT_A$ (see Fig. 5.3). The activation energy was determined to be 2.2 eV, which is in good agreement with the literature [TON94].

In addition to the blue-shift, the efficiency of the QDs-luminescence is considerably enhanced due to TA. As seen in Fig. 5.4 (a), the integrated intensity of the QD-luminescence, for a constant excitation power, increases with increasing T_A . For the range of T_A between 300 °C and 450 °C, a continuous increases of the PL intensity is observed. This is the range of T_A wherein no PL-energy-shift was observed. Similar results were found also for the InGaAs heterosystem [LEO97], but the observations were not extensively discussed. In absence of a spectral shift of the PL-energy, the enhancement of the PL-intensity, might not be attributed to any diffusion-related process. Instead, it might be assigned to annihilation of point defects and particularly vacancies [HAR05, OSH92, YAB88, MAR93, KOT91, LIP96].

On the other hand, for $T_A = 450 - 550$ °C, a drastic PL-blue-shift is seen. Additionally, from Fig. 5.4 (b), it is seen that in the range between $T_A = 300 - 450$ °C, the FWHM is constant (at 36 meV) and beyond $T_A = 450$ °C, it reduces strongly, down to 12 meV. While the PL-blue-shift indicates the onset of Zn-Cd interdiffusion, the narrowing of the spectra strongly suggests suppression of QD-size distribution.

In order to have more information about the changes that TA induces on the optical properties of QDs, measurements of the exciton decay time were performed. Exciton lifetimes for the annealed samples were compared with those of the unannealed (as-grown) samples. Fig. 5.5 (a) shows the time evolution of the spectrally-integrated-PL-intensity of the unannealed (as-grown) sample and that annealed at $T_A = 500$ °C.

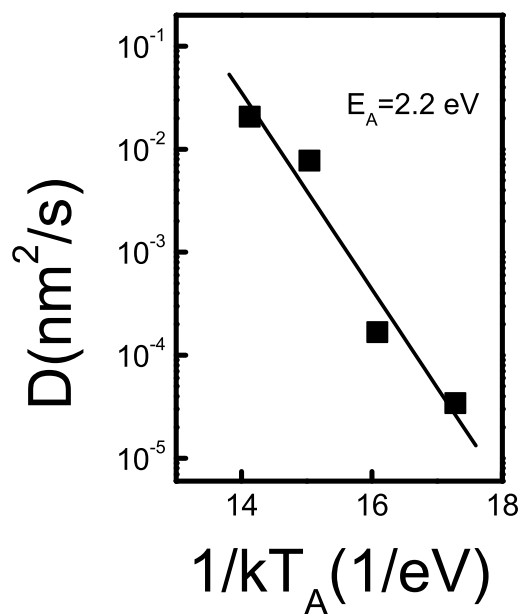


Fig. 5.3: Determination of the activation energy, E_A , by fitting the experimental data for an ensemble of CdSe/ZnSe QDs.

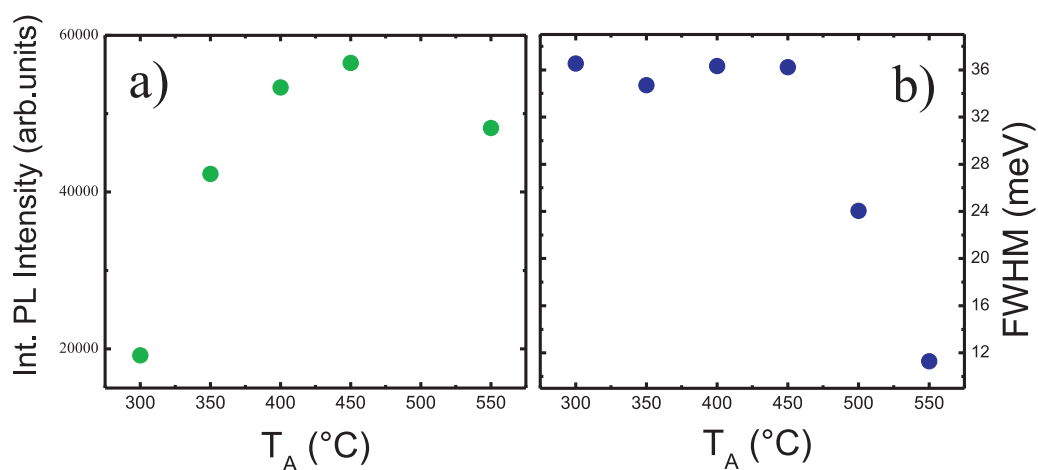


Fig. 5.4: (a) Variation of PL intensity versus the annealing temperature. (b) The corresponding variation of the FWHM of the spectra.

To determine the exciton recombination time, one needs to consider the rate equation describing the electron-hole recombination process. The rate equation for the exciton recombination can be described as:

$$\frac{dw_X}{dt} = \frac{w_X}{\tau_{X^*}} \quad (5.2)$$

where w_X is the probability of forming an exciton in a quantum dot and $1/\tau_{X^*} = 1/\tau_X + 1/\tau_{X_S}$, with τ_X , the radiative exciton lifetime and τ_{X_S} the spin relaxation time. However, it is known that $\tau_{X_S} \gg \tau_X$, thus $\tau_{X^*} \cong \tau_X$, in agreement with Puls and Henneberger [PUL97]. By using the rate equation, it is possible to fit the experimental

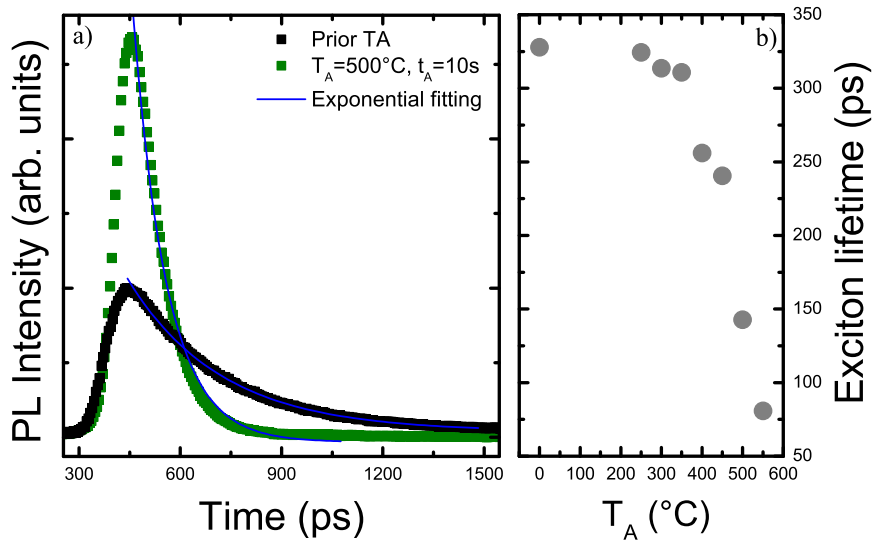


Fig. 5.5: (a) Time evolution of the integrated PL intensity for an unannealed sample and for an annealed sample, with $T_A = 500$ °C and $t_A = 10$ s. From the exponential fitting of the decaying part of the plots, the exciton decay time is determined. (b) A plot of all the exciton decay times calculated for all samples thermally annealed at different temperature, between 300 °C and 550 °C.

data plotted in Fig. 5.5 (a) and extract the exciton lifetime for the different annealed samples. The exciton decay time for the unannealed sample TA has a value of (330 ± 20) ps and stays almost constant up to $T_A = 350$ °C. Beyond this, the exciton decay time strongly drops down to 80 ps, as seen in Fig. 5.5 (b).

The series of annealing at different temperature shows that the PL intensity is enhanced almost linearly up to $T_A = 450$ °C, whereas the exciton decay time decreases. This observation is a sign of an enhanced quantum efficiency due to annealing. Several

reasons for an improved PL emission can be given. One reason could be the annihilation of point defects in the surrounding of the dots, which in turn reduces the non-radiative recombination channels and enhance the QD luminescence efficiency. Another reason could be the enhancement of oscillator strength Γ_{QD} , as suggested by the reduced exciton decay time, since $\tau_X = \hbar/2\Gamma_{QD}$. In Fig. 5.2 is shown that the PL-energy is not shifted up to $T_A = 450$ °C, meaning that in this range of measurements the QDs size and composition are not modified. Since, it is known that the oscillator strength is a function of the QDs size [FON05, GIL02], it can be concluded that the second hypothesis does not support the above results. In conclusion, TA improves the QDs luminescence efficiency by decreasing the defects around the dots, and thereby reducing the probability of Auger-like effects.

5.3 Enhanced diffusion of single CdZnSe QDs

A series of PL spectra, recorded from an 80-nm-wide mesa after each TA step, as well as prior to annealing, is presented in the left panel of Fig. 5.6. While the bottom-most spectrum (prior to TA) is dominated by a single-QD exciton emission line, further referred to as the A line, additional luminescence features appear at higher energies, immediately after the first TA step. However, the A line can be clearly traced in the spectrum after each TA step. In the subsequent steps of TA, both the A line and the additional lines at higher energies show similar blueshifts, indicating a gradual interdiffusion of Cd and Zn between the studied single QD and the surrounding ZnSe matrix. The blueshift is low up to $T_A = 180$ °C, beyond which, however, it increases more rapidly. For the present mesa, the observed blueshift after annealing to temperatures up to 240 °C is about 100 meV. Interestingly, such large blueshifts for this range of TA is observed only in the spectra of the small mesas. For 10- μm -wide mesas similar TA processes result in no appreciable blueshift in a comparable range of TA values, as shown in the right panel of Fig. 5.6. In this case, blueshifts in the order of 10 meV were recorded for $T_A = 400$ °C and beyond, from which E_A for interdiffusion in large mesas was extracted. In the corresponding inset, the PL blueshift ΔE of the A line (80 nm mesa), a single-QD line in a 180-nm-wide mesa (not shown), and the peak maximum of the 10 μm mesa are plotted as a function of TA. The TA-induced blueshift is larger the smaller the etched mesa is. This observation is associated to an enhanced cation intermixing in small mesas. However, unlike in Ref. [WEL01], where enhanced intermixing in small mesas has been attributed to TA-induced generation of defects at the upper surface of the sample (due to different thermal expansion coefficients of the epitaxial semiconducting layers and the Ti mask), the dependence of the energy shift on the mesa sizes in this case rather suggests that the etched sidewalls contribute to the enhancement of cation interdiffusion. Possible origins are strain gradients in the vicinity of the sidewalls, induced by partial relaxation of elastic strain or the presence

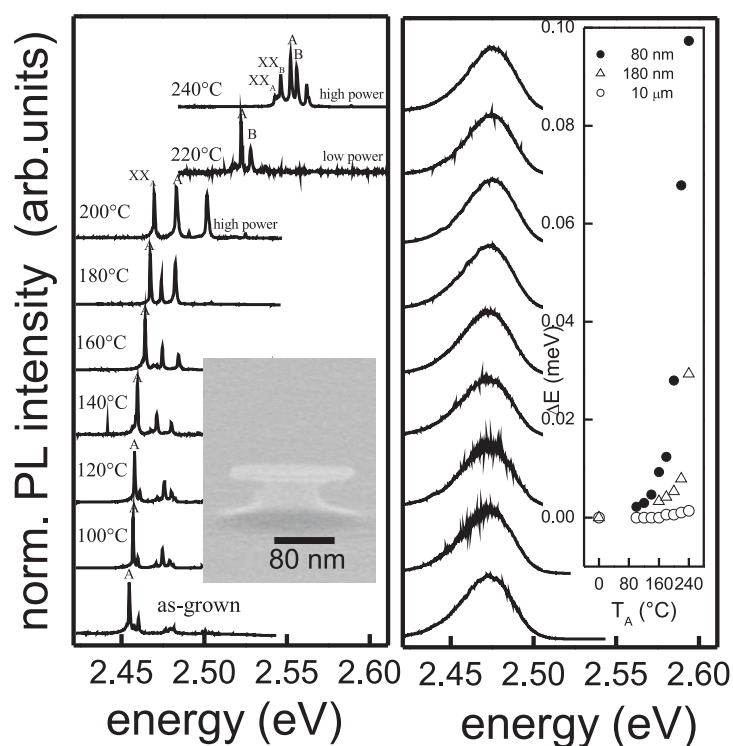


Fig. 5.6: Left panel: Photoluminescence spectra of a small QD ensemble embedded in an 80-nm-wide mesa, annealed at different temperatures between 100 and 240 °C for 30 s. The inset shows a scanning electron microscope image of the mesa (side view), taken prior to mask removal. Right panel: Photoluminescence spectra of a 10- μm -wide mesa which was processed and annealed in an identical manner as the 80-nm-wide mesa. The inset shows the energy shift of the A line (80 nm mesa), a line in the spectrum of a 180-nm-wide mesa, and the emission maximum corresponding to the large mesa (10 μm), vs the annealing temperature T_A .

of defects at the side walls.

In addition to the pronounced blueshift, biexcitons in the annealed QDs were observed. In order to identify biexciton recombinations, emission intensities have been recorded as a function of the excitation power, which was ramped to a maximum of $P = 20 \text{ kW/cm}^{-2}$. For the present mesa no biexcitons were observed prior to annealing. Also in the spectra of other mesas biexciton lines were detected only very rarely without TA. A different behavior was found for thermally annealed mesas. In Fig. 5.6 (left panel) a new emission line (labeled XX) is seen on the low energy side of the A line, for $T_A = 200 \text{ }^\circ\text{C}$ and $P = 20 \text{ kW/cm}^{-2}$. This XX line, e.g., corresponding to $T_A = 220 \text{ }^\circ\text{C}$, vanishes for small excitation powers. At even higher annealing temperatures additional emission lines appear for high excitation powers; e.g., the B line in the spectra for $T_A = 240 \text{ }^\circ\text{C}$ is accompanied by an additional XX_B line for high excitation power. In Fig. 5.6 the integrated intensities of the A line and the XX_A line is plotted as a function of the excitation power. The straight lines $I \sim P$ and $I \sim P^2$ are depicted as a guide to the eye. The integrated intensity of the A line depends approximately linearly on P , whereas the integrated intensity of the XX_A line scales quadratically. Such a behavior is typical for excitons and biexcitons, respectively [ZAI01, HER97]. Thus we associate the XX lines to biexciton emissions. The first biexciton emission line was observed (XX_A line) after TA at $200 \text{ }^\circ\text{C}$. The corresponding binding energy, which is the energy difference between the exciton and the biexciton lines, was determined to be 14.6 meV , a value which is notably smaller than the biexciton binding energies reported for as-grown CdSe QDs [KUL99, XIE01]. At an even higher annealing temperature $T_A = 240 \text{ }^\circ\text{C}$, a biexciton binding energy of less than 10 meV was observed. This behavior clearly indicates an increase in the quantum dot size [HER97] due to TA. The TA-induced lowering of QD confinement has been recently observed also by a reduction of exciton lifetime [MAC03-1].

5.3.1 Model

For the analysis of the TA-induced energy shift, a change in the QD size and the effective band gap was considered. Since the lateral dimensions of the CdZnSe QDs are considerably larger than their heights L_z , it was assumed that the quantum confinement and its variation due to TA is predominantly determined by the QD height. Typical values of L_z range between 1 and 2 nm with lateral dimension of about 20 nm . Therefore, the diffusion process in one dimension was determined, i.e. in the z direction (direction of growth). The diffusion coefficient $D(T)$ is given by the Arrhenius law:

$$D(T_A) = D_0 \exp\left(-\frac{E_A}{k_B T_A}\right), \quad (5.3)$$

where E_A is the activation energy of the Zn-Cd interdiffusion, T_A , the annealing temperature, k_B the Boltzmann constant and D_0 a prefactor. $D(T)$ in turn is related

to the diffusion length L_D by the relation

$$L_D = \sqrt{Dt_A}, \quad (5.4)$$

where t_A is the annealing time. To determine L_D from the PL blueshift, a concentration profile of Cd in the z direction

$$C(z, t) = 1 - \frac{C_0}{2} \left[\operatorname{erfc} \left(\frac{z - L_z/2}{2L_D} \right) + \operatorname{erfc} \left(\frac{z + L_z/2}{2L_D} \right) \right] \quad (5.5)$$

was taken into account with C_0 as the initial Cd content (prior TA) and $\operatorname{erfc}(z)$ as the error function. Initial values of $L_z = 1.5$ nm and $C_0 = 71\%$ were chosen based on the fact that the corresponding calculated energy fits very well to the experiment. In a first step we have calculated the energy shift ΔE versus the diffusion length, L_D , using a Schrödinger equation solver, taking into account the diffusion-modulated energy profile according to eq. 5.3.1. With increasing L_D , a funnel-like potential profile evolves. Then, by comparison of the calculated $\Delta E(L_D)$ with the experimental data, the diffusion length corresponding to each value of $\Delta E(L_D)$ was determined. As the annealing temperature was varied for different TA steps, one can extract the diffusion coefficients only from the change of the diffusion length between two consecutive TA steps using eq. 5.3.1. From the slope of the $D(1/k_B T_A)$ vs $1/k_B T_A$ plot on a semilogarithmic scale, the activation energies E_A for the different structures were determined (see Fig. 5.7). $E_A = 0.9 \pm 0.1$, 1.2 ± 0.1 , and 2.2 ± 0.3 eV were extracted for the 80 nm, 180 nm and the 10 μm mesas, respectively. The activation energy of the small mesa is more than a factor of 2 smaller than that measured for a large QDs ensemble. Thus, these results show that the Zn-Cd interdiffusion is enhanced significantly in small mesas.

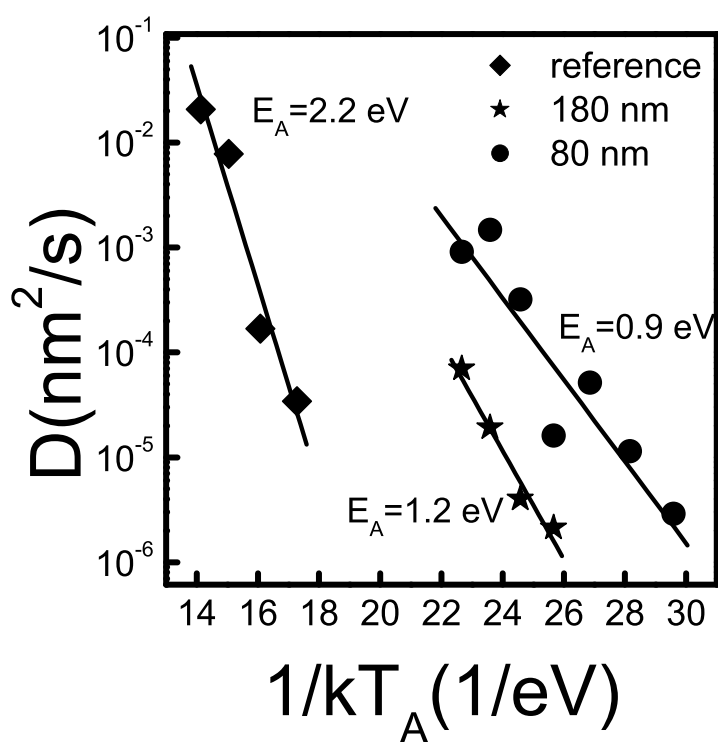


Fig. 5.7: Semilogarithmic plots of $D(T)$ vs $1/k_B T_A$ determined for different mesas.

Chapter 6

Study of the anisotropy of a quantum dot

6.1 Control of QD-isotropy by thermal annealing

By mapping the anisotropy fine-structure splitting of the exciton ground state in the luminescence spectra of individual $\text{Cd}_x\text{Zn}_{1-x}\text{Se}$ quantum dots, treated by postgrowth rapid thermal annealing (TA), a preferred in-plane axis of Zn-Cd interdiffusion has been identified. In particular, a TA-induced sign reversal of the fine-structure splitting is demonstrated. Additionally, in the annealed quantum dots, the binding energy of the charged exciton reaches a maximum value when the fine-structure splitting is minimum. The studies demonstrate that by post-growth thermal annealing the symmetry of individual quantum dot can be modulated.

6.1.1 Tuning of the QDs symmetry

A key result of the studies presented in the previous chapter is that the processing-induced defects on the sidewalls of the mesas strongly influence the Zn-Cd intermixing between the QDs and the surrounding matrix, during TA. For small mesas, this turns out to enhance interdiffusion, since the QDs are more likely to be close to the edges of the mesa. In this chapter it is demonstrated that the defects on the mesa side-walls not only change the composition and size of the QDs due to enhanced TA-induced interdiffusion, but also can strongly modify their shape. As-grown QDs are well-known to be elongated along a particular in-plane direction [AIC07, MAR07, SEG06]. On small mesas, TA introduces drastic changes in the QD-shape, changing its direction of elongation in a perpendicular axis, passing through a symmetric intermediate step. This changes of the SQD in-plane dimensions has been studied by analyzing the evolution of FSS (see sec. 2.1.4) under TA, in μ -PL spectroscopy. As mentioned in section 2.1.4, in asymmetric QDs, the EHX interaction leads to splitting of the degenerate ground state, whose emissions are perpendicularly linearly polarized. In this work TA-induced

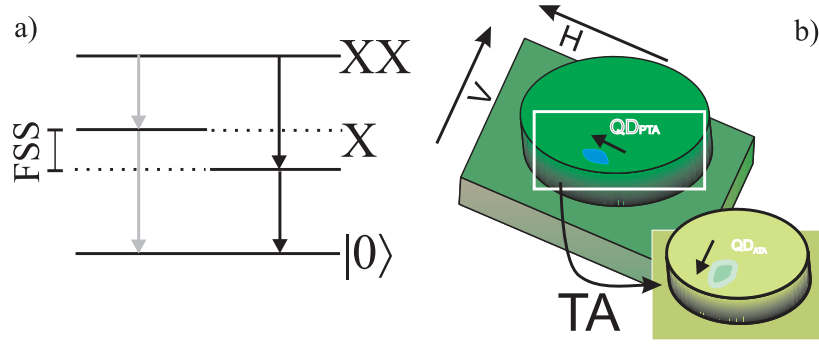


Fig. 6.1: a) X and XX recombination-scheme changing in presence of EHX-induced FSS in an asymmetric QD. b) Elongated-QD and its evolution with TA when it is within a small mesa structure. The sketch and the inset are referred to the cases prior to TA and after TA, respectively.

interdiffusion has been used to tune the QD in-plane shape and thereby the EHX interaction. The energy level scheme of the biexciton and exciton states in presence of EHX splitting of the ground excitonic state is schematically shown in Fig. 6.1 (a). Fig. 6.1 (b) shows a sketch of a small mesa with a QD, elongated along the $[110]$ (designated as H-axis). Such a QD, close to the mesa wall, after some TA-steps, changes its elongation from the H-axis to the perpendicular V-axis, through an intermediate symmetric shape. Such changes in the QD-shape can be explained with the presence of surface states formed during the fabrication of the mesa structures. In order to investigate the evolution of FSS by TA, measurements of SQDs were executed by using a linear polarizer placed in front of the monochromator, as described in section 3.3. Such measurements were performed several time for different annealing temperatures, T_A , and for QDs inside a small mesa.

Fig. 6.2 (a) shows the PL spectra corresponding to sample S1, after thermal annealing at temperatures between $T_A = 100$ - 180 °C, varied in steps of 20 °C. The annealing duration was kept constant at $t_A = 30$ s. The spectrum for $T_A = 100$ °C (bottom-most) shows emission due to a neutral exciton (X), a charged exciton (X^-), and a bi-exciton (XX). Such emissions were not seen in spectra recorded prior to TA. On further annealing at $T_A = 120$ °C, a red-shift is also observed. The shift on further annealing is on the blue side. Fig. 6.2 (b) shows the excitonic emission spectra corresponding to polarization direction (of detection) parallel to H and V axes, for TA at three different T_A values, namely 100 °C, 120 °C, and 180 °C. For $T_A = 100$ °C, the V-polarized emission is on the red side of the H-polarized emission, and this we term as positive FSS. The FSS for $T_A = 100$ °C is 0.1 meV. As T_A is increased to 120 °C, the FSS is almost zero, signifying an isotropic shape of the QD at this stage. At this value of T_A , the PL-emission is red-shifted (see Fig. 6.2 (a)) which is also related to the formation of high symmetric QDs. As the QD assumes a symmetric shape due to annealing, the initial effect is to release of strain, due to which a redshift results. By

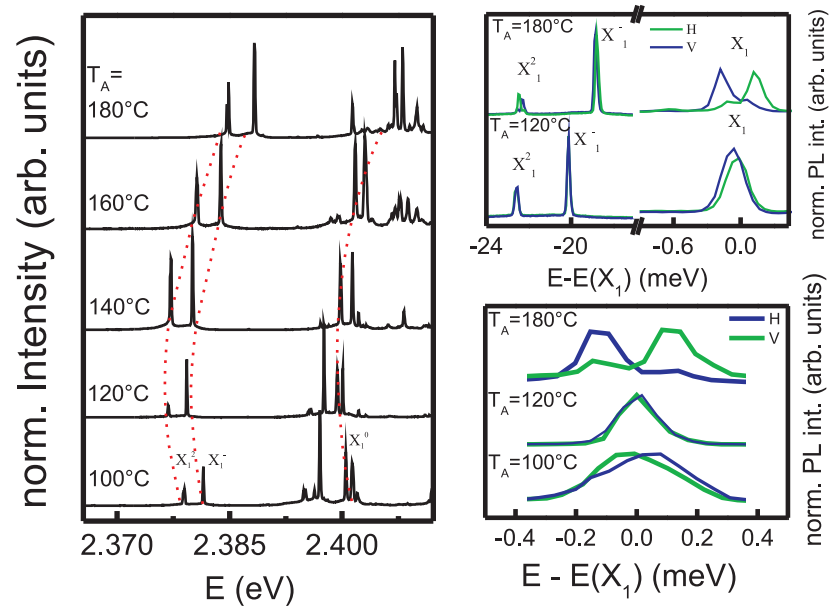


Fig. 6.2: PL spectra recorded from a 150 nm mesa for annealing at temperatures between $T_A = 100$ - 180 °C, for 30 s. The shift of an exciton, biexciton and trion emission is shown by the red dotted lines. (b) A zoom of the spectra corresponding to $T_A = 120$ °C and $T_A = 180$ °C, for the H and V polarization of the emission spectra. The reversal of FSS is demonstrated in (c).

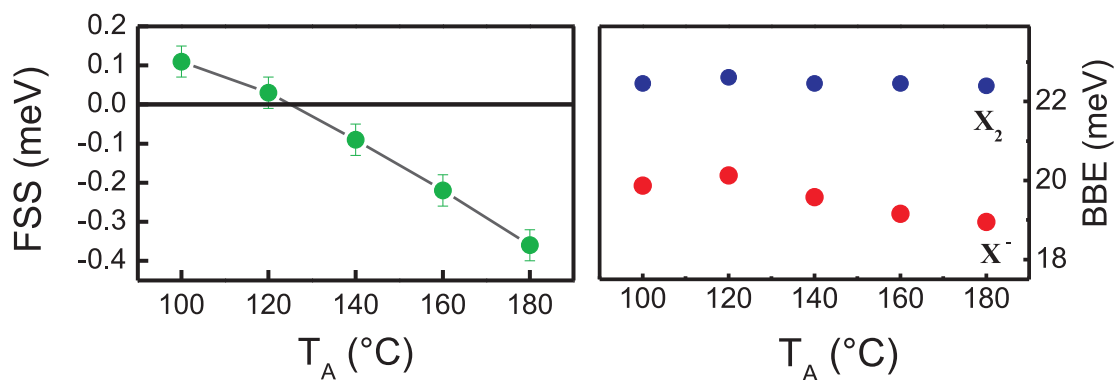


Fig. 6.3: Variation of (a) FSS and (b) trion (blue) and biexciton (red) BE with T_A . The BE values have an error bar of 0.05 meV, being limited by the resolution of the set up.

increasing the annealing temperature to 180 °C, it is clearly observed that the FSS has a negative sign. The value of the FSS in this case is -0.4 meV. This reversal of FSS sign establishes the fact that thermal annealing allows changing the elongation axis of single QDs in perpendicular directions, passing through an intermediate isotropic shape. The values of FSS for different annealing temperatures are plotted in Fig. 6.3 (a) which demonstrates the shape-anisotropy inversion phenomenon. In addition, TA leads to an increase in the size of the QD. This, in turn, reduces the EHX interaction, responsible for the FSS. This contributes to explain FSS tending to zero after progressive annealing. However, none of the above effects can explain the reversal of the FSS. The FSS reversal is brought by the enhanced local interdiffusion close to the mesa walls, in presence of the defects. Indeed, these defects might work as transient-states, which enhances the diffusion (see next section). Finally, TA by changing the shape-anisotropy of QDs on small mesas, also the trion and biexciton binding energies (BE) is influenced. Fig. 6.3 (b) shows the variation of trion (blue) and biexciton BEs with T_A . As is well known, TA induces to an enlargement of the QD size, which in turn means that the electron-hole wave functions are less overlapping leading to a reduced binding energy. This is what was indeed measured in the annealing range between 120-180 °C. However, in the first annealing step, 100-120°C, the binding energy is increased, which is a sign of an improved overlap between the electron and the hole wave functions. This further confirms the high symmetry of the QDs obtained at $T_A = 120^\circ\text{C}$.

6.1.2 Strain assisted diffusion

In addition to defect enhanced diffusion, it should also be mentioned, that in QWs [RYU95, LIM00] and more specifically in QDs [THO03], diffusion occurs not isotropically in the x, y and z directions. Since II-VI QDs are elongated either in the [1 1 0] or [1 -1 0] crystallographic directions (see section 2.1.4), such QDs are normally defined to belong to a symmetric group $< D_{2d}$, where D_{2d} refers to the cylindrical symmetry. The competition between the surface and the elastic energy results in the reduced symmetry of the QDs [THO03]. Such competition induces to release the strain mostly in the elastic soft direction than in the elastic hard direction [THO03]. In this way the system lowers its energy when the dot changes its morphology from a cylindrical symmetry to elongated shape. Post-growth TA releases the strain in z-direction in case of QW. However, in case of QDs the release of the strain occurs also in-plane. Precisely, it is expected to have a major relaxation in the elastic hard direction and a minor relaxation in the soft elastic direction. Consequently, one should expect that by a thermal process a spontaneous relaxation of the elastic directions occurs. As a result, during post-growth TA the surface-wall of an elongated QD converges towards a symmetric shape, if no further contributions are considered.

Chapter 7

7.1 Introduction

Magneto-optical properties of self-assembled semiconductor quantum dots are of wide interest in the study of quantum information processing. The basic idea is to be able to manipulate the spin degree of freedom of a three-dimensionally confined exciton. Magneto-optical response is investigated by magneto-photoluminescence and polarization measurements, which in turn give the possibility to get information about the spin-splitting of the exciton-ground state and the spin lifetime of the electrons and holes. Studies of the degree of circular polarization have been carried out for epitaxially self-assembled QDs of 1- and 2-ML of an ensemble of quantum dots, before and after thermal annealing.

7.2 Inversion of polarization

The samples under investigation were grown by molecular beam epitaxy. More details about the growth condition are presented in Appendix C. The evolution of the degree of circular polarization (DCP) of the PL at magnetic fields of up to 6 T was studied. In Fig. 7.1 is shown the evolution of the PL spectra emitted by the 2ML $\text{Zn}_{1-x}\text{Cd}_x\text{Se}$ QDs samples, before and after thermal annealing. Annealing was carried out at a temperature of $T_A = 500$ °C for 10 s, 30 s, and 50 s. A typical red-shift and narrowing of the spectra of the annealed QDs, compared to the as-grown (un-annealed) QDs, is observed. Spectral narrowing due to TA is well known and has been observed also for QDs realized in other material systems (see discussion in chapter 5). The phenomenon is associated to a TA-induced enhancement of the QDs homogeneity. A close inspection of the PL spectra corresponding to samples annealed, for $t_A = 30$ s and $t_A = 50$ s, also reveals an asymmetry in the spectral shape. This behavior indicates to the presence of a bimodal QD when annealing is performed for long duration.

To probe the annealing-induced evolution of the magneto-optical properties of the QD ensembles, magneto-photoluminescence measurements were carried out in a liquid He bath-cryostat at a temperature of 2K. Magnetic fields were applied parallel to the

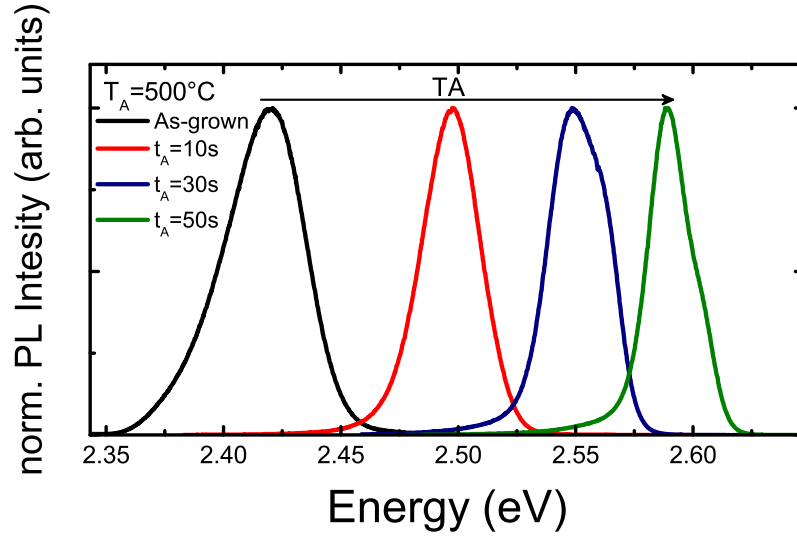


Fig. 7.1: PL spectra recorded from an ensemble of self-assemble quantum dots, before and after 10 s and 30 s of thermal annealing executed at the temperature of $T_A = 500$ °C.

growth direction (Faraday geometry). The PL was excited with the 405 nm line of a solid state continuous-wave laser, as described in chapter 3.1.3. In order to investigate the circular polarization of the QD luminescence, a 50 kHz photoelastic modulator operating as a $\lambda/4$ -plate, in combination with a linear polarizer, was placed in front of the monochromator. For the magnetic field dependent polarization measurements, we evaluated the degree of circular polarization, $DCP = (I^- - I^+) / (I^- + I^+)$, where I^+ (I^-) represents the intensity of the σ^+ (σ^-) polarized QD emission, recorded at the peak maximum. These measurements were performed for two type of samples, the 1ML and the 2ML QDs, prior to and after TA.

The B-field dependence of the DCP of both the as-grown quantum dots and the thermally annealed samples ($T_A = 500$ °C, $t_A = 30$ s) are shown in Fig. 7.2. While for the as-grown QDs (dark-squares), the DCP undergoes a reversal from positive to negative sign beyond a magnetic field strength of $B = 4$ T, it is observed that the DCP corresponding to the annealed QDs (grey-square) exhibits a negative magnetic dispersion in the entire range of $B = 0$ -5 T. While the DCP for the as-grown QDs changes from 1.8% at $B = 4$ T to -3.5% at $B = 8$ T, that for the annealed QDs is -5.0% over the entire range of the B-field.

From high resolution transmission electron microscope (HRTEM) (see Fig. 7.2 b and Fig. 7.2 c) images it is evident that the QD-layer broadens out in the growth direction (z-axis). Regions of bright contrast represent high Cd-content while those

with darkest contrast are highest in Zn-content. The lateral dimensions of the QDs do not change significantly due to TA. As indicated by the white arrow, the typical diameter of the QDs prior-to and after TA is ~ 20 nm. However, the composition and size of the QDs along the z-axis changes significantly. This was observed by recording the variation of the lattice parameter along the growth direction from high resolution off axis images taken after tilting the sample by 10° around the z axis from the [110] zone axis. Hereby, the QD extensions along the direction of growth was estimated to be $L_z = 2$ nm for the as-grown QDs and 6-8 nm for the annealed QDs.

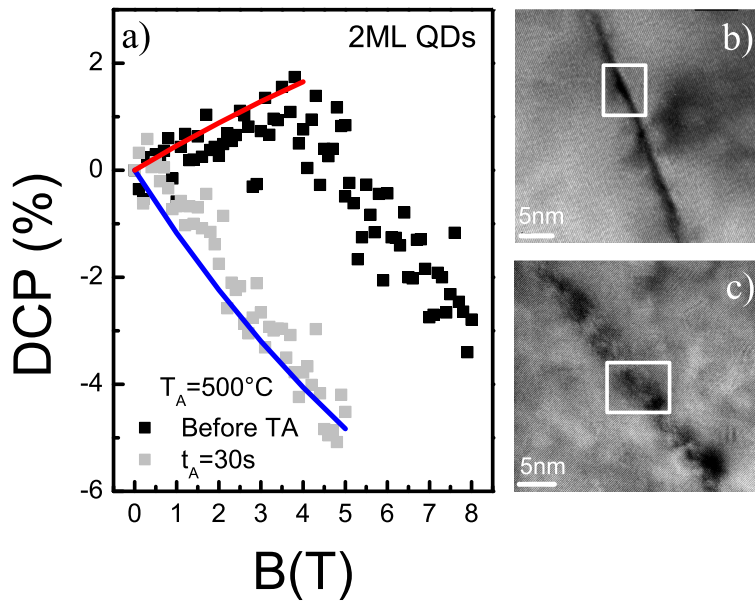


Fig. 7.2: Squares represent the DCP of 2ML $\text{Zn}_{1-x}\text{Cd}_x\text{Se}$ QD luminescence recorded at the peak maximum. Solid curves are corresponding to the fitting with Mackowski model. (b) HREM pictures taken prior to and (c) after thermal annealing for 30 s at $T_A = 500^\circ\text{C}$

Similarly, the DCP for the 1ML $\text{Cd}_x\text{Zn}_{1-x}\text{Se}$ QD-sample was investigated (see Fig. 7.3). In contrast to the 2ML QDs, the as-grown 1ML QDs sample (dark-squares) shows a constant positive DCP ($= 4\%$) for all magnetic fields $B = 0-5\text{T}$. However, when the sample is annealed at $T_A = 500^\circ\text{C}$ for $t_A = 20\text{s}$ (grey-squares) the DCP changes sign ($\text{DCP} = -1.5\%$). In the same way, for the thermally annealed sample, $T_A = 500^\circ\text{C}$ for $t_A = 30\text{s}$ (light gray-square), the DCP changes sign and shows a larger polarization ($\text{DCP} = -9\%$).

From the DCP measurements versus the magnetic field strength, it is possible to

extract the Landé g -factor and the spin relaxation time, τ_s . These two parameters can be extracted following the well known Mackowski model [MAC03]. In the present work the experiments were done by using a linearly polarized source, which implies an equal generation rate for up- and down-spins. Therefore, accordingly to S. Mackowski et al. [MAC03] the equation for the degree of circular polarization can be written as:

$$DCP = \frac{1 - e^{\frac{\Delta E}{kT}}}{1 + (\frac{t_s}{t_r} + 1)e^{\frac{\Delta E}{kT}}}, \quad (7.1)$$

where ΔE is the Zeeman splitting of the exciton ground state, τ_r is exciton relaxation time and τ_s is the spin relaxation time. For simplicity of notation, the ratio τ_s/τ_r will henceforth be denoted as τ . It is worth noting that eq. 7.1 needs to be modified when the changes of sign for the DCP is considered. Precisely, the right side of the eq. 7.1 and the ΔE must change sign.

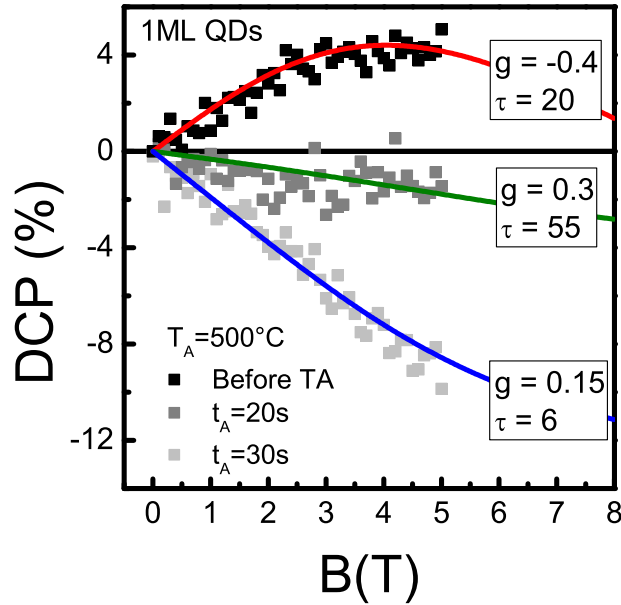


Fig. 7.3: Squares represent the experimental data for the gradual variation in the DCP of 1ML QD-luminescence for different annealing times. Solid curves are the corresponding theoretical fitting.

Then, by using the above equation, the experimental data were fitted for both the 2ML and 1ML QDs samples as shown in Fig. 7.2 and Fig. 7.3, respectively. For the 2ML QDs sample, the experimental data of the as-grown sample shows a non linear behavior. Up to $B = 4$ T the DCP is positive and changes sign for $B = 4-8$ T. This

unusual behavior of the DCP indicates that the g-factor is not constant over the entire field range. Such behavior can be attributed to a mixing of the excitonic states induced by the magnetic field [TRA95], which is reflected in an anomalous Zeeman effect. By fixing $\tau = 15$ and the g-factor $g = -0.06$ (Zeeman splitting $\Delta = -0.014$ meV) the DCP could be fitted for the as-grown QDs sample up to the magnetic field $B = 4$ T. Since the exciton relaxation time measured at $B = 0$ is $\tau_r = 330$ ps, the spin relaxation time becomes $\tau_s = 4.9$ ns, which is in agreement with the value found from Mackowski et al. [MAC03, MAC05].

For the annealed sample ($T_A = 500$ °C and $t_A = 30$ s), the fitting leads to $\tau = 8$ and $g = 0.09$, which means the Zeeman splitting $\Delta E = 0.03$ meV. In this case, the exciton relaxation time at $B = 0$ is $\tau_r = 71$ ps, which leads to $\tau_s = 0.57$ ns. The enhancement of the spin scattering efficiency upon annealing is attributed to an increased mixing between different spin states in larger CdSe quantum dots.

The same calculation was repeated for the 1ML QDs sample. For the as-grown sample, the fitting leads to $\tau = 20$ and $g = -0.4$, which correspond to $\Delta E = -0.1$ meV at $B = 5$ T. For this sample, the exciton relaxation time at $B = 0$ is $\tau_r = 190$ ps, and therefore the spin relaxation time turn out to be $\tau_s = 3.8$ ns. For the annealed sample, $T_A = 500$ °C for $t_A = 20$ s, the fitting leads to $\tau = 55$ and $g = 0.33$, which correspond to $\Delta E = 0.08$ meV at $B = 5$ T. The measured exciton relaxation time at $B = 0$ is $\tau_r = 180$ ps. Therefore, the extracted spin relaxation time is $\tau_s = 9.9$ ns. Finally, for the 1ML QDs annealed sample, $T_A = 500$ °C for $t_A = 30$ s, the fitting leads to $\tau = 6$ and $g = 0.15$, which correspond to $\Delta E = 0.04$ meV at $B = 5$ T. In this last case, the measured exciton relaxation time at $B = 0$ is $\tau_r = 170$ ps, that leads to $\tau_s = 1.0$ ns. For clarity, all the above calculated parameters are tabulated in Table 7.1.

Tab. 7.1: Values of the g-factor, exciton and spin relaxation time and Zeeman splitting extracted from the 2ML and 1ML QDs samples before and after TA.

—	B (T)	g	τ_r (ps)	τ_s (ns)	ΔE (meV)
2ML QDs (as-grown)	0-4	-0.06	330	4.9	-0.014
2ML QDs ($t_A = 30$ s)	0-5	0.09	71	0.57	0.03
1ML QDs (as-grown)	0-5	-0.4	190	3.8	-0.1
1ML QDs ($t_A = 20$ s)	0-5	0.33	180	9.9	0.08
1ML QDs ($t_A = 30$ s)	0-5	0.15	170	1.0	0.04

It should be pointed out that all the calculated Zeeman splittings are much smaller than one would expect for CdSe/ZnSe QDs, which normally show g-factors in the order of $g = 1$ [KUN98, MAC05]. In order to understand the reason of such small g-factor, single quantum dot spectroscopy for the as-grown and annealed samples were carried out in presence of an external magnetic field. In Fig. 7.4 (a) and (b) the PL spectra recorded at $B = 6$ T are shown, for the as-grown and annealed samples ($T_A = 500$ °C

and $t_A = 10$ s), respectively. The energy difference between $E(\sigma^+)$ and $E(\sigma^-)$ reflects the Zeeman splitting. For the as-grown sample the measured g -factor is $g_X = 1.1$ and for the thermally annealed samples are $g_X = 1.7$ (QD1) and $g_X = 3$ (QD2). It is worth noting that the g -factors determined from the single QDs is bigger than to the value of QD-ensembles determine by using eq. 7.1 and shown in Table 7.1.

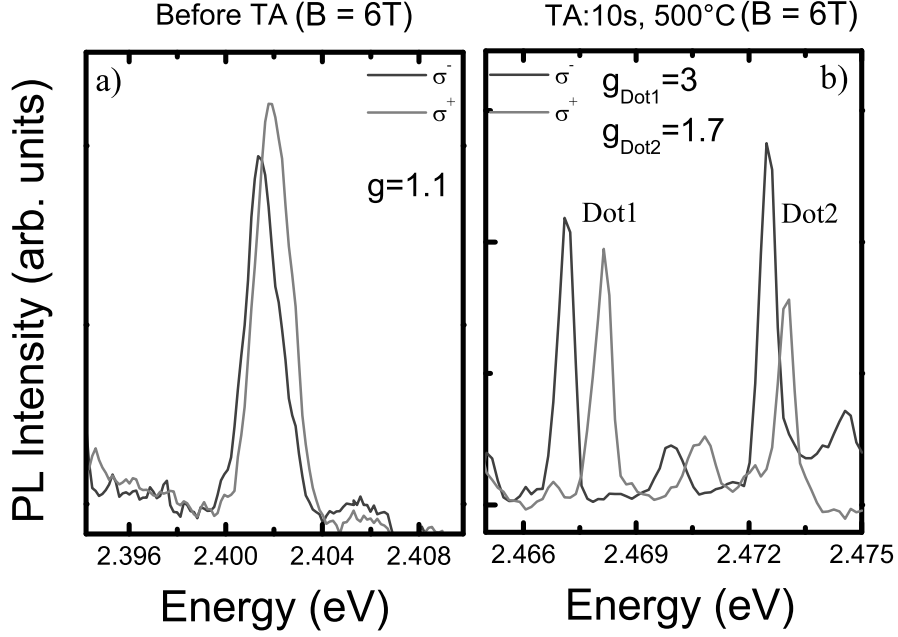


Fig. 7.4: (a) Zeeman splitting of a single QDs before TA and (b) after TA at $T_A = 500^\circ\text{C}$ for $t_A = 10$ s. The magnetic field strength is $B = 6$ T.

The SQD magneto spectroscopic data presented here (see Fig. 7.4) reveals that the g -factors of selenide-based QDs are much larger than those calculated from DCP measurements, based on the Mackowski model. The fundamental difference is in the fact that eq. 1 assumes that the g -factor is due to one type of carriers, namely the holes in this case. This can be understood considering the existence of an excess density of electrons. Indeed, it is well known that II-selenides exhibit an unintentional n -type doping, often attributed to native defects [WAL02]. Electrons from certain donor-type native defects [YOA85], as well as from the n -type GaAs substrate, might relax into the QDs making the QDs negatively charged. With this assumption, the extracted g -factors from the DCP-measurements correspond to the minority carriers and not to the excitons, as one would expect.

For the theoretical description we have considered the QDs to be embedded in a QW-like structure. The spatial confinement of holes and electrons, in the theoretical simulation is defined by an in-plane potential, $V_{x,y} = 1/2 m_{x,y}\omega_0^2 (x^2+y^2)$, where $m_{x,y}$

is the carrier in-plane effective mass and $\omega_0^2 = \hbar/(m_0 R^2)$ is the parabolic confinement strength in terms of the effective lateral extension of the QD, R [DES04]. For the longitudinal direction, we assume a hard wall QW, with height L_z . The unperturbed Hamiltonian has the well-known Fock-Darwin solution [DES04]. The kinetic energy for the valence (conduction) band is treated by the 4×4 (2×2) Luttinger coupled (parabolic uncoupled) Hamiltonian.

By the use of a multiband calculation it can be shown that the spin splitting of the ground states of the electrons and heavy-holes depends on the QD-parameters [EFR98, KiS01, KOT01, KUN98, MAC05]. The Cd-content dependence has been introduced from the reported values of the band parameters of $\text{Zn}_{1-x}\text{Cd}_x\text{Se}$ [LAN96, ZAR05]. Due to a lack of parameters, a linear interpolation between the corresponding values of ZnSe and CdSe has been assumed for the alloy composition. In Fig. 7.5 (a) and (b), the corresponding Zeeman splittings for the first conduction and the topmost valence band levels are shown for various Cd-content values. The conduction band is only slightly affected by the alloy composition. It is the valence band that responds in a much stronger way. The Zeeman splitting of the valence band ground state changes slope with the magnetic field, and its sign beyond a certain Cd-concentration. This is caused by the coupling between the light- and the heavy-hole states. Such an effect leads to an inversion in the occupation of the spin-split hole-levels which, in turn, results in a sign-reversal of the DCP. More details about the theory are given in Ref. [MAR08].

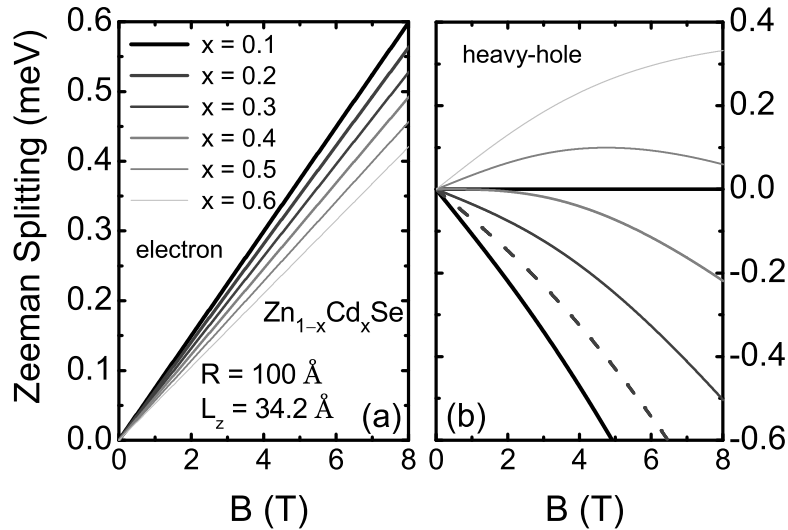


Fig. 7.5: Calculated Zeeman splitting for the a) conduction- and b) valence-band ground states of the QD as a function of the magnetic field and for different Cd-contents, x .

Chapter 8

8.1 Paramagnetic response of TA nonmagnetic SQD

A characteristic signature of nonmagnetic semiconductors (NMSs) is the absence of a permanent magnetic moment. Typically, the zero-dimensional ground state of electrons and holes in NMS QDs have zero angular momentum and exhibit therefore a diamagnetic response of spin-split states to an external magnetic field [JAC98, KRO04, WAL98, CIN99]. To realize magnetic quantum dots (MQDs), usually paramagnetic ions are incorporated, e.g. Mn^{2+} [AWS00, AND50, BAC02, HEN07]. In this chapter it is demonstrated that pronounced paramagnetic behavior can also be observed in the spectra of single nonmagnetic CdSe quantum dots, after post-growth RTA and without the incorporation of extra manganese spins. Such behavior is associated with quantum-confinement induced inversion of heavy (hh) and light hole (lh) states when the Cd-content, x , within the QD is decreased.

8.2 Sample preparation and experimental set-up

The sample-structure investigated in this chapter is described in Appendix E. Post-growth TA was performed in N_2 environment at a temperature of $T_A = 500$ °C for a duration of 10 s. The measurements were carried out in a LHe bath-cryostat at a temperature of 2K (the set-up is described in section 3.4). Magnetic fields of up to 7T were applied parallel to the growth direction (Faraday configuration). The QDs were excited with a 405 nm line of a solid state continuous wave laser. The QD-PL were dispersed by a monochromator and recorded with a LN_2 cooled CCD camera. In order to select the photoluminescence from a SQD, small mesas with a diameter of about 100 nm, carrying only a low number of QDs, were fabricated by EBL and wet-chemical etching.

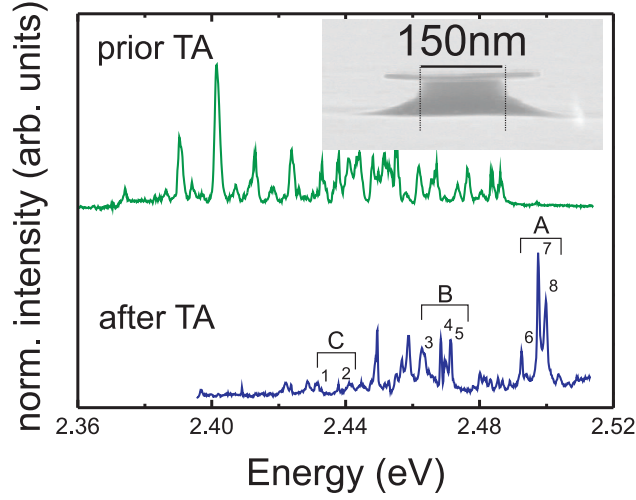


Fig. 8.1: PL spectra recorded from a 150 nm mesa prior to (green) and after (blue) thermal annealing (TA). TA leads to a blue shift of the spectrum due to Cd-Zn intermixing between the QDs and the surrounding matrix. The inset shows a SEM image of the mesa before mask removal.

8.3 Experimental observation

The investigation of the magnetic properties of QDs were executed by studying a single layer of CdZnSe QDs embedded in a ZnSe matrix by optical spectroscopy. To observe single exciton lines, small mesas (≈ 100 nm), containing a small number of self-assembled CdZnSe QDs, were fabricated. In the inset of Fig. 8.1, an SEM image of a mesa, prior to mask removal, is shown. A typical PL spectrum, recorded from a 150 nm mesa is presented in the upper part of the same figure. On the low energy side, the spectrum shows several narrow emission lines associated with SQD excitons. The bottom spectrum corresponds to a RTA-treated sample with annealing parameters $T_A = 500$ °C and $t_A = 10$ s. Typically, the PL spectrum of RTA QDs is blue-shifted compared to that of the as-grown sample. The energy-shift is caused by interdiffusion of the Cd and Zn atoms between the ZnSe-barrier and the CdSe QD-layer [MAR06]. The exciton lines in the annealed spectrum are numbered and distinguished into three regions *A*, *B* and *C*, in order to associate them to data discussed later on. To study the changes of the magnetic properties of SQD after TA, eight QDs lines were carefully studied in magnetic fields up to 7T.

On the left panel of Fig. 8.2 the PL-spectra of a thermally annealed QD (line 4, Fig. 8.1) is shown. Here, spectra corresponding to two circular polarized detection

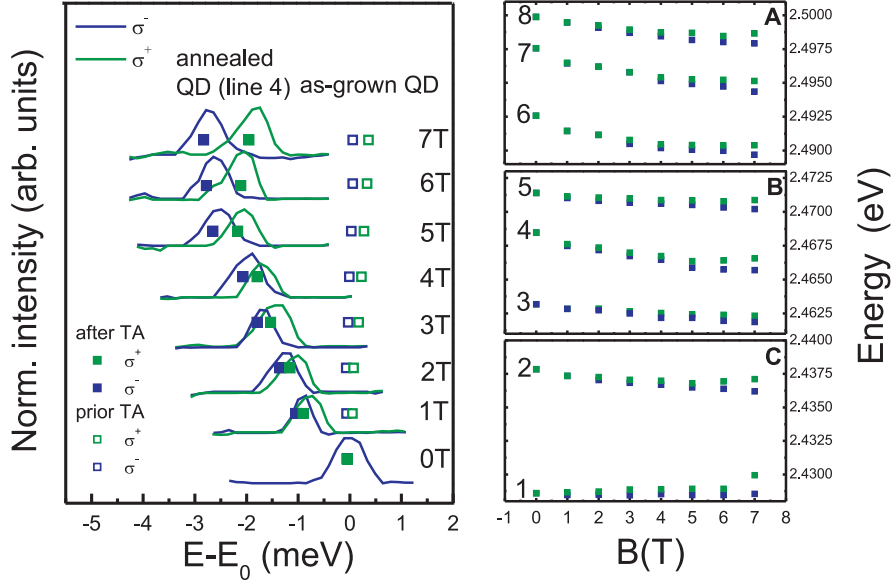


Fig. 8.2: (Left part) PL spectra of a thermally annealed QD (line 4). The peak energies are red-shifted with increasing magnetic field strength, \mathbf{B} . Typically, as-grown QDs show a small energy blue shift of the circularly polarized components (σ^\pm), as an effect of diamagnetism. (right side) Zeeman splitting of the eight QD lines, after TA, indicated in Fig. 8.1. By increasing the magnetic field \mathbf{B} the single exciton lines split into a σ^+ (green) and σ^- (blue) circularly polarized component, with the center of gravity, ΔE , shifted to lower energies.

(σ^\pm) are shown for different magnetic field strengths. For clarity, the peak positions, (full squares) of the spectra, are also indicated and the corresponding peak positions (empty squares) of the as-grown QD is also given as reference. After TA, already at 1T, both σ^+ and σ^- emissions are pronouncedly red-shifted. Between 1T and 5T, the shift increases and saturates between 5T and 6T. In addition, it should be pointed out that for the same dot the Zeeman splitting is larger compared to the one measured prior TA. Indeed, the measured g-factor is roughly $g \approx 1$ prior TA and $g \approx 2$ after TA. A weak diamagnetic blue-shift of the Zeeman components for the reference as-grown QD is determined [ERD06, SCH02] to be 0.3 meV at 7T. On the contrary, the Zeeman splitting of all the annealed QDs, designated by numbers 1 to 8 in Fig. 8.1, shift towards low energies when \mathbf{B} is increased. The trend, for all 8-lines is shown in Fig. 8.2. All annealed QDs, except QD1 in panel C, are red-shifted with increasing

magnetic field, henceforth referred to as paramagnetic shift (PS). The largest shift measured after TA is -2.8 meV (line 7), whose absolute value is much larger compared to the positive shift of the unannealed QD. For a better comparison, the energy-shift for each QD investigated was calculated and presented in Fig. 8.3. By using eq. 2.15 and eq. 2.16 it is possible to determine the diamagnetic shift for all 8-QDs, above measured. Therefore, the diamagnetic shift is given by:

$$\Delta E(B) = \frac{E(B)^{\sigma^+} + E(B)^{\sigma^-}}{2} - E(0) = \gamma B^2 \quad (8.1)$$

where γ is the diamagnetic coefficient and $E(B)^{\sigma^+}$ and $E(B)^{\sigma^-}$, the energy components of σ^+ and σ^- , respectively. As expected, the energy-peak shifts towards high energy when the unannealed QD (empty circle) is considered. On the other hand, from the annealed sample, all the other QD-lines (except QD1) show pronounced red-shifts.

8.4 Theoretical calculation

In order to explain the observed red shifted energy of the PL spectra, of both the circularly polarized emission light, σ^\pm , in presence of an external magnetic field, \mathbf{B} , a comparison between Fock-Darwin model and multi-band calculation was developed. For the purpose of understanding the magnetic dispersion of the annealed QDs, the electronic structure of the QDs has been analyzed using the Fock-Darwin Hamiltonian for the conduction band states and a multiband Luttinger Hamiltonian for the valence band states. A single $\text{Cd}_x\text{Zn}_{1-x}\text{Se}$ QD has been modeled by a cylindrical spatial confinement within a region of radius R and height L_z . The band parameters for the ternary compound have been assumed to be a linear function of the Cd-content. The vertical confinement (z -axis), $V(z)$, of the QD has been assumed to be square-well like, while the in-plane confinement (x - y plane), $V(\rho)$, radially symmetrical, with $\rho^2 = x^2 + y^2$. The radially symmetric in-plane potential emulates a smooth (radially symmetric) transition of the Cd-content from the centre (high Cd content) to the periphery of the QD. With these assumptions, the axial (ρ) and vertical (z) coordinates inside this cylindrically shaped QD can be treated as separable variables, without any loss of generality, even in the presence of magnetic field applied along the vertical direction.

Conduction band: Fock-Darwin model

For the assumed cylindrical confinement, the conduction band Hamiltonian can be solved within the Fock-Darwin formalism. The electron of effective mass $m^* \cdot m_0$ is assumed to be confined within an in-plane parabolic potential $V(\rho) = 1/2m_0/m^*\omega_0^2\rho^2$, where $\omega_0 = \hbar / m_0 R^2$ is the axial parabolic frequency. In the absence of external field,

the localization of an electron can be described by the cylindrical Hamiltonian,

$$\mathcal{H}_D^{(0)} = \frac{1}{m^*} \left\{ \frac{\hbar^2}{2m_0} \hat{\mathbf{k}}^2 + \frac{1}{2} m_0 \omega_0^2 \rho^2 \right\} + V(z), \quad (8.2)$$

This Hamiltonian can be re-written in terms of creation and annihilation operators, a_{\pm}^{\dagger} and a_{\pm} , using the harmonic expressions:

$$\hat{k}_{\pm} = \frac{i}{R} (a_{\pm}^{\dagger} - a_{\mp}). \quad (8.3)$$

Equation 8.2 then reads as:

$$\mathcal{H}_D^{(0)} = \mathcal{H}_{xy} + \frac{\hbar^2}{2m^*m_0} \hat{k}_z^2 + V(z), \quad (8.4)$$

where

$$\mathcal{H}_{xy} = \frac{\hbar}{m^*} \omega_0 (\hat{N}_+ + \hat{N}_- + 1), \quad (8.5)$$

This is the bi-dimensional harmonic oscillator problem with number operators, $\hat{N}_{\pm} =$

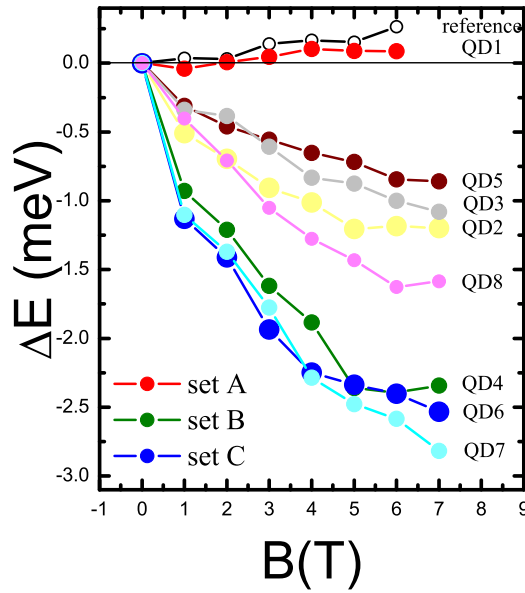


Fig. 8.3: As-grown QDs (empty circle) and one of the annealed QDs (line 1) show a typical diamagnetic shift. In contrast, a paramagnetic shift is observed for all the other annealed QDs.

$a_{\pm}^{\dagger} a_{\pm}$. The eigenstates of Eqn. 8.4 can be labeled as $|n_+, n_-\rangle$, with $n_+, n_- = 0, 1, 2, \dots$. The eigenstates obey the eigenvalue relations $\hat{N}_{\pm} |n_+, n_-\rangle = n_{\pm} |n_+, n_-\rangle$.

From eq. 8.5 it is seen that in absence of an external magnetic field, the states $|n_+, n_-\rangle$, with $n_+ + n_- = \text{const}$, remain energetically degenerate. The degeneracy of the states can be broken when a magnetic field, $\mathbf{B} = B\hat{z}$, is applied parallel to the symmetry-axis of the QD. This field leads to the quantization of the angular momentum, $L_z = n_+ - n_-$. Consequently, an effective potential is added to the axial quantization, $V_B = m_0/m^* \omega_c^2 \rho^2 / 8$, where $\omega_c = eB/m_0c$ is the cyclotron frequency.

The new Hamiltonian for the in-plane motion, in presence of \mathbf{B} , can now be written as:

$$\mathcal{H}_{FD} = \frac{1}{m^*} \left[\hbar\omega_+ \left(\hat{N}_+ + \frac{1}{2} \right) + \hbar\omega_- \left(\hat{N}_- + \frac{1}{2} \right) \right] + \frac{g_0\mu_B}{2} B\sigma_z, \quad (8.6)$$

where, $\omega_{\pm} = \Omega \pm \omega_c/2$ and $\Omega = \sqrt{\omega_0^2 + \omega_c^2/4}$, $\mu_B = e\hbar/2m_0c$ is the Bohr magneton, g is the electron Landé factor and σ_z is the z -component of the Pauli matrix. The corresponding eigenvalues of the Hamiltonian (eq. 8.6) are

$$E_{n_+, n_-, \sigma_z} = \frac{1}{m^*} \left[\hbar\Omega (n_+ + n_- + 1) + \frac{1}{2} \hbar\omega_c (n_+ - n_-) \right] + g_0\mu_B B \frac{\sigma_z}{2}. \quad (8.7)$$

Valence band description: Luttinger model

The description of electronic states in the valence band are not captured adequately by the Fock Darwin formalism and one needs to go beyond the parabolic band approximation. In the majority of the situations describing wide-gap semiconductor states in nanostructures, such as QDs, the multi-band Luttinger Hamiltonian model is a fairly good approximation. The eigensolutions of (eq. 8.6) can be found by using the commutation and anti-commutation relations between momentum operator components, in the form of

$$\{\hat{k}_+, \hat{k}_-\} = \left(\hat{N}_+ + \frac{1}{2} \right) c_+^2 + \left(\hat{N}_- + \frac{1}{2} \right) c_-^2 - c_+c_- \left(a_+^\dagger a_-^\dagger + a_+ a_- \right), \quad (8.8)$$

$$[\hat{k}_+, \hat{k}_-] = -c_+^2 + c_-^2. \quad (8.9)$$

The Luttinger Hamiltonian then takes the matrix form

$$\mathcal{H}_L = \begin{bmatrix} D_{hh}^{(+)} & A_- & 0 & B \\ & D_{lh}^{(+)} & B & 0 \\ & & D_{hh}^{(-)} & A_+ \\ & & & D_{lh}^{(-)} \end{bmatrix}, \quad (8.10)$$

where

$$D_{hh}^{(\pm)} = - \left(\frac{\tilde{\gamma}_1 + \tilde{\gamma}_2}{2} \right) \{\hat{k}_+, \hat{k}_-\} - \left(\frac{\tilde{\gamma}_1 - 2\tilde{\gamma}_2}{2} \right) \hat{k}_z^2 \pm \frac{3}{4} \left(\bar{\kappa} + \frac{9}{4}\bar{q} \right) [\hat{k}_+, \hat{k}_-] \quad (8.11)$$

$$D_{lh}^{(\pm)} = - \left(\frac{\tilde{\gamma}_1 - \tilde{\gamma}_2}{2} \right) \{\hat{k}_+, \hat{k}_-\} - \left(\frac{\tilde{\gamma}_1 + 2\tilde{\gamma}_2}{2} \right) \hat{k}_z^2 \pm \frac{1}{4} \left(\bar{\kappa} + \frac{1}{4}\bar{q} \right) [\hat{k}_+, \hat{k}_-] \quad (8.12)$$

represent the diagonal terms. The off-diagonal terms are defined by,

$$A_{\pm} = \mp\sqrt{3}\bar{\gamma}_3\hat{k}_{\pm}\hat{k}_z, \quad (8.13)$$

$$B = -\frac{\sqrt{3}}{2}\bar{\gamma}\hat{k}_{-}^2, \quad (8.14)$$

with:

$$\bar{\gamma}_i = \frac{\hbar^2}{m_0}\gamma_i \quad (i = 1, 2, 3) \quad , \quad \bar{\kappa} = \frac{\hbar^2}{m_0}\kappa \quad , \quad \bar{q} = \frac{\hbar^2}{m_0}q \quad , \quad \bar{\gamma} = \frac{\bar{\gamma}_2 + \bar{\gamma}_3}{2}. \quad (8.15)$$

As one may note, the opposite spin-states hh^{\pm} and lh^{\pm} in the first subband, corresponding to the quantization in the z -direction, are coupled through the terms B^2 (A_{\pm}), proportional to the quadratic (linear) operators. They induce hh - lh hybridization between states that have an angular momentum difference $\Delta m = \pm 2$ ($\Delta m = \pm 1$). This effect raises or lowers the Fock-Darwin quantum numbers n_{\pm} between hybridized states by a factor 2 (1). The results of last calculation, for the valence bands, are shown

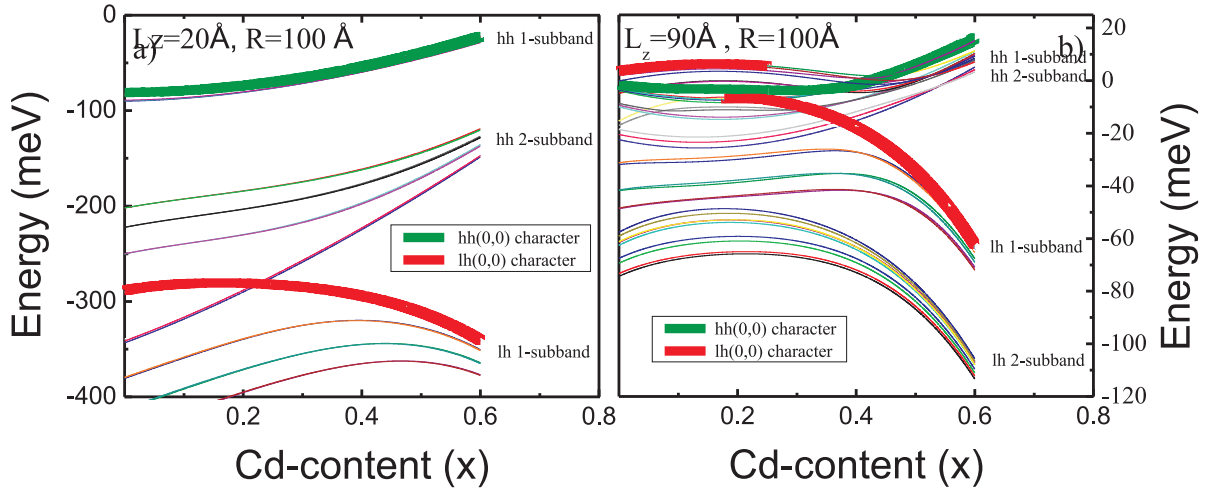


Fig. 8.4: (a) Calculated valence bands of a quantum dot, with $L_z = 2 \text{ nm}$ and $R = 10 \text{ nm}$, versus Cd-content, x , where strain was taken in account. The light and heavy hole states are energetically separated due to both strain and confinement. (b) Valence bands of an annealed quantum dot, with $L_z = 9 \text{ nm}$ and $R = 10 \text{ nm}$, versus the Cd-content, x , where a mixture between the heavy and light states occurs. The hybridization is now strongly x -dependent.

in Figs. 8.4 (a) and (b). Fig. 8.4 (a) shows, for an as-grown QD, the band energies for the first and the second heavy subbands (hh 1- and hh 2-subband). The first light hole subband (lh 1-subband) are shown too. The same plot is shown for an annealed QD in Fig. 8.4 (b). A comparison of the two figures reveals a striking feature. Annealing

induced reduction of Cd content of a single QD leads to an inversion of the ground state from a hh to a hybrid state, with contributions from the lh state.

With the aid of the calculations performed here, based on a combination of FD formalism for the conduction band states and a multi-band Luttinger formalism for the valence band states, it is possible to explain the observed magneto-optical dispersion of the annealed SQDs (see Fig. 8.3).

For an as-grown SQD (i.e. prior to RTA), the ground state is purely hh in character. The exciton states, defined by an electron and a heavy hole, are well described by the simple parabolic band model. On the contrary, after TA, the previously well defined QD-potential is expected to undergo a pronounced change both in size and composition. The QD is now enlarged and the Cd-content per unit volume is reduced. The result of the calculations presented before indicates that due to TA the QDs were modified in a way such that their ground valence band state assumes a hybrid hh-lh character. This hybridization leads to coupling of the orbital angular momenta of the involved states and imparts a non-zero m -value for the hole-ground state [IVC97, PER96, BRA97a].

The above description can be easily understood by referring to Figs. 8.4 (a) and (b), which represent the cases prior to and after thermal annealing, respectively. Due to the selection rule, the bands that mainly contribute are the hh 1-subband and the lh 1-subband, commonly known as the heavy and light hole states. These bands are emphasized by green and red thick lines. Prior to TA, when the Cd-content is high, for instance $x = 0.6$, the energy difference between the two bands is ≈ 300 meV, which is large enough to avoid a contribution from the light hole states to the valence band ground state. If the Cd-content is reduced, the energy difference, $lh(0,0)$ - $hh(0,0)$, is also reduced. However, this variation is not so relevant for a small and strongly confined QD. Indeed the hh- and lh-bands still do not influence each other when very low Cd-content is considered.

The influence of the change in Cd content becomes prominent when the size of the QD is changed such that the exciton confinement is reduced (Fig. 8.4 (b)). In Fig. 8.4 (b), $L_z = 9$ nm, as opposed to 2 nm in case of Fig. 8.4 (a). This change in L_z (vertical confinement), for a constant in-plane radius ($R = 10$ nm) clearly demonstrates a strong variation of the valence band and a crossover from a hh to a lh valence band ground state for Cd content ≤ 0.3 .

The calculated exciton energy shifts in an externally applied magnetic field (in Faraday geometry) are shown in Fig. 8.5 for both as-grown and annealed QDs, for several QDs size. When one considers a pure hh-ground state, a diamagnetic energy shift occurs, as indicated by the red line and the dotted lines grouped by a circle (see Fig. 8.5 (a)). In this case the height of the QD is $L_z = 2$ nm and the radius $R = 10$ nm, while the Cd-content is 15%. Keeping the Cd:Zn ratio fixed when L_z is increased beyond 2 nm, the energy shift clearly shows a paramagnetic character (i.e. a red shift). This paramagnetic shift (PS) increases with increasing L_z , up to $L_z = 6$ nm, beyond which it starts to fall again. This is illustrated by the case $L_z = 9$ nm. On the other

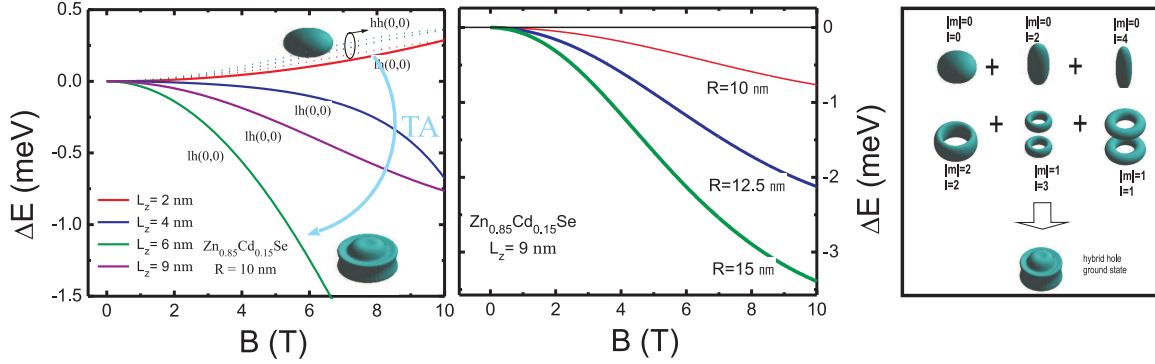


Fig. 8.5: a) Ground state QD exciton formed by hh shows always the diamagnetic shift. In contrast, when the lh is the predominant components in the ground state, a red-energy shift is observed. By variation of QD shape, due to TA, it is found that the lh becomes the ground hole state. For a fixed $R = 10$ nm. The different holes states are visualized for clarity by surfaces of constant wave amplitude. b) PS obtained by changing now the R and let fix $L_z = 9$ nm. c) Superposition of several density of WFs leads to a hybrid WF with light hole character.

hand, an increase in the in-plane radius R , for a fixed value of L_z and alloy composition, causes the PS to decrease further (Fig. 8.5 (b)). Indeed, for $R = 15$ nm, a shift of -2.62 meV was recorded.

Fig. 8.5 (a) also shows the valence ground state wave function (WF) prior to (top inset) and after TA. The disc-shaped density of the unannealed sample corresponds to a purely hh hole ground state. On the other hand, the density distribution is strongly modified after TA. The shown distribution is a hybrid of individual WFs, which are shown pictorially in Fig. 8.5 (c), along with the respective values of the magnetic quantum numbers (m). It is due to this hybridization, that the valence band ground state assumes a predominantly light hole character and a non-zero value of m . This leads to the observed negative energy shift. The negative energy shift was observed whenever the lh-state contributes largely to the exciton ground state, which was demonstrated by varying the parameter space for several different QD-compositions and -shapes.

Appendix A

The $\vec{k} \cdot \vec{p}$ in the perturbation approach

One of the method used for the calculation of the conduction and valence band states is accomplished by the $\vec{k} \cdot \vec{p}$ theory [DAV98]. The Hamiltonian in the $\vec{k} \cdot \vec{p}$ theory can be written as:

$$\left(H_0 + \frac{\hbar}{m_0} \vec{k} \cdot \vec{p} + \frac{\hbar^2 k^2}{2m_0} + \right) u_{\vec{k}, \vec{r}} = \epsilon(\vec{k}) u_{\vec{k}, \vec{r}}, \quad (8.16)$$

obtained by substituting the Bloch wave function into the Schrödinger equation plus two extra terms, taking into account the perturbation. In order to resolve the above equation, is possible to distinguish between two cases, that are the study of the Hamiltonian in presence or in absence of the spin-orbit interaction. When is considered the case of absence of *spin-orbit interaction*, the solutions of the eq. 8.16 for a direct semiconductor crystal are the eigenvalues $\epsilon_n(0)$ and the corresponding eigenstates $|n\rangle$. So using the perturbation theory¹ the eigenvalues of eq. 8.16 for small \vec{k} are:

$$\epsilon_n(\vec{k}) \approx \epsilon_n(0) + \frac{\hbar^2 k^2}{2m_0} + \frac{\hbar^2}{m_0^2} \sum_{m \neq n} \frac{|\langle u_{0, \vec{r}} | \vec{k} \cdot \vec{p} | u_{n, 0} \rangle|^2}{\epsilon_n(0) - \epsilon_m(0)}. \quad (8.20)$$

¹By the *perturbation theory* a second order correction is added to the Schrödinger solution resolved at Γ point, $H^{(0)}|n\rangle = \epsilon_n^{(0)}|n\rangle$, with $|n\rangle$ the eigen function and $\epsilon_n^{(0)}$ the eigen energy solutions of the non-perturbed Hamiltonian. When the perturbation is introduced, the Hamiltonian is written as $H = H^{(0)} + W$, where W is the perturbation. If the eigenvalues are non-degenerate, the first order energy correction is:

$$\Delta \epsilon_n^{(1)} \approx \langle n | W | n \rangle, \quad (8.17)$$

and no correction in the eigenfunctions are expected. On the contrary, in the second order the perturbation arises from the non-diagonal terms in the matrix element of the perturbation potential. The energy correction become:

$$\Delta \epsilon_n^{(2)} \approx \sum_{m \neq n} \frac{|\langle n | W | m \rangle|^2}{\epsilon_n^{(0)} - \epsilon_m^{(0)}}. \quad (8.18)$$

Consequently, it is possible to write the total energy:

$$\epsilon_n \approx \epsilon_n^{(0)} + \Delta \epsilon_n^{(1)} + \Delta \epsilon_n^{(2)} \quad (8.19)$$

In this last case the perturbation arise from the interaction between different eigenvalues. Whether interaction arise between the states or not is decided by the matrix elements $\langle n | W | m \rangle$ in eq. 8.18.

The above expression can be rewritten more simply as:

$$\epsilon_n(\vec{k}) \approx \epsilon_n(0) + \frac{\hbar^2 k^2}{2m^*}, \quad (8.21)$$

where

$$\frac{1}{m^*} = \frac{1}{m_0} \left[1 + \frac{2}{m_0 k^2} \sum_{m \neq n} \frac{|\langle u_{0,\vec{r}} | \vec{k} \cdot \vec{p} | u_{n,0} \rangle|^2}{\epsilon_n(0) - \epsilon_m(0)} \right]. \quad (8.22)$$

This is the *reciprocal effective mass* of the n^{th} band. Equation 8.22 describes the electron effective mass in a semiconductor crystal. It shows that, due to the coupling between electronics states of different bands an electron in a semiconductor crystal has different mass. From the energy solution is possible to have an idea of the band shape. Taking into account the conduction band at the Γ -valley, the largest contribution comes from the band energetically nearest, that is the top of the valence band. The matrix elements in eq. 8.20 do not vanish because the conduction band is symmetric (*s*-like) and the valence band is asymmetric (*p*-like). The conduction band effective mass is given by:

$$m_c^* \approx \frac{m_0}{1 + \frac{2P^2}{m_0 E_g}}. \quad (8.23)$$

Since the valence band at Γ -point is four-fold degenerate, the $\vec{k} \cdot \vec{p}$ theory alone is not sufficient to resolve it.

Kane Model

The Kane model is a standard approximation that can be used at various level of resolution. The full Kane model describes the valence bands by taking into account the spin-orbit interaction, which is significant when the atomic number increases.

The resolution of the $H_{\vec{k} \cdot \vec{p}}$ in the perturbation approach is a satisfactory method only for small values of \vec{k} near the Γ -point. A better approach is to resolve the Hamiltonian exactly within a restricted basis set. The basis set is that of all eigenfunctions at $\mathbf{k} = 0$, as used in the perturbation theory, above introduced. By neglecting the spin-orbit coupling in the Kane model, the valence bands, and specially the heavy hole states are not well supported for $\mathbf{k} \neq 0$. Consequently, by considering the spin-orbit interaction, the solutions of the Schrödinger equation can be expressed with the Kane model using the following base set $|j, j_z\rangle$:

$$\begin{aligned} |\frac{3}{2}, +\frac{3}{2}\rangle &= | + 1 \uparrow \rangle, \\ |\frac{3}{2}, +\frac{1}{2}\rangle &= \sqrt{\frac{1}{3}} | + 1 \downarrow \rangle - \sqrt{\frac{2}{3}} | 0 \uparrow \rangle, \\ |\frac{3}{2}, -\frac{1}{2}\rangle &= -\sqrt{\frac{1}{3}} | - 1 \uparrow \rangle - \sqrt{\frac{2}{3}} | 0 \downarrow \rangle, \\ |\frac{3}{2}, -\frac{3}{2}\rangle &= | - 1 \downarrow \rangle, \end{aligned}$$

$$|\frac{1}{2}, +\frac{1}{2}\rangle = \sqrt{\frac{2}{3}}|+1 \downarrow\rangle + \sqrt{\frac{1}{3}}|0 \uparrow\rangle,$$

$$|\frac{1}{2}, -\frac{1}{2}\rangle = -\sqrt{\frac{2}{3}}|+1 \uparrow\rangle + \sqrt{\frac{1}{3}}|0 \downarrow\rangle,$$

In this thesis will be not given detailed information regarding this model. More information of how to calculate this base set and to derive the Hamiltonian matrix can be found in the text book of Cordona [CAR96] and J. H. Davies. [DAV98].

The spin-orbit coupling within the Kane model mirrors better the conduction and valence band for $k < 0.5 \text{ nm}^{-1}$, but for larger k the bands approach the previous model. Also the description of the heavy hole is quite unsatisfactory, then the simplest approach is to decouple the band with total angular momenta $j = 3/2$ from $j = 1/2$ when the spin-orbit coupling is large enough. Consequently, it is possible to calculate the heavy- and light-hole-band without affecting the others. In this case the $H_{\vec{k}, \vec{p}}$ can be restricted to $j = 3/2$ and can be solved exactly. This approach is called *Luttinger model* and gives the energies of heavy and light holes as follow:

$$\epsilon(k) = E_v - \frac{\hbar^2}{2m_0} [Ak^2 \pm \sqrt{(Bk^2)^2 + C^2(k_x^2 k_y^2 + k_y^2 k_z^2 + k_z^2 k_x^2)}]. \quad (8.24)$$

The constants are conventionally expressed in term of the Luttinger parameters:

$$A = \gamma_1, B = 2\gamma_2, \text{ and } C^2 = 12(\gamma_3^2 - \gamma_2^2). \quad (8.25)$$

The effective masses along [100] are:

$$m_{hh} = \frac{1}{\gamma_1 - 2\gamma_2}, m_{lh} = \frac{1}{\gamma_1 + 2\gamma_2}. \quad (8.26)$$

Luttinger Model

In this section an outlook is given as regards the Luttinger model in case of low confined system. The low confined system has L_x and L_y as in-plane size and L_z the size in the growth direction, with $L_x, L_y \gg L_z$. That is the condition for quantization of states in z-direction. In order to approach realistically this problem the Kohn-Luttinger (KL) model uses a 3 x 2 valence band matrix and introduces the conduction band by a Lowdin renormalization [BAH99]. Since here a low dimensional system is considered, the four-fold degeneracy at $\vec{k} = 0$ is broken. Consequently, the SO-band is pushed down and the light and the heavy hole are energetically separated. Then the states with $j = 3/2$ and $j = 1/2$ are energetically apart from each other. The total angular momentum $j = 3/2$ has two components for j_z , that are $j_z = 3/2$ and $j_z = 1/2$. Let distinguish two cases:

- In the first case, when the state $|j, j_z\rangle = |3/2, 3/2\rangle$ is considered, the wave function is expressed as a linear combination of the states $|X\rangle$ and $|Y\rangle$, which refer to the

valence-band states with the symmetry of p_x and p_y orbitals. It implies that the p-orbitals are oriented in the x- and y-direction. The resulting bands have lighter mass in the xy-plane and heavier in the z-direction, i.e. $m_{xy}^{3/2} < m_z^{3/2}$ (see Fig.8.6 (a)).

- In the second case, when the state $|j, j_z\rangle = |3/2, 1/2\rangle$ is considered, the wave function is expressed as $|Z\rangle$, which refers to the valence-band state with the symmetry of p_z orbitals. In this case the p-orbitals are oriented along z and the masses are consequently heavier in the direction normal to z, that leads to $m_z^{1/2} < m_{xy}^{1/2}$ [DAV98].

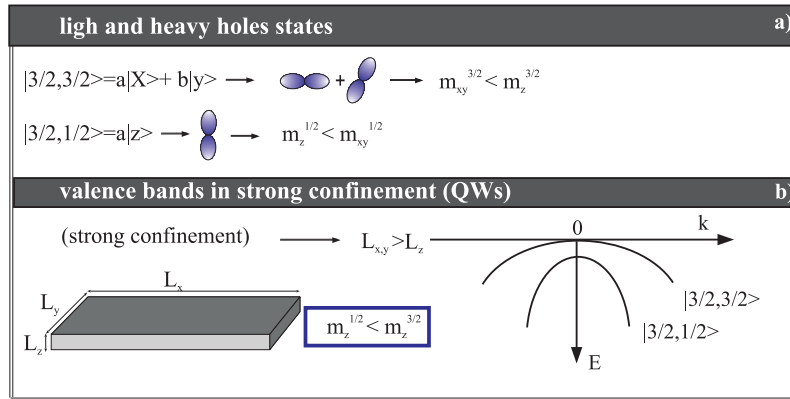


Fig. 8.6: (a) Schematic explanation of the heavy and the light holes. (b) Case of strong confinement for QWs whose in plane size ($L_{x,y}$) is bigger than the vertical size L_z . Also the break of the degeneracy at $\vec{k} = 0$ is shown.

Normally, the KL model is easier to be applied in case of a zinc-blend or diamond crystal structure, where the symmetric properties of the s- and p-orbitals can be considered. Nevertheless, this model was further simplified by Luttinger, who considered a sub-part of the KL valence band matrix. By this model only information about hh and lh states are given. The Luttinger matrix became:

$$\begin{pmatrix} P+Q & S & R & 0 \\ -S^+ & P-Q & 0 & R \\ R^+ & 0 & P-Q & S \\ 0 & R^+ & S^+ & P+Q \end{pmatrix}. \quad (8.27)$$

The matrix's coefficients P, Q, R and S are explicated as: $P = \frac{\hbar^2}{2m_0}\gamma_1(k_x^2 + k_y^2 + k_z^2)$,

$$Q = \frac{\hbar^2}{2m_0}\gamma_2(k_x^2 + k_y^2 - 2k_z^2),$$

$$R = \frac{\hbar^2}{2m_0}[-\sqrt{3}\gamma_2(k_x^2 - k_y^2) + i2\sqrt{3}\gamma_3k_xk_y]$$

$$S = \frac{\hbar^2}{2m_0} 2\gamma_3 (k_x - ik_y) k_z.$$

It must be remarked that, contrarily to the previous models, these results can be extended to high \vec{k} values. In addition, taking into account the axial approximation, γ_2 become proportional to γ_3 ($\gamma_2 \approx \gamma_3$).

These coefficients contain the Luttinger parameters (γ_i), describing the energy dispersion in k-space. Furthermore, the off-diagonal terms take into account the coupling between the lh and hh. By the Luttinger model, the heavy and the light hole masses can be rewritten, where the motion in z and in-plane must be distinguished. If one considers the motion in the z-direction:

- for $j_z = 3/2$, the effective mass in z-direction is:

$$m_{hz} = m_0 / (\gamma_1 - 2\gamma_2), \quad (8.28)$$

- while, for $j_z = 1/2$, the effective mass is:

$$m_{lz} = m_0 / (\gamma_1 + 2\gamma_2). \quad (8.29)$$

The eqs. 8.28 and 8.29 give the hh- and lh-masses in the Luttinger formalism, when the motion in z-direction is considered. It results in $m_{lz} < m_{hz}$. On the contrary, when the motion in-plane of the QW is taken into account, it is found that,

- for $j_z = 3/2$ it is:

$$m_{h\parallel} = m_0 / (\gamma_1 + \gamma_2), \quad (8.30)$$

- whereas, for $j_z = 1/2$ it is:

$$m_{l\parallel} = m_0 / (\gamma_1 - \gamma_2). \quad (8.31)$$

In this last case, $m_{l\parallel} > m_{h\parallel}$ is found. This behavior known as *mass reversal* effect, was experimentally observed by compressive [0 0 1] uniaxial stress [HEN63, PER00, BRA97, IVC96]. Figure 8.6 (b) shows a sketch of the hh and lh state for a QW where no coupling was considered. The energy separation between the states, with distinguished heavy and light holes character is due to the presence of strong confinement. Nonetheless, the case of a mixing between the valence band states should also be taken into consideration. Figure 8.7 (b) shows the band dispersion versus k_z component, for both the cases of strong confinement left and mixing of states (right), respectively. In the second case, a mixing between hh and lh bands is considered, which leads to an anti-crossing between the bands. Since the mixing between hh and lh can be caused by the confinement and size of the studied system, a mass reversal or mixing between the bands can be expected when morphological changes of the quantum-system are considered.

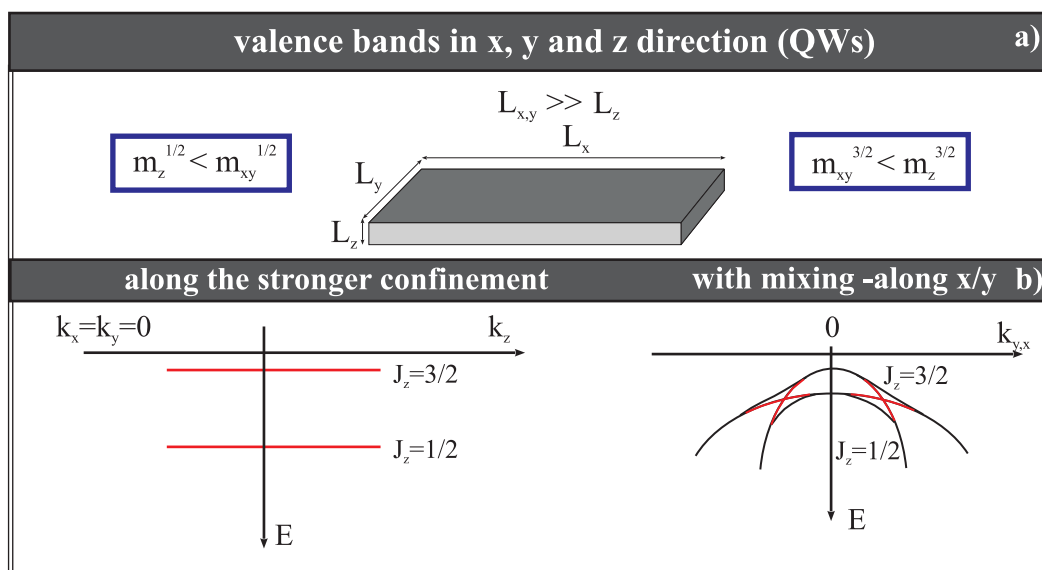


Fig. 8.7: Valence states calculated in case of QWs with (a) size $L_{x,y} \gg L_z$. (b) In the growth axis direction the confinement induces to the splitting between light and heavy holes. Whereas (c) in-plane a mixing of the bands might be presented.

Appendix C

Samples preparation: S1

The sample described here was grown in collaboration within the SFB 410 project in the Laboratory of Experimentelle Physik III in the University of Würzburg.

- Method of growth: Molecular beam epitaxy (MBE)
- Sample grown by: PhD. Suddhasatta Mahapatra
- Supervisor: Prof. Karl Brunner

Tab. 8.1: Structure of the sample (1794M2)

cap-layer	ZnSe	25 nm
QDs-layer	CdSe	2.0ML
barrier	ZnSe	50 nm
buffer	GaAs	200 nm
subtrait	GaAs	600 μm

The samples S1 was grown by molecular beam epitaxy (MBE). The sample structure is shown in Tab. 6.1. A Si-doped GaAs (001) substrate has been overgrown with an undoped GaAs buffer. Then a 50 nm thick ZnSe layer formed the basis of the II-VI structure. The CdSe-based QDs were realized by deposition of 2.0 ML CdSe by conventional MBE at a temperature of 300 °C, without any growth interruption at any stage. At the end, the structure has been capped with 25 nm of a ZnSe layer. By this method the QDs are embedded in a film like structure forming natural quantum dots [ZRE94].

In order to have information of the morphology of the sample prior TA, high resolution transmission electron microscope (HREM)² images have been recorded, as shown in Fig. 8.8. The well-like QDs formed by MBE, contain a wide range of potential size, $V(x,y)$, where several lateral dimensions, in the range between 8 nm and 20 nm are shown. It leads to an inhomogeneous broad PL-spectra with full width half maximum (FWHM) of 30-40 meV (see section 4.1.2).

²The High resolution electron micrograph (HREM) images have been realized within a collaboration with C. Bougerol, CEA-CNRS NPSC, SP2M/DRFMC/CEA-Grenoble, France.

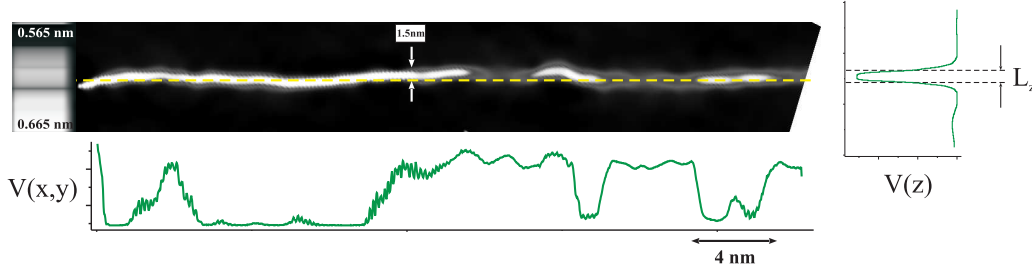


Fig. 8.8: Cross-section HREM images of a 2ML sample (S1). Rough interface of the Cd(Zn)Se layer is shown. The random size and composition distribution leads to a random potential profile along the x-y plane, but the large energy gap difference, between the two material system, leads to a strong and well defined confinement along the z-axis. From a well established relationship existing between lattice constant and material content, the HREM gives also information about the Cd-content within the Cd(Zn)Se layer. Using as reference the ZnSe lattice constant, $a_{ZnSe} = 0.565$ nm, the amount of Cd into the QDs is estimated to be ≈ 70 %.

However, the broad energy gap (1.8 eV) along the growth axis allows to have a box-like potential, $V(z)$, with strong confinement. The cross-sectional HREM images were obtained with a Jeol 4000EX microscope operated at 400 kV. The variation of the lattice parameter along the growth direction (\hat{z} -axis) has been obtained from high resolution off axis images taken after tilting the sample by 10° around the \hat{z} axis from the [110] zone axis. A Wiener filter has been first applied to the images to remove the noise [GAL]. Then, the images have been analyzed by the geometrical phase method, [HYT98, NEU06] which allowed to obtain the lattice parameter along the growth direction using the lower ZnSe barrier as a reference. By knowing the elastic constants of both CdSe ($a_{CdSe} = 0.61$ nm in literature) and ZnSe ($a_{CdSe} = 0.565$ nm in literature), the changes of the lattice constant along the growth axis can be followed. Indeed, using the gray scale of the HREM image, the white region with 0.656 nm indicates that the CdSe layer is still strained, so explaining the absence of the 3D QDs. Consequently, assuming that there was no total relaxation along the foil thickness (thick foil limit). The Cd-composition was estimated to be of 70 % into the QDs.

Finally, Fig. 8.9 shows the atomic force microscopy (AFM) measurement done before the capping of the sample with a ZnSe layer. A top view of a prospective image, Fig. 8.9 (a), and of an in-plane image, Fig. 8.9 (b), clearly show the absence of well defined QDs, but only of a rough interface. Whereas, a well located confinement evidenced in the gray-dark contrast of a TEM cross-image is shown in Fig. 8.9 (c), where the gray-dark contrast is due to the CdSe-ZnSe difference.

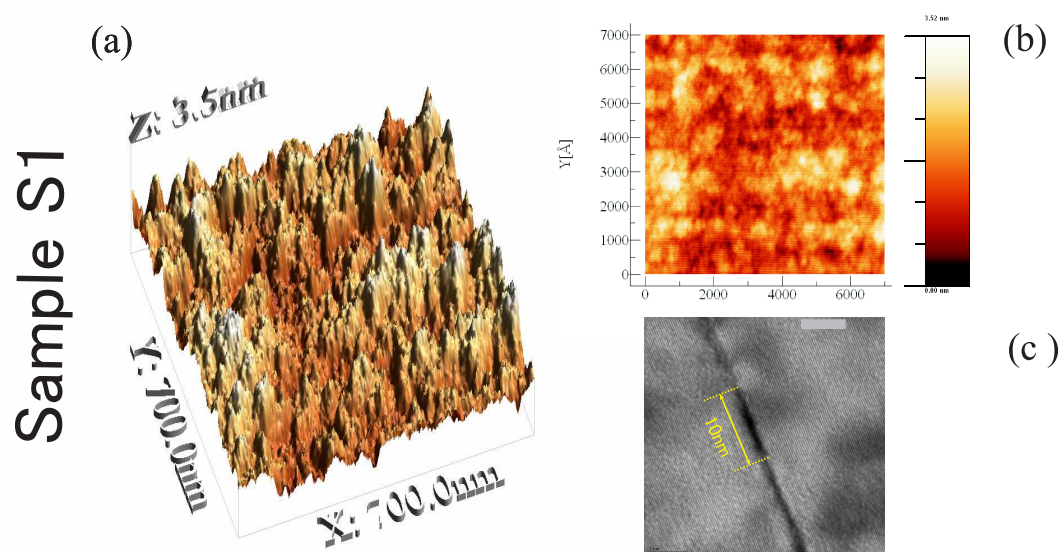


Fig. 8.9: (a) Top view of an AFM image of the sample S1 before the capping with ZnSe layer. The CdSe epilayer shows only a rough interface. (b) The distribution of the roughness can be better seen in a plane-view of the AFM image by the brown-white color distribution. (c) However, QDs-like potentials are formed. Its evidence is given by the cross section of the TEM image (lateral view). Cd-rich areas, defining the QD, are described by dark regions on a gray background.

Appendix D

Samples preparation: S2

The sample described here was grown in collaboration within the CEA-CNRS NPSC, SP2M/ DRFMC/CEA-Grenoble laboratories.

- Method of growth: MBE-ALE
- Sample grown by: Dr. Thomas Aichele
- Supervisor: Prof. Kunthek Keng

Tab. 8.2: Structure of the sample (M1800)

cap-layer	ZnSe	30 nm
QDs-layer	CdSe	3ML
barrier	ZnSe	60 nm
buffer	GaAs	1 μm
substrait	GaAs	600 μm

The sample S2 has a 1 μm thick GaAs buffer layer grown by MBE on top of Zn-doped GaAs (001) substrate. The sample was then transferred under vacuum to a II-VI MBE chamber. A 60 nm ZnSe layer was grown at 280 °C with a growth rate of typically 0.4 ML/s (Zn flux: 2.5×10^{-7} mbar, Se flux: 5×10^{-7} mbar), controlled by reflection high-energy electron diffraction (RHEED). Next, using atomic layer epitaxy (ALE), 3 ML CdSe were deposited, which is just below the critical thickness for strain relaxation.

The sample was then slowly cooled down (within 2 h) to -10 °C and exposed to Se for 30 min, creating a 50-100 nm thick layer of amorphous Se. Next, the sample temperature was slowly increased to 280 °C to desorb the amorphous Se. It is during this process, where the transition to quantum dot islands occurs (Fig.8.10) [ROB06]. Finally, the islands were overgrowth with a 30 nm capping layer. The QDs formed in this way shows a clear evidence of 3D-island formation. The structure of the sample is given in Tab. 6.2. The atomic force microscopy (AFM) image shows an uncapped sample of 3 ML CdSe QDs on ZnSe (see Fig.8.10 (a)), while a plane view of the same

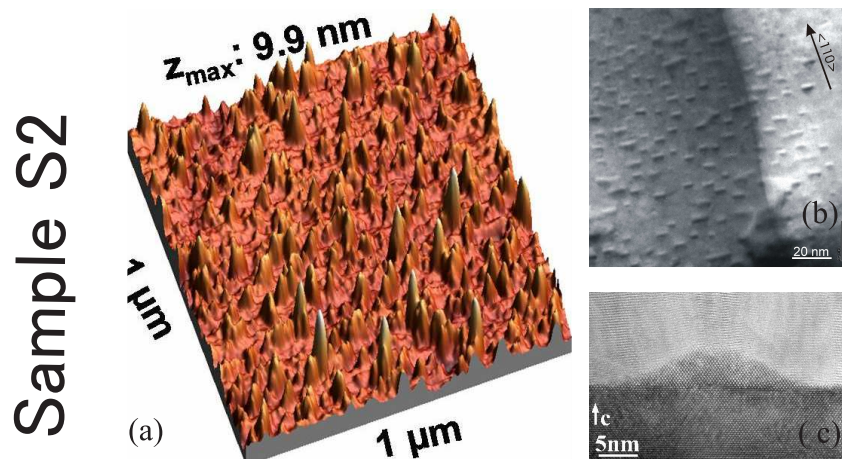


Fig. 8.10: (a) AFM scan of an uncapped sample of 3 ML CdSe QDs on ZnSe. (b) Plan view TEM image of several uncapped 3 ML CdSe QD on ZnSe substrate. The QDs are elongated along one crystal direction $\langle 110 \rangle$ (c) TEM image of an uncapped 3 ML CdSe QD on ZnSe.

sample shows the elongation of the QDs along one crystal direction $\langle 110 \rangle$ (see Fig.8.10 (b)).

Finally, in Fig.8.10 (c) a three-dimensionality of the QD by a TEM image of an uncapped 3ML CdSe QD is shown. The light gray on top of the QD is amorphous selenium.

Appendix E

Samples preparation: S3

The sample described here was grown in collaboration within the SFB 410 project in the Laboratory of Experimentelle Physik III in the University of Würzburg.

- Method of growth: in-situ thermal annealing combined with MBE
- sample grown by: PhD Suddhasatta Mahapatra
- Supervisor: Prof. Karl Brunner

Tab. 8.3: Structure of the sample (9115w10)

cap-layer	ZnSe	25 nm
QDs-layer	CdSe	3.8ML
barrier	ZnSe	50 nm
buffer	GaAs	200 nm
substrait	GaAs	600 μm

The sample S3 was grown by in-situ thermal annealing process combined with MBE, so ensuring the 3D-island formation, otherwise prevented, as discussed in section C. The formation of 3D-QDs was explained by the decrease of the layer-rough, wherein the 3D island are nucleated. The nucleation is caused by an enhanced up-climb of the residue adatom atop the 2D island, while raising the temperature [MAH06].

The sample has a homo-epitaxial undoped GaAs buffer grown atop of a GaAs:Si (001) substrate. The active CdSe QDs formed by in-situ annealing is 3.8 ML thick. However, before to rump up of the temperature, 310 °C, the sample was kept for 10 s under Se-Flus. This time of rest is demonstrated to be the threshold-time afterwards it results in the disappearance of the 3D islands. Finally, the sample was embedded between a 50 nm thick ZnSe buffer layer and 25 nm thick ZnSe cap layer. The structure of the sample is given in Tab. 6.3.

From HREM measurements it was observed that the distance between the QD can be as large as 30 nm. It leads to have lower QDs density compared to the sample S1, where no time of rest under Se flus was used. From Fig. 8.11 (a) the QDs are well

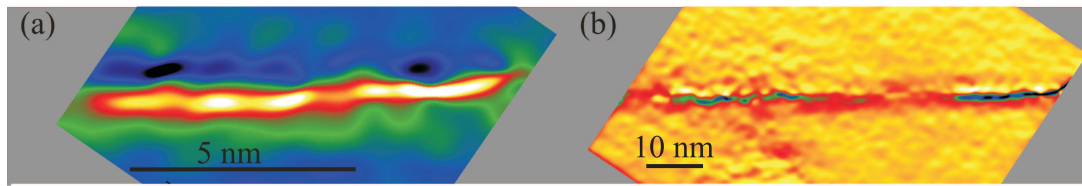


Fig. 8.11: Cross-section HREM images of a 3.8 ML sample (S3) recorded in two different places of the sample. (a) A zoom image shows a QD with later size of 10 nm. (b) The Cd-reach zone is described by the green region.

defined and with a lateral extension of 10 nm. By investigation of a larger area of the sample (again by HREM), it was noted that different later sizes for the QDs can be found. Indeed, in Fig. 8.11 (b), QDs with different later size ranging from 10 nm to 20 nm are measured.

Bibliography

- [ADL96] F. Adler, M. Geiger, A. Bauknecht, F. Scholz, H. Schweizer, M. H. Pilkuhn, B. Ohnesorge, and A. Forchel, *Appl. Phys. Lett.* **80**, 4019 (1996)
- [AIC07] T. Aichele, I.-C. Robin, C. Bougerol, R. André, S. Tatarenko, G. Van Tendeloo, *J. Cryst. Growth* **301**, 281 (2007)
- [AIC07a] T. Aichele, I.-C. Robin, C. Bougerol, R. André, S. Tatarenko, G. Van Tendeloo, *Surface Sci.* **601**, 2664 (2007)
- [AND50] P. W. Anderson, *Phys. Rev.* **79**, 350-356 (1950)
- [AKI07] Y. Akiyama, and H. Sakakia, *J. Cryst. Growth* **301-302**, 697 (2007)
- [ARE86] A. G. Areshkin, G. S. Pekar, G. N. Polisskii, T. B. Popova, L. G. Suslina, D. L. Fedorov, *Sov. Phys. Solid State* **28**, 2109 (1986)
- [AWS00] D. D. Awschalom and R. K. Kawakami, *Nature* **408**, 923 (2000)
- [BAC02] G. Bacher, A. A. Maksimov, H. Schömig, V. D. Kulakovskii, M. K. Welsch, P. S. Dorozhkin, A. V. Chernenko, S. Lee, M. Dobrowolska, J. K. Furdyna and A. Forchel, *Phys. Rev. B* **89**, 127201 (2002)
- [BAC01] G. Bacher, A. A. Maksimov, A. McDonald, H. Schömig, M. K. Welsch, V. D. Kulakovskii, A. Forchel, C. R. Becker, L. W. Molenkamp, and G. Landwehr *phys. stat. sol. (b)* **224**, 573-577 (2001)
- [BAH99] Thomas B. Bahder, *Phys. Rev. B* **45**, 1629 (1992)
- [BAY98] M. Bayer, T. Grutbrod, V. D. Kulakovskii, A. Gorbunov, M. Michel, R. Steffen, K. H. Wang, and A. Forchel, *Phys. Rev. B* **58**, 584740 (1998)
- [BAN99] U. Banin, Y. Cao, D. Katz, and O. Millo, *Nature* **400**, 542 (1999)
- [BLA94] E. Blackwood, M. J. Snelling, S. R. Andrews, C. T. B. Foxon, R. T. Harley, *Phys. Rev. B* **50**, 14246 (1994)
- [BOG01] T. Boggess, L. Zhang, D. G. Deppe, D. L. Huffaker, and C. Cao, *Appl. Phys. Lett.* **78**, 276 (2001)
- [BOL03] F. Bollet, W. P. Gillin, M. Hopkinson, and R. Gwilliam, *J. Appl. Phys.* **93**, 3881 (2003)

- [BRA97] M. Braskén and M. Lindberg, Phys. Rev. B **55**, 9275 (1997)
- [BRA97a] M. Braskén, J. Tulkki, and M. Lindberg, Phys. Rev. B **55**, 559275 (1997)
- [CAR96] *Fundamentals of Semiconductors-Physics and Materials Properties*, Peter Y. Yu and Manuela Cardona Springer-Verlag Berlin Heidelberg New York, (1996)
- [CHA98] Chae-Deok Lee, Chanro Park, Hwack Joo Lee, Kyu-Seok Lee, Seong-Ju Park, and S. K. Noh, Appl. Phys. Lett. **73**, 2615 (1998)
- [CHA96] M. Chamarro, C. Gourdon, O. Lublinskaya, A. I. Ekimov, and P. Lavalard, Phys. Rev. B **53**, 531336 (1996)
- [CHE01] C.-C. Chen, T.-H. Hsueh, Y.-S. Ting, G.-C. Chi, and C.-A. Chang, J. Appl. Phys. **90**, 5180 (2001)
- [CHU95] S. L. Chuang, Physics of Optoelectronic Devices. New York: John Wiley & Sons (1995)
- [CIN99] R. Cingolani, R. Rinaldi, H. Lipsanen, M. Sopanen, R. Virkkala, K. Maijala, J. Tulkki, J. Ahopelto, K. Uchida, N. Miura, and Y. Arakawa, Phys. Rev. Lett. **83**, 4832-4835 (1999)
- [DAV98] *The Physics of Low-Dimensional Semiconductors (An introduction)*, John H. Davies, Cambridge University Press, (1998)
- [DES04] C. F. Destefani, S. E. Ulloa, and G. E. Marques, Phys. Rev. Lett. **69**, 125302 (2004)
- [EFR98] Al. L. Efros and M. Rosen Phys. Rev. B **58**, 587120 (1998)
- [FEL87] J. Feldmann, G. Peter, E. O. Göbel, P. Dawson, K. Moore, C. Foxon, and R. J. Elliott, Phys. Rev. Lett. **59**, 2337 (1987)
- [FON05] V. A. Fonoberov and A.A. Balandin Appl. Phys. Lett. **86**, 226101 (2005)
- [GIL02] B. Gil, A. V. Kavokin Appl. Phys. Lett. **81**, 748 (2002)
- [GIN99] F. Gindele, K. Hild, W. Langbein, U. Woggon, K. Leonardi, D. Hommel, T. Kukulski, G. Bacher, A. Forche, Journal of Luminescence **83-84**, 305-308, (1999)
- [GLI00] *Diffusion in Solids, field-Theory, Solid-State Principle and Applications* by Martin Eden Glicksman, Rensselaer Polytechnic Institute, A Wiley-Interscience Publication (2000)
- [GOD06] M. P. F. de Godoy, P. F. Gomes, M. K. K. Nakaema, F. Iikawa, M. J. S. P. Brasil, R. A. Caetano, J. R. Madureira, J. R. R. Bortoleto, M. A. Cotta, E. Ribeiro, G. E. Marques, and A. C. R. Bittencourt, Phys. Rev. B **73**, 033309 (2006)

- [GRU95] M. Grundmann, J. Christen, N. N. Ledentsov, J. Böhrer, D. Bimberg, S. S. Ruvimov, P. Werner, U. Richter, U. Gösele, J. Heydenreich, V. M. Ustinov, A. Yu. Egorov, A. E. Zhukov, P. S. Kop'ev, Zh. I. Alferov, Phys. Rev. Lett. **74**, 4043 (1995)
- [GUR91] M. Gurioli, A. Vinattieri, M. Colocci, C. Deparis, J. Massies, G. Neu, A. Bosacchi, and S. Franchi, Phys. Rev. B **44**, 3115 (1991)
- [ERD06] M. Erdmann, C. Ropers, M. Wenderoth, S. Malzer, G. H. Döhler, and R. G. Ulbrich, Phys. Rev. B **74**, 125412 (2006)
- [HAR05] *Quantum Wells, Wires and Dots* 2nd Edition, by Paul Harrison, Wiley-Interscience (2005)
- [HEI88] D. Heiman, A. Petrou, S. H. Bloom, Y. Shapira, E. D. Isaacs, and W. Girit Phys. Rev. Lett. **60**, 1876 (1988)
- [HEN63] J. C. Hensel and G. Feher, Phys. Rev. **129**, 1041 (1963)
- [HYT98] M.J. Hÿtch, E. Snoeck, R. Kilaas, Ultramicroscopy **74**, 131 (1998)
- [GAL] Strain determination software, P.L. Galindo, Universidad Cadiz, Spain.
- [HEI88] D. Heiman, A. Petrou, S. H. Bloom, Y. Shapira, E. D. Isaacs, W. Girit, Phys. Rev. Lett. **60**, 1876 (1988)
- [HEI96] R. Heitz, M. Grundmann, N. N. Ledentsov, L. Eckey, M. Veit, D. Bimberg, V. M. Ustinov, A. Y. Egorov, A. E. Zhukov, P. S. Kop'ev, and Zh. I. Alferov, Appl. Phys. Lett. **68**, 361 (1996)
- [HEN07] K. Hennessy, A. Badolato, M. Winger, D. Gerace, M. Atatüre, S. Gulde, S. Fält, E. L. Hu, and A. Imamolu, Nature **445**, 896-899 (2007)
- [HER97] K. Herz, T. Kuemmel, G. Bacher, A. Forchel, B. Jobst, D. Hommel, and G. Landwehr, Phys. Rev. B **56**, 15261 (1997)
- [KES90] H. W. van Kesteren, E. C. Cosman, C. T. Foxon, and W. A. J. A. van der Poel, Phys. Rev. B **41**, 5283 (1990)
- [KiS01] A. A. Kiselev, E. Yablonovitch and K. W. Kim Phys. Rev. B **64**, 25303 (2001)
- [KIM00] C. S. Kim, M. Kim, J. K. Furdyna, M. Dobrowolska, S. Lee, H. Rho, L. M. Smith, Howard E. Jackson, E. M. James, Y. Xin, and N. D. Browning, Phys. Rev. Lett. **85**, 1124 (2000)
- [KOT91] E. S. Koteles, B. Elman, P. Melman, J. Y. Chi, and C. A. Armiento, Optic. Quant. Electr. **23**, S779, (1991)
- [KOT01] R. Kotlyar, T. L. Reinecke, M. Bayer, A. Forchel, Phys. Rev. B **63**, 85310 (2001)

- [KRO04] M. Kroutvar, Y. Ducommun, D. Heiss, M. Bichler, D. Schuh, G. Abstreiter, J. J. Finley, *Nature* **432**, 81 - 84 (2004)
- [KUL99] V. D. Kulakovskii, G. Bacher, R. Weigand, T. Kümmell, E. Borovitskaya, K. Leonardi and D. Hommel, and A. Forchel, *Phys. Rev. Lett.* **82**, 1780 (1999)
- [KUN98] M. Kuno, M. Nirmal, A. Efros, M. Rosen and M. G. Bawendi *J. Chem. Phys.* **108**, 4242 (1998)
- [KUN99] *Phys. Rev. Lett.* **82**, 1780 (1999)
- [YAB88] E. Yablonovic, H. M. Cox, and T. J. Gmitter, *Appl. Phys. Lett.* **52**, 1002 (1988)
- [YOA85] T. Yao, *J. Cryst. Growth* **72**, 31, (1985)
- [YUA02] Z. Yuan, B. E. Kardynal, R. M. Stevenson, A. J. Shields, C. J. Lobo, K. Cooper, N. S. Beattie, D. A. Ritchie, M. Pepper, *Science* **294**, 102 (2002)
- [IVC96] E. L. Ivchenko, U. Rössler, and A. Yu Kaminski, *Phys. Rev. B* **54**, 5852 (1996)
- [IVC97] E. L. Ivchenko, U. Rössler, and A. Yu. Kaminski, *Phys. Rev. B* **54**, 545852 (1997)
- [IVC97a] E. L. Ivchenko and G. Pikus, *Superlattices and Other Heterostructures*, Springer, Berlin, 1997.
- [LAN96] Landolt-Börnstein Comprehensive Index, ed. O. Madelung and W. Martienssen (Springer, Berlin 1996).
- [LEE04] S. Lee et al. *Semicond. Sci. Technol.* **19**, 1125 (2004)
- [LEO97] R. Leon, D. R. M. Williams, J. Krueger, E. R. Weber, and M. R. Melloch *Phys. Rev. B* **56**, R4336 (1997)
- [LIM00] Y. S. Lim, H.S. Kim, D.W. Moon, and J. Y. Lee, *Appl. Phys. Lett.* **77**, 4157 (2000)
- [LIP96] H. Lipsaner, M. Sopanen, M. Taskinen, J. Ahopelto, and J. Tulkki, *Appl. Phys. Lett.* **68**, 2216 (1996)
- [LIT01] D. Litvinov, A. Rosenauer, D. Gerthsen, and E. Kurtz, *J. Appl. Phys.* **89**, 4150 (2001)
- [LIT01] D. Litvinov, A. Rosenauer, D. Gerthsen, H. Preis, K. Fuchs, and S. Bauer, *J. Appl. Phys.* **89**, 3695 (2001)
- [LIS03] K. Lis, S. Bednarek, B. Szafran, and J. Adamowski, *Physica E: Low-dimensional systems and Nanostructures* **17**, 494 (2003)

- [MAC03] S. Mackowski, T. A. Nguyen, H. E. Jackson, J. Kossut, G. Karczewski, L. M. Smith, *Appl. Phys. Lett.* **83**, 5524 (2003)
- [MAC03-1] S. Mackowski, L. M. Smith, H. E. Jackson, W. Heiss, J. Kossut, and G. Karczewski, *Appl. Phys. Lett.* **83**, 254 (2003)
- [MAC05] S. Mackowski, T. Gurung, H. E. Jackson, W. Heiss, J. Kossut, G. Karczewski and L. M. Smith *Appl. Phys. Lett.* **86**, 103101 (2005)
- [MAH06] S. Mahapatra, T. Kiessling, E. Margapoti, G. V. Astakhov, W. Ossau, L. Worschech, A. Forchel, and K. Brunner, *Appl. Phys. Lett.* **89**, 043102 (2006)
- [MAH70] J. P. Mahoney, C. C. Lin, W. H. Brumage, and F. Dorman, *J. Chem. Phys.* **53**, 4286 (1970)
- [MARG1] E. Margapoti, L. Worschech, Fabrizio M. Alves, S. Mahapatra, V. Lopez-Richard, K. Brunner, C. Destefani, C. Bougerol, Menéndez-Proupin, Fanyao Qu, G. E. Marques, A. Forchel (submitted on *Phys. Rev. B*)
- [MARG2] E. Margapoti, L. Worschech, S. Mahapatra, K. Brunner, F. M. Alves, V. Lopez-Richard, G. E. Marques, C. Bougerol, A. Forchel (submitted on *Phys. Rev. Lett.*)
- [MAR06] E. Margapoti, L. Worschech, T. Slobodskyy, L. W. Molenkamp, and A. Forchel, *phys. stat. sol. (c)* **3**, 920 (2006)
- [MAR07] E. Margapoti, L. Worschech, A. Tribu, T. Aichele, R. André, K. Kheng and A. Forchel, *Appl. Phys. Lett.* **90**, 181927 (2007)
- [MAR08] E. Margapoti, L. Worschech, S. Mahapatra, K. Brunner, Fabrizio M. Alves, V. Lopez-Richard, G. E. Marques, C. Bougerol and A. Forchel *Phys. Rev. B* **77**, 73308 (2008)
- [MAR93] J. H. Marsh, *Semicond. Scie. Technol.* **8(6)**, 1136, (1993).
- [MAR94] J.-Y. Marzin, J.-M. Gerard, A. Izrael, D. Barrier, G. Bastard, *Phys. Rev. Lett.* **73**, 716 (1994)
- [MED97] G. Medeiros-Ribeiro, F. G. Pikus, P. M. Petro, and A. L. Efros, *Phys. Rev. B* **55**, 1568 (1997)
- [MER98] J. L. Merz, J. K. Furdyna, *J. Crystal Growth* **184/185** 228 (1998)
- [MES99] A. Messiah, *Quantum Mechanics*. Mineola, New York: Dover (1999). See Ch. 15, section 21.
- [NEU06] W. Neumann, H. Kirmse, I. Häusler, and R. Otto, *Journal of Microscopy* **223**, 200 (2006)

- [NIR95] M. Nirmal, D. J. Norris, M. Kuno, M. G. Bawendi, Al. L. Efros, and M. Rosen, *Phys. Rev. Lett.* **75**, 3728 (1995)
- [OH03] Eunsoon Oh, K. J. Yee, S. M. Soh, J. U. Lee, J. C. Woo, H. S. Jeon, D. S. Kim, S. Lee, J. K. Furdyna, H. C. Ri, H. S. Chany, and S. H. Park *Appl. Phys. Lett.* **83**, 4604 (2003)
- [OSH92] J. Oshinowo, D. Grützmacher, M. Stollenwerk, M. Heuken, K. Heime, and A. Forchel, *Appl. Phys. Lett.* **60**, 2660 (1992)
- [OUA90] D. Ouadjaout and Y. Marfaing, *Phys. Rev. B* **41**, 12096 (1990)
- [PAR92] P. J. Parbrook, B. Henderson, K.P. O'Donnell, P.J. Wight and B. Cockayne *J. Cryst. Growth* **117**, 492 (1992)
- [PER00] N. Peranio, A. Rosenauer, D. Gerthsen, S. V. Sorokin, I. V. Sedova, and S. V. Ivanov, *Phys. Rev. B* **61**, 16015 (2000)
- [PER96] E. Pérez, L. Vinã, K. M. Lau, A. Di Carlo, and P. Lugli, *Semicond. Sci. Technol.* **15**, 189-196, (1996)
- [PER00] E. Pérez, L. Viëna, E. S. Koteles, K. M. Lau, A. D. Carlo and P. Lugli, *Semicond. Sci. Technol.* **15**, 189-196, (2000)
- [PRY98] C. Pryor, *Phys. Rev. B* **57**, 7190 (1998)
- [PUL99] J. Puls, M. Rabe, H.-J. Wünsche, and F. Henneberger, *Phys. Rev. B* **60**, 16303 (1999)
- [PUL97] J. Puls and F. Hennerberger *phys. stat. sol. (a)* **164**, 499 (1997)
- [JAC98] *Quantum Dots* L. Jacak, P. Hawrylak, A. Wójs, Springer (1998)
- [JAI93] *II-VI Semiconductors Compunds*, Edited by Musek Jain, World Scientific Publishing (1993)
- [RAO94] S. S. Rao, W. P. Gillin, and K. P. Homewood, *Phys. Rev. B* **50**, 8071 (1994)
- [REE86] M. A. Reed, R. T. Bate, K. Bradshaw, W. M. Duncan, W. R. Frensley, J. W. Lee, and H. D. Shih, *J. Vacuum Sci. Technol. B* **4**, 358 (1986)
- [RYU95] S.-W. Ryu, In Kim, W.G. Jeong and B.-D. Choe, *Appl. Phys. Lett.* **67**, 1417 (1995)
- [ROB06] I.-C. Robin, R. André, C. Bougerol, T. Aichele, S. Tatarenko, *Appl. Phys. Lett.* **88**, 233103 (2006)
- [ROB04] I. C. Robin, R. André, Le Si Dang, H. Mariette¹, S. Tatarenko, J. M. Gérard, K. Kheng, F. Tinjod, M. Bartels, K. Lischka, and D. Schikora *phys. stat. sol. (b)* **241**, 542 (2004)

- [ROB06] I.-C. Robin, R. André, C. Bougerol, T. Aichele, S. Tatarenko, *Appl. Phys. Lett.* **88**, 233103 (2006)
- [SAN03] Charles S. Santori "Generation of nonclassical light using semiconductor quantum dots" PhD Dissertation, Stanford University, 2003
- [SCH02] C. Schulhauser, D. Haft, R. J. Warburton, K. Karrai, A. O. Govorov, A. V. Kalmeitsev, A. Chaplik, W. Schoenfeld, J. M. Garcia, and P. M. Petroff, *Phys. Rev. B* **66**, 193303 (2002)
- [SEG05] R. Seguin, A. Schliwa, S. Rodt, K. Pötschke, and D. Bimberg *Phys. Rev. Lett.* **95**, 257402 (2005)
- [SEG06] R. Seguin, A. Schliwa, S. Rodt, K. Pötschke, U.W. Pohl and D. Bimberg *Phys. E: Low-Dimensional System and Nanostructures* **32**, 101 (2006)
- [SHA88] K. Shahzad, D.J. Olego and C.G. Van de Walle, *Phys. Rev. B* **38**, 1417 (1988)
- [SIL97] S. W. Silva, Yu A. Pusep, J. C. Galzerani, D. I. Lubyshev, P. P. González-Borrero, and P. Basmanji, *Letter to the editor J. Phys. Condens. Matter* **9**, L13, (1997)
- [STI99] O. Stier, M. Grundmann, and D. Bimberg, *Phys. Rev. B* **59**, 5688 (1999)
- [TAL02] D. V. Talapin, S. K. Poznyak, N. P. Gaponik, A. L. Rogach, and A. Eychmüller, *Physica E: Low-Dimensional System and Nanostructures* **14**, 237 (2002)
- [MAS02] *Semiconductor Quantum Dots Physics, Spectroscopy and Applications* Y. Masumoto, T. Takagahara, Nanoscience and Technology, Springer (2002)
- [TAK00] T. Takagahara, *Phys. Rev. B* **62**, 16840 (2000)
- [TAK93] T. Takagahara, *Phys. Rev. B* **47**, 4569 (1993)
- [TAK05] K. Takemoto, Y. Sakuma, S. Hirose, T. Usuki, N. Yokoyama, T. Miyazawa, M. Takatsu and Y. Arakawa, *Physica E: Low-dimensional Systems and Nanostructure* **26**, 185 (2005)
- [THO03] K. Thornton, J. Ågren, and P.W. Voorhess, *Acta Materialia* **51**, 5675, (2003)
- [TOD99] Y. Toda, O. Moriwaki, M. Nishioka, and Y. Arakawa, *Phys. Rev. Lett.* **82**, 4114 (1999)
- [TON94] D. Tönnies, G. Bacher, A. Forchel, A. Waag, and G. Landwehr *Appl. Phys. Lett.* **64**, 766 (1994)
- [TRA95] N. J. Traynor, R. T. Harley, R. J. Warburton, *Phys. Rev. B* **51**, 7361 (1995)

- [TWA87] A. Twardowski, P. Glod, W. J. M. deJonge, and Demianiuk, *Solid State Communication* **64**, 63, (1987)
- [TWA85] A. Twardowski, M. von Ortenberg, and Demianiuk, *J. Cryst. Growth* **72**, 401, (1985)
- [WAL02] C. G. Van de Walle, *Phys. Stat. Sol. (b)* **229**, 221, (2002)
- [WAL98] S. N. Walck, and T. L. Reinecke, *Phys. Rev. Lett.* **57**, 9088 (1998)
- [WAN99] L.-W. Wang, J. Kim, and A. Zunger, *Phys. Rev. B* **59**, 5678 (1999)
- [WEL01] M. K. Welsch, H. Schoemig, M. Legge, G. Bacher, and A. Forchel, *Appl. Phys. Lett.* **78**, 2937 (2001)
- [ZAI01] M. Zaitsev, M. K. Welsch, H. Schömig, G. Bacher, V. D. Kulakovskii, A. Forchel, B. König, C. R. Becker, W. Ossau, and L. W. Molenkamp, *Semicond. Sci. Technol.* **16**, 631 (2001)
- [ZAR05] S. Z. Karazhanov and L. Yan Voon, *Semiconductors* **39**, 161, (2005)
- [ZHA01] L. Zhang, T. F. Boggess, K. Gundogdu, M. E. Flatté, D. G. Deppe, C. Cao, and O. B. Shchekin, *Appl. Phys. Lett.* **79**, 3320 (2001)
- [ZRE94] A. Zrenner, L. V. Butov, M. Hagn, G. Abstreiter, G. Böhm, and G. Weimann *Phys. Rev. Lett.* **72**, 3382 (1994)
- [XIE01] W. Xie, *J. Phys.: Condens. Matter* **13**, 3149 (2001).

Danksagung

Hereby I would like to thank all the people that helped me and made the success of this work possible:

Prof. Dr. A. Forchel, who gave me the opportunity to exploit several facilities for fabrication and sample characterization and to work in a stimulating team.

PD Dr. L. Worschech, who was always present during the time of the PhD-work with discussions and fruitful suggestions. I thank him very much for helping me to grow up as a scientist.

Prof. Dr. Brunner from Experimentelle Physik III for providing high quality QD samples.

My colleague and friend S. Mahapatra from Experimentelle Physik III, for growing QDs samples. In particular, I would like to thank him for many intellectual discussions, which have been important and have inspired my work.

A big thank goes to our colleagues from the Universidade Federal de São Carlos, Prof. V. L. Richard and Prof. G. E. Marques for their friendly collaboration. I would like to thank them for many transatlantic discussions, which have been extremely important for the understanding and the success of the work.

I would like to thank Prof. K. Kheng and Prof. H. Mariette for inviting me to spend two months in the CEA-CNRS "Nanophysique et Semiconducteurs" group at the University J. Fourier-Grenoble in France.

Also, I would like to thank the II-VI group, H. Schömig, M. Scheibner, T. Schmidt, J. Renner for the friendly atmosphere during the work and for several discussions on science.

I would like to thank the colleagues from III-V group, C. Hoffman, S. Reitzenstein and in particular, R. Krebs from the MBE group for sharing discussions and problems.

I would like also to thank all the technicians working in the MSL for their expertise, thus providing an important support to the work, Dipl. Ing. G. Heller, for his availability to solve many technical problems and all the colleagues from the Physikalisches Institut, in particular the Helium-, Elektronik- and the Mechanik-werkstatt for the continuous service they provided.

Finally, I would like to thank my parents. They have been always supportive and very helpful the whole time long I have been working in Germany. A big thank is also dedicated to my friends Suddhasatta and Alessandra for their important support in so many different aspects of life they gave me during these years of my PhD work.

Curriculum Vitae

Emanuela Margapoti, geboren am 18.06.1974 in Lecce (Italy)

1984–1993	Liceo Artistico
June 1993	Diploma di Maturità Artistica
1994–2002	Student of Physics at the University of Lecce
April–September 2000	Student at the University of Saarbrücken (Erasmus Project)
June 2001–April 2002	Master thesis in the Nanotechnology Laboratory in Lecce. Chair Prof. Dr. R. Cingolani, Thema: <i>Fabrication of photonic crystals by electron beam lithography</i>
2003-2007	PhD student in the Technische Physik department at the University of Würzburg

Würzburg, den 07.08.2009

Emanuela MARGAPOTI

Ehrenwörtliche Erklärung

gemäss §6 Abs. 1 Ziff. 3 und 7
der Promotionsordnung der
Fakultät für Physik und Astronomie
der Universität Würzburg

Hiermit erkläre ich ehrenwörtlich, dass ich die Dissertation selbständig und ohne Hilfe eines Promotionsberaters angefertigt und keine weiteren als die angegebenen Quellen und Hilfsmittel benutzt habe.

Die Dissertation wurde bisher weder vollständig noch teilweise einer anderen Hochschule mit dem Ziel, einen akademischen Grad zu erwerben, vorgelegt.

Am 30. April 2002 wurde mir von der Universität Lecce in Italien der akademische Grad 'Laurea in Fisica' (Diplom-Physiker) verliehen. Weitere akademische Grade habe ich weder erworben noch versucht zu erwerben.

Würzburg, den 07.08.2009

Emanuela MARGAPOTI

